Politecnico di Torino

Master's Degree in Aerospace Engineering

Academic Year 2024–2025

SSB-iFEM for Beams: Displacement Reconstruction with a Reduced Number of Strain Sensors

Supervisor
Prof. Marco Gherlone

Candidate
Dario Netti

Abstract

This thesis investigates the application of the inverse Finite Element Method (iFEM) to Euler–Bernoulli beam elements, focusing on a Single-Sensor-Based (SSB) iFEM formulation that reconstructs the displacement field from discrete surface-strain measurements without requiring paired sensors on opposite faces. For beam applications, this enables accurate recovery with unpaired layouts that may place sensors on one or both faces, while still keeping the overall sensor count low.

The work adapts recent SSB ideas to one-dimensional beam models and implements the formulation in MATLAB. The approach treats each strain reading as an independent measurement associated with its physical location on the cross-section or along the span, allowing flexible layouts driven by accessibility and practical instrumentation constraints. The numerical procedure follows a standard finite-element workflow that assembles and solves a least-squares problem at the structural level, with consistent handling of local/global frames and boundary conditions.

Validation proceeds from simple beam cases to configurations indicative of more complex geometries. Across these numerical studies, the SSB-based reconstruction achieves accuracy comparable to the conventional beam iFEM when provided with comparable information. In other words, the SSB formulation and the classical formulation are equivalent in terms of displacement reconstruction performance within the tested conditions.

Overall, the results support SSB-iFEM for beam-like structures as a practical route to shape sensing with fewer sensors and non-paired layouts, offering an attractive option for structural health monitoring and real-time displacement reconstruction in aerospace and related engineering applications.

Contents

Chapter 1

Introduction

The objective of this thesis is the application of the *inverse Finite Element Method* (iFEM) to beam elements, with a specific focus on studying the feasibility of reconstructing the displacement field using a reduced number of strain sensors.

Beams are fundamental structural elements, widely present in aerospace, civil, and marine applications. They often constitute the primary load-carrying members of wings, fuselage frames, bridges, and ship hulls. Due to their structural relevance, deterioration or damage in beams can lead to significant reductions in global stiffness and strength, with severe implications for safety. At the same time, the cost of monitoring and maintaining beams can be very high. For this reason, beam elements provide an ideal case study for evaluating the effectiveness of iFEM-based shape sensing.

In practice, the number of strain sensors plays a critical role in the applicability of such methods. A large sensor network increases both costs and system complexity, and in many cases sensors are not easy to install in critical locations. For instance, the interior of an aircraft wing is already densely packed with cables and systems, making additional sensor installation extremely challenging. Reducing the number of required sensors therefore provides clear advantages: lower costs, simplified cabling and data acquisition, and easier maintenance.

The methodology adopted in this work starts from the finite element formulation of Euler–Bernoulli beams, and extends the iFEM framework accordingly. Inspired by recent developments of the Single-Sensor-Based iFEM (SSB-iFEM) for plates and shells [1], a new least-squares error functional is introduced for Euler–Bernoulli beams. This functional is built directly on *measured* strains on accessible surfaces, thereby enabling displacement field reconstruction without paired sensors on opposite faces. Unlike classical formulations, the use of unpaired sensors on single faces opens the possibility

of achieving accurate shape sensing with fewer measurements.

After deriving the theoretical model, the formulation is implemented in MATLAB to perform analytical verification. The approach is further validated through comparison with high-fidelity simulations; possible experimental tests on real beams are considered as future work.

1.1 iFEM Method Introduction

The *inverse Finite Element Method* (iFEM) is a variational shape-sensing technique introduced by Tessler and Spangler [2]. It provides a systematic framework for reconstructing displacement fields of structures from distributed strain measurements, without requiring knowledge of applied loads, boundary conditions, or material properties. This unique independence from operating conditions makes iFEM especially attractive for applications in structural health monitoring and real-time shape sensing.

Similar to the traditional finite element method (FEM), iFEM is based on the discretization of a structure into finite elements. Shape functions are employed to interpolate the displacement field from nodal degrees of freedom. The strain–displacement relations remain linear, involving spatial derivatives of the shape functions. However, the fundamental difference with respect to FEM lies in the formulation of the governing equations. In FEM, displacements are solved by enforcing equilibrium between external loads and internal forces; in iFEM, displacements are obtained by minimizing a least-squares functional that measures the discrepancy between computed and measured strains. This error functional is quadratic and convex, leading to a system of linear equations for the unknown nodal displacements.

The original iFEM was implemented for 2D structures using Mindlin kinematics [3], with inverse elements such as iMIN3, iQS4, and iCS8. These elements demonstrated accurate displacement reconstruction capabilities for thin-walled structures. Nevertheless, the accuracy of the 2D iFEM strongly depends on the number and distribution of strain sensors. To achieve satisfactory results, a relatively large number of stations is often required, and determining their optimal placement becomes critical.

Extensions of 2D iFEM have been successfully applied to multilayer composite laminates, sandwich structures, wing panels, wing boxes, and stiffened shells [3, 4]. However, limitations emerge when applying 2D iFEM to components with a dominant longitudinal dimension, such as beams or rods. In such cases, the computational model based on 2D shell elements is heavier than needed, while the reconstructed degrees of freedom fail to efficiently capture the dominant axial/bending behavior.

To address this, 1D beam formulations of iFEM were developed [4–6]. The first 1D implementations were based on Timoshenko beam theory, where the error functional accounts for discrepancies in axial, bending, shear, and torsional strains. This formulation proved effective for beam-shaped components such as stiffeners and stringers. More recently, Euler–Bernoulli beam formulations have been considered, especially for slender beams where shear deformations can be neglected [6].

A comparative analysis of 1D and 2D iFEM reveals complementary advantages. On the one hand, 1D beam iFEM requires fewer sensors and lower computational cost, since a small number of elements suffices to model slender components. On the other hand, a purely 1D discretization may not capture local effects or complex cross-sections. Hybrid approaches combine the strengths of both, modeling skins and webs with 2D elements and stringers/stiffeners with 1D inverse elements [4].

1.2 Single-Sensor-Based iFEM

A recent development is the *Single-Sensor-Based iFEM* (SSB-iFEM), proposed to address limitations related to sensor placement [1]. In classical iFEM, accurate bending reconstruction typically requires paired strain sensors on opposite faces at identical stations. This double-sided instrumentation increases complexity and cost and may be infeasible.

SSB-iFEM introduces a modified least-squares functional formulated directly in terms of *surface* strain measurements from accessible faces. By embedding the geometric relation between mid-line strains and curvature, the method enables displacement reconstruction without paired sensors. Adapting this idea to beams allows the use of unpaired sensors located only on one face, increasing layout flexibility and reducing the total number of sensors without sacrificing accuracy—an important advantage in aerospace applications.

1.3 Sensor Positioning in Beam iFEM

The accuracy of iFEM reconstructions strongly depends on station placement. In classical Euler–Bernoulli iFEM, two-sided measurements (top/bottom) at matched x-stations allow one to separate axial and bending contributions [6]. The *minimum* number of stations per element to achieve accurate curvature reconstruction depends on the interpolation order and the chosen station strategy; in this thesis, layouts are selected to match the polynomial

order and ensure stable curvature recovery (see also [6]).

Installing paired sensors on both faces is often impractical. The SSB functional permits reconstruction using single-sensor stations distributed along accessible faces at different x-positions, simplifying instrumentation and improving robustness to sensor loss.

1.4 Application to Structural Health Monitoring

Structural Health Monitoring (SHM) aims to provide continuous or on-demand information about structural state, reducing maintenance costs, increasing safety, and extending service life. Shape sensing through iFEM allows reconstruction of displacement/strain fields from limited sensor sets, enabling real-time insight into load paths and damage. The SSB-based approach enhances practicality by minimizing sensor count and removing the need for paired stations on inaccessible faces, a valuable feature in aerospace structures.

Chapter 2

Theoretical Background

This chapter presents the theoretical foundations for Euler–Bernoulli (EB) beam iFEM and sets the stage for the SSB specialization.

Remark on geometry vs. deformations. We adopt a right-handed frame with x along the beam axis and z upward. The beam *geometry* lies in the x–z plane (nodes with $y = 0$, element local frames rotated within that plane if needed). However, *deformations* may include bending about y (via w and κ_{zz}) *and* about z (via v and κ_{yy}). Therefore, both κ_{zz} and κ_{yy} are retained in the kinematics and in the SSB formulation.

2.1 Kinematics and Degrees of Freedom

Each node has five degrees of freedom (DOFs):

$$\{\, u,\, v,\, w,\, \phi_y,\, \omega_z \,\}. \tag{2.1}$$

The rotational variables are defined as

$$\phi_y = -\, w_{,x}, \tag{2.2}$$
$$\omega_z = v_{,x}. \tag{2.3}$$

Therefore, for a two-node element:

$$\mathbf{u}_e = \{\, u_1,\, v_1,\, w_1,\, \phi_{y1},\, \omega_{z1},\; u_2,\, v_2,\, w_2,\, \phi_{y2},\, \omega_{z2} \,\}^T. \tag{2.4}$$

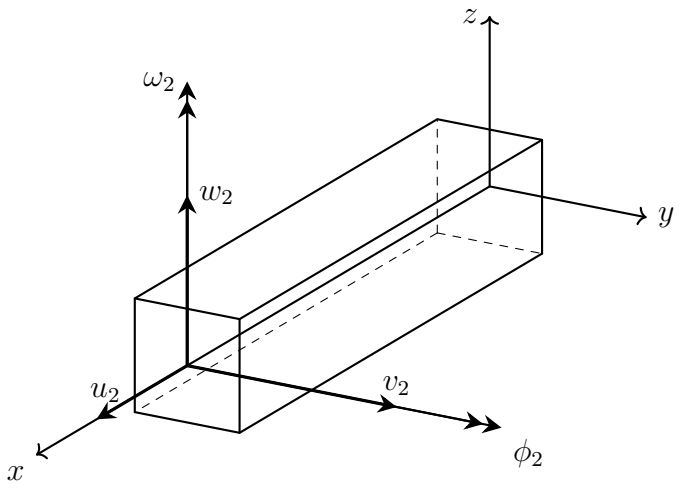

Figure 2.1: Orientation of the beam element and local reference frame. Translational DOFs (u, v, w) act along the local axes (x, y, z), while the rotations ϕ_y and ω_z are associated with bending about the corresponding axes.

The three-dimensional displacement field at (x, y, z) reads

$$u_x = u(x) - z\, w_{,x}(x) - y\, v_{,x}(x), \tag{2.5}$$
$$u_y = v(x), \tag{2.6}$$
$$u_z = w(x), \tag{2.7}$$

yielding

$$\varepsilon_{xx}(x, y, z) = u_{,x} - z\, w_{,xx} - y\, v_{,xx} = \varepsilon + z\, \kappa_{zz} + y\, \kappa_{yy}, \tag{2.8}$$

with

$$\varepsilon = u_{,x}, \tag{2.9}$$
$$\kappa_{zz} = -\, w_{,xx}, \tag{2.10}$$
$$\kappa_{yy} = -\, v_{,xx}. \tag{2.11}$$

2.2 Shape Functions

The finite element formulation requires interpolating the displacement field within each element in terms of its nodal degrees of freedom. A linear Lagrange interpolation is adopted for the axial displacement $u(x)$, while Hermite cubic polynomials are used for the transverse displacements $v(x)$ and $w(x)$ to ensure C^1 continuity of rotations.

Let $\xi = x/L \in [0, 1]$.

Lagrange linear shape functions for u:

$$N_1 = 1 - \xi, \tag{2.12}$$
$$N_2 = \xi. \tag{2.13}$$

Hermite cubic shape functions for v and w:

$$H_1 = 2\xi^3 - 3\xi^2 + 1, \tag{2.14}$$
$$H_2 = \xi^3 - 2\xi^2 + \xi, \tag{2.15}$$
$$H_3 = -2\xi^3 + 3\xi^2, \tag{2.16}$$
$$H_4 = \xi^3 - \xi^2. \tag{2.17}$$

The corresponding second derivatives, required for curvature computation, are

$$H_{1,xx} = \tfrac{1}{L^2}(12\xi - 6), \tag{2.18}$$
$$H_{2,xx} = \tfrac{1}{L^2}(6\xi - 4), \tag{2.19}$$
$$H_{3,xx} = \tfrac{1}{L^2}(-12\xi + 6), \tag{2.20}$$
$$H_{4,xx} = \tfrac{1}{L^2}(6\xi - 2). \tag{2.21}$$

Displacement interpolations:

$$u(x) = N_1 u_1 + N_2 u_2, \tag{2.22}$$
$$v(x) = H_1 v_1 + LH_2\,\omega_{z1} + H_3 v_2 + LH_4\,\omega_{z2}, \tag{2.23}$$
$$w(x) = H_1 w_1 - LH_2\,\phi_{y1} + H_3 w_2 - LH_4\,\phi_{y2}. \tag{2.24}$$

Here, the signs of the rotational terms are consistent with the kinematic definitions $\phi_y = -\,w_{,x}$ and $\omega_z = v_{,x}$.

Matrix representation. The interpolations above can be compactly written as

$$\mathbf{u}(x) = \mathbf{N}_u\,\mathbf{u}_e, \qquad \mathbf{v}(x) = \mathbf{N}_v\,\mathbf{u}_e, \qquad \mathbf{w}(x) = \mathbf{N}_w\,\mathbf{u}_e, \tag{2.25}$$

where the row shape function matrices are

$$\mathbf{N}_u = \Big[N_1\ 0\ 0\ 0\ 0\ \ N_2\ 0\ 0\ 0\ 0\Big], \tag{2.26}$$

$$\mathbf{N}_v = \Big[0\ H_1\ 0\ 0\ LH_2\ \ 0\ H_3\ 0\ 0\ LH_4\Big], \tag{2.27}$$

$$\mathbf{N}_w = \Big[0\ 0\ H_1\ \ -LH_2\ 0\ \ 0\ 0\ H_3\ \ -LH_4\ 0\Big]. \tag{2.28}$$

2.3 Strain–Displacement Relations

The strain measures of an Euler–Bernoulli beam are obtained from the spatial derivatives of the interpolated displacement field. From the kinematic relations (2.9, 2.10, 2.11), each strain component can be expressed in matrix form as a linear combination of the nodal degrees of freedom:

$$\varepsilon = \mathbf{B}_u \, \mathbf{u}_e, \tag{2.29}$$

$$\kappa_{zz} = \mathbf{B}_w \, \mathbf{u}_e, \tag{2.30}$$

$$\kappa_{yy} = \mathbf{B}_v \, \mathbf{u}_e. \tag{2.31}$$

The matrices $\mathbf{B}_u$, $\mathbf{B}_w$, and $\mathbf{B}_v$ are the *strain–displacement matrices* (or *kinematic matrices*) of the element. They contain the derivatives of the shape functions with respect to the axial coordinate and relate the nodal DOFs to the corresponding axial strain and bending curvatures along z and y, respectively.

Using the interpolations defined in Section 2.2, the explicit form of these matrices reads:

$$\mathbf{B}_u = \Big[-\tfrac{1}{L} \; 0 \; 0 \; 0 \; 0 \;\; \tfrac{1}{L} \; 0 \; 0 \; 0 \; 0 \Big], \tag{2.32}$$

$$\mathbf{B}_w = \Big[0 \; 0 \;\; -H_{1,xx} \;\; LH_{2,xx} \;\; 0 \;\; 0 \; 0 \;\; -H_{3,xx} \;\; LH_{4,xx} \;\; 0 \Big], \tag{2.33}$$

$$\mathbf{B}_v = \Big[0 \;\; -H_{1,xx} \; 0 \; 0 \;\; -LH_{2,xx} \;\; 0 \;\; -H_{3,xx} \; 0 \; 0 \;\; -LH_{4,xx} \Big]. \tag{2.34}$$

Here:

- $\mathbf{B}_u$ relates the axial displacement $u(x)$ to the normal strain ε;
- $\mathbf{B}_w$ corresponds to bending about the y-axis (deflection w in the z direction, curvature κ_{zz});
- $\mathbf{B}_v$ corresponds to bending about the z-axis (deflection v in the y direction, curvature κ_{yy}).

These matrices will be used in the subsequent section to construct the iFEM least-squares functional at the element level.

2.4 iFEM Least-Squares Functional (Classical)

Following [2, 6], the iFEM element functional is defined as a weighted least-squares of the station-wise discrepancies between computed and measured

strain measures. For a given element e of length L, let $\{x_i^{\varepsilon}\}_{i=1}^{n_\varepsilon}$, $\{x_j^{kzz}\}_{j=1}^{n_{kzz}}$, and $\{x_\ell^{kyy}\}_{\ell=1}^{n_{kyy}}$ be the stations where the axial strain ε, the curvature κ_{zz} (bending about y), and the curvature κ_{yy} (bending about z) are available, respectively. Denote by e_i^{ε}, $e_j^{\kappa_{zz}}$, $e_\ell^{\kappa_{yy}}$ the corresponding measurements, and by

$$\mathbf{B}_u(x), \qquad \mathbf{B}_w(x), \qquad \mathbf{B}_v(x)$$

the strain–displacement matrices introduced in Section 2.3. The element functional reads

$$\Phi_{\varepsilon}^{e} = \frac{L}{n_\varepsilon} \sum_{i=1}^{n_\varepsilon} \Big(\mathbf{B}_u(x_i^{\varepsilon})\, \mathbf{u}_e - e_i^{\varepsilon} \Big)^2, \tag{2.35}$$

$$\Phi_{\kappa zz}^{e} = \frac{I_{yy}}{A} \frac{L}{n_{kzz}} \sum_{j=1}^{n_{kzz}} \Big(\mathbf{B}_w(x_j^{kzz})\, \mathbf{u}_e - e_j^{\kappa_{zz}} \Big)^2, \tag{2.36}$$

$$\Phi_{\kappa yy}^{e} = \frac{I_{zz}}{A} \frac{L}{n_{kyy}} \sum_{\ell=1}^{n_{kyy}} \Big(\mathbf{B}_v(x_\ell^{kyy})\, \mathbf{u}_e - e_\ell^{\kappa_{yy}} \Big)^2. \tag{2.37}$$

The scaling factors $L/n_\bullet$ distribute stations uniformly along the element, while I_{yy}/A and I_{zz}/A balance the relative magnitude of curvature residuals (units-consistent weighting).

Step-by-step expansion. Introduce the shorthand row operators

$$\mathbf{b}_{u,i} := \mathbf{B}_u(x_i^{\varepsilon}), \quad \mathbf{b}_{w,j} := \mathbf{B}_w(x_j^{kzz}), \quad \mathbf{b}_{v,\ell} := \mathbf{B}_v(x_\ell^{kyy}),$$

so that each scalar residual is

$$r_i^{\varepsilon} = \mathbf{b}_{u,i}\, \mathbf{u}_e - e_i^{\varepsilon}, \tag{2.38}$$

$$r_j^{kzz} = \mathbf{b}_{w,j}\, \mathbf{u}_e - e_j^{\kappa_{zz}}, \tag{2.39}$$

$$r_\ell^{kyy} = \mathbf{b}_{v,\ell}\, \mathbf{u}_e - e_\ell^{\kappa_{yy}}. \tag{2.40}$$

For a generic term of the form $\Big(\mathbf{a}\, \mathbf{u}_e - \alpha\Big)^2$ (with $\mathbf{a} \in \mathbb{R}^{1\times 10}$ and $\alpha \in \mathbb{R}$), the quadratic expansion gives

$$\Big(\mathbf{a}\, \mathbf{u}_e - \alpha\Big)^2 = \mathbf{u}_e^T\, \mathbf{a}^T \mathbf{a}\, \mathbf{u}_e \;-\; 2\,\alpha\, \mathbf{a}\, \mathbf{u}_e \;+\; \alpha^2. \tag{2.41}$$

Applying (2.41) to (2.38) and summing over $i = 1, \ldots, n_\varepsilon$,

$$\begin{aligned}\Phi^e_\varepsilon &= \frac{L}{n_\varepsilon}\sum_{i=1}^{n_\varepsilon}\left(\mathbf{u}_e^T\,\mathbf{b}_{u,i}^T\mathbf{b}_{u,i}\,\mathbf{u}_e - 2\,e_i^\varepsilon\,\mathbf{b}_{u,i}\,\mathbf{u}_e + (e_i^\varepsilon)^2\right)\\ &= \mathbf{u}_e^T\underbrace{\left(\frac{L}{n_\varepsilon}\sum_{i=1}^{n_\varepsilon}\mathbf{b}_{u,i}^T\mathbf{b}_{u,i}\right)}_{\mathbf{A}_e}\mathbf{u}_e \;-\; 2\,\mathbf{u}_e^T\underbrace{\left(\frac{L}{n_\varepsilon}\sum_{i=1}^{n_\varepsilon}\mathbf{b}_{u,i}^T e_i^\varepsilon\right)}_{\mathbf{b}_e}\\ &\quad+\underbrace{\left(\frac{L}{n_\varepsilon}\sum_{i=1}^{n_\varepsilon}(e_i^\varepsilon)^2\right)}_{c_\varepsilon}.\end{aligned} \tag{2.42}$$

Analogously, for the curvature contributions:

$$\begin{aligned}\Phi^e_{\kappa zz} &= \mathbf{u}_e^T\underbrace{\left(\frac{I_{yy}}{A}\,\frac{L}{n_{kzz}}\sum_{j=1}^{n_{kzz}}\mathbf{b}_{w,j}^T\mathbf{b}_{w,j}\right)}_{\mathbf{A}_{kzz}}\mathbf{u}_e - 2\,\mathbf{u}_e^T\underbrace{\left(\frac{I_{yy}}{A}\,\frac{L}{n_{kzz}}\sum_{j=1}^{n_{kzz}}\mathbf{b}_{w,j}^T e_j^{\kappa_{zz}}\right)}_{\mathbf{b}_{kzz}}\\ &\quad+\underbrace{\left(\frac{I_{yy}}{A}\,\frac{L}{n_{kzz}}\sum_{j=1}^{n_{kzz}}(e_j^{\kappa_{zz}})^2\right)}_{c_{kzz}},\end{aligned} \tag{2.43}$$

$$\begin{aligned}\Phi^e_{\kappa yy} &= \mathbf{u}_e^T\underbrace{\left(\frac{I_{zz}}{A}\,\frac{L}{n_{kyy}}\sum_{\ell=1}^{n_{kyy}}\mathbf{b}_{v,\ell}^T\mathbf{b}_{v,\ell}\right)}_{\mathbf{A}_{kyy}}\mathbf{u}_e - 2\,\mathbf{u}_e^T\underbrace{\left(\frac{I_{zz}}{A}\,\frac{L}{n_{kyy}}\sum_{\ell=1}^{n_{kyy}}\mathbf{b}_{v,\ell}^T e_\ell^{\kappa_{yy}}\right)}_{\mathbf{b}_{kyy}}\\ &\quad+\underbrace{\left(\frac{I_{zz}}{A}\,\frac{L}{n_{kyy}}\sum_{\ell=1}^{n_{kyy}}(e_\ell^{\kappa_{yy}})^2\right)}_{c_{kyy}}.\end{aligned} \tag{2.44}$$

Quadratic form and normal equations. By summing Eqs. (2.42)–(2.44), the complete element functional is obtained as

$$\Phi_e = \Phi^e_\varepsilon + \Phi^e_{\kappa zz} + \Phi^e_{\kappa yy} = \mathbf{u}_e^T\,\mathbf{K}_e\,\mathbf{u}_e - 2\,\mathbf{u}_e^T\,\mathbf{f}_e + c, \tag{2.45}$$

with

$$\mathbf{K}_e = \mathbf{A}_e + \mathbf{A}_{kzz} + \mathbf{A}_{kyy}, \tag{2.46}$$

$$\mathbf{f}_e = \mathbf{b}_e + \mathbf{b}_{kzz} + \mathbf{b}_{kyy}, \tag{2.47}$$

$$c = c_\varepsilon + c_{kzz} + c_{kyy}. \tag{2.48}$$

Stationarity of (2.45) with respect to $\mathbf{u}_e$ yields the element normal equations

$$\frac{\partial \Phi_e}{\partial \mathbf{u}_e} = 2\,\mathbf{K}_e\,\mathbf{u}_e - 2\,\mathbf{f}_e = \mathbf{0} \qquad \Longrightarrow \qquad \boxed{\mathbf{K}_e\,\mathbf{u}_e = \mathbf{f}_e}. \tag{2.49}$$

After standard finite-element assembly over all elements,

$$\boxed{\mathbf{K}\,\mathbf{u} = \mathbf{f}}. \tag{2.50}$$

Remarks. (i) Each matrix $\mathbf{A}_\bullet$ is symmetric positive semidefinite; positive definiteness (and thus uniqueness of $\mathbf{u}_e$) requires sufficiently informative station placement. (ii) The constants collected in c depend only on measurements and do not affect the minimizer. (iii) The factors I_{yy}/A and I_{zz}/A render curvature residuals commensurate with axial strain residuals, avoiding an artificial bias due to units or magnitudes.

Chapter 3

Single-Sensor-Based iFEM (general sensor-based formulation for beams)

This chapter introduces the Single-Sensor-Based inverse Finite Element Method (SSB-iFEM) and develops its specialization to Euler–Bernoulli beams with *arbitrary* cross-sections. Unlike face-based formulations (e.g., top/bottom, left/right of a rectangular section), here each strain measurement is associated with its own coordinates (x_i, y_i, z_i), and the element least-squares functional is defined as the sum of the residuals over all sensors located within the element. This generalization preserves the rationale of SSB-iFEM for plates and shells [2,3] while extending its applicability to beams with generic cross-sections and sensor layouts.

3.1 From plate SSB-iFEM to beam kinematics

The Single-Sensor-Based inverse Finite Element Method (SSB-iFEM) for plates and shells [1, 2] expresses surface strains as linear combinations of mid-surface membrane strains and bending curvatures evaluated at the same in-plane location. For beams, the same rationale can be adopted by restricting the *geometry* to the x–z plane (the y-axis completing a right-handed triad), while allowing an *arbitrary cross-section* and arbitrary sensor placement.

Under Euler–Bernoulli kinematics (see Chapter 2), the axial strain at a generic point (x, y, z) of the beam cross-section varies linearly with respect

to the transverse coordinates as

$$\varepsilon_{xx}(x, y, z) = \varepsilon(x) + z\,\kappa_{zz}(x) + y\,\kappa_{yy}(x), \tag{3.1}$$

as introduced in Eq. (2.8). This relation reflects the fundamental assumption that plane sections remain plane and orthogonal to the neutral axis during deformation, leading to a linear distribution of axial strain over the section. The mid-line strain ε accounts for axial stretching, whereas κ_{zz} and κ_{yy} represent the curvatures associated with bending about the y- and z-axes, respectively.

The corresponding one-dimensional strain measures are defined in Eqs. (2.9)–(2.11) as

$$\varepsilon(x) = u_{,x}(x), \qquad \kappa_{zz}(x) = -\,w_{,xx}(x), \qquad \kappa_{yy}(x) = -\,v_{,xx}(x).$$

In the finite element setting (Eqs. (2.29)–(2.31)), these quantities are interpolated through the strain–displacement matrices $\mathbf{B}_u(x)$, $\mathbf{B}_w(x)$, and $\mathbf{B}_v(x)$:

$$\varepsilon(x) = \mathbf{B}_u(x)\,\mathbf{u}_e, \qquad \kappa_{zz}(x) = \mathbf{B}_w(x)\,\mathbf{u}_e, \qquad \kappa_{yy}(x) = \mathbf{B}_v(x)\,\mathbf{u}_e,$$

with $\mathbf{u}_e$ the element displacement vector defined in Eq. (2.4).

In the classical iFEM formulation (Chapter 2), these strain components are reconstructed from paired measurements taken on opposite faces of the beam, thus enabling separation of the axial and bending contributions. The SSB-iFEM generalizes this framework by treating each strain measurement as an independent observation associated with its own coordinates (x_i, y_i, z_i), without requiring symmetry or paired sensors. This viewpoint leads naturally to a sensor-wise least-squares formulation, introduced in the following section.

3.2 Sensor stations and measurement model

Consider element e of length L, instrumented with N_e strain sensors. The i-th sensor is located at the axial coordinate $x_i \in [0, L]$ (parent coordinate $\xi_i = x_i/L \in [0, 1]$) and at the transverse offsets (y_i, z_i) measured from the centroidal (neutral) axes of the cross-section. Each strain measurement is therefore associated with a well-defined point (x_i, y_i, z_i) in the local reference frame of the element.

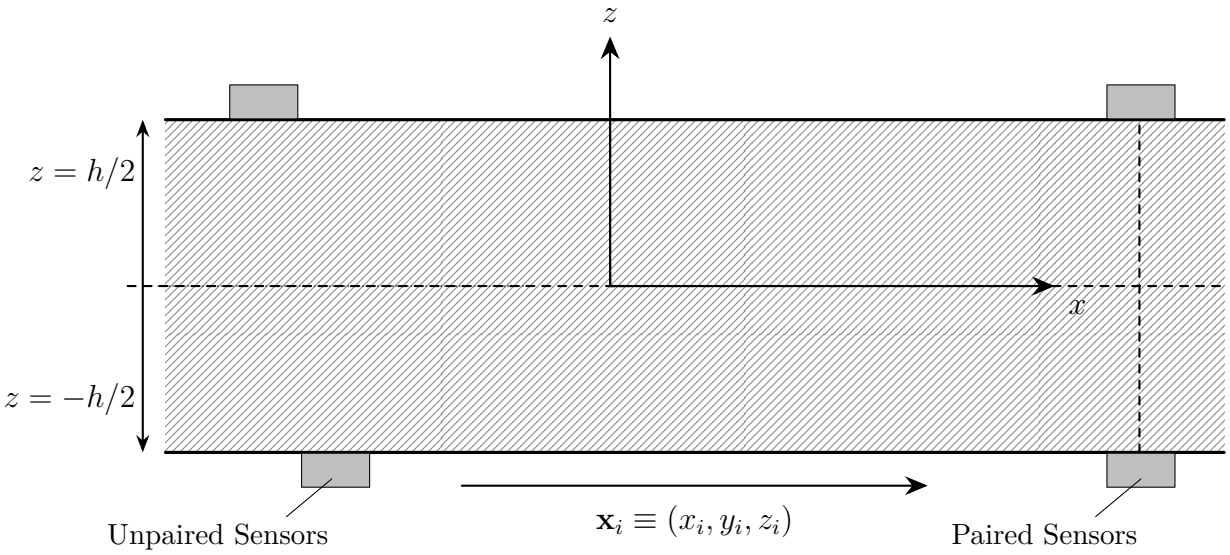

Figure 3.1: Example of strain-sensor arrangements along a beam element. On the left, a *decoupled* (single-surface) configuration as used in the SSB-iFEM; on the right, a *paired* configuration typical of classical iFEM with top/bottom sensors at matching stations. The local reference axes and section height ($z = \pm h/2$) are also shown.

From Eq. (3.1) and the finite element strain–displacement relations of Eqs. (2.29)–(2.31), the *predicted* axial strain at the sensor location is obtained by substituting the kinematic expressions of ε, κ_{zz}, and κ_{yy} into the linear relation for $\varepsilon_{xx}(x, y, z)$. The resulting expression reads

$$\varepsilon_s(x_i, y_i, z_i) = \Big(\mathbf{B}_u(x_i) + z_i\, \mathbf{B}_w(x_i) + y_i\, \mathbf{B}_v(x_i) \Big)\, \mathbf{u}_e = \mathbf{A}_i\, \mathbf{u}_e, \tag{3.2}$$

where the *row operator* $\mathbf{A}_i \in \mathbb{R}^{1\times 10}$ collects the contributions of the axial and bending strain components:

$$\mathbf{A}_i = \mathbf{B}_u(x_i) + z_i\, \mathbf{B}_w(x_i) + y_i\, \mathbf{B}_v(x_i). \tag{3.3}$$

In this expression, the first term represents the mid-line (axial) strain sensitivity, while the second and third terms weight the curvatures about the y- and z-axes by the corresponding offsets of the sensor.

Let e_i^{ε} denote the *measured* strain provided by sensor i. The difference between the predicted and the measured values defines the *scalar residual*

$$r_i = \mathbf{A}_i\, \mathbf{u}_e - e_i^{\varepsilon}, \tag{3.4}$$

which quantifies the local discrepancy between model and measurement. These residuals form the fundamental building blocks of the SSB-iFEM least-squares functional introduced in the next section.

3.3 SSB-iFEM element functional

The inverse finite element method (iFEM) determines the unknown nodal degrees of freedom by minimizing a least-squares functional that measures the discrepancy between predicted and measured strains. In the Single-Sensor-Based formulation, each sensor contributes individually to this functional through its scalar residual r_i defined in Eq. (3.4). Accordingly, the element-level functional for beam element e is expressed as

$$\Psi_e(\mathbf{u}_e) = \frac{L}{N_e} \sum_{i=1}^{N_e} \lambda_i \left(\mathbf{A}_i \, \mathbf{u}_e - e_i^{\varepsilon} \right)^2, \tag{3.5}$$

where L/N_e acts as a uniform scaling factor along the element length, and $\lambda_i > 0$ is a non-dimensional weight associated with sensor i.

The term inside the parentheses represents the local residual at sensor i, i.e., the error between the predicted strain $\mathbf{A}_i\mathbf{u}_e$ and the corresponding measurement e_i^{ε}. The minimization of $\Psi_e(\mathbf{u}_e)$ therefore yields the set of nodal displacements that best reproduces the measured strain field in a least-squares sense.

Definition and role of the weights. The coefficients λ_i in Eq. (3.5) determine the relative influence of each sensor in the minimization. Each λ_i is assigned individually to the i-th sensor and has the following physical meaning:

- $\lambda_i = 1$ if the i-th sensor is active and considered fully reliable;
- $\lambda_i = 0$ if the i-th sensor is absent, faulty, or intentionally excluded from the functional;
- $0 < \lambda_i < 1$ if the i-th sensor is available but affected by uncertainty or reduced confidence, e.g. due to calibration errors or increased noise.

The introduction of these weights provides a simple yet powerful way to control the contribution of each strain measurement, enabling the formulation to handle heterogeneous datasets or partially missing measurements. In practical implementations, the weights can also be interpreted as inverse variance factors, $\lambda_i \propto 1/\sigma_i^2$, when the sensor noise level σ_i is known. Unless otherwise specified, all active sensors are assumed to have unit weights ($\lambda_i = 1$).

The functional in Eq. (3.5) generalizes the classical iFEM least-squares expression (see Eq. (2.45)) by assembling all strain components into a single

sensor-wise summation. In contrast to the traditional formulation, which separates the contributions of axial strain and bending curvatures, the SSB-iFEM treats each strain measurement individually through its local coordinates (x_i, y_i, z_i). This unified representation enables the method to handle arbitrary sensor layouts and cross-section geometries without requiring predefined sensor pairs.

3.4 Element matrices

Starting from the sensor-wise residual in Eq. (3.4),

$$r_i \;=\; \mathbf{A}_i\,\mathbf{u}_e \;-\; e_i^{\varepsilon}, \tag{3.6}$$

the SSB-iFEM element functional in Eq. (3.5) reads

$$\Psi_e(\mathbf{u}_e) \;=\; \frac{L}{N_e}\sum_{i=1}^{N_e}\lambda_i\, r_i^2. \tag{3.7}$$

Quadratic expansion at a single sensor. For a generic scalar of the form $(\mathbf{a}\,\mathbf{u}_e - \alpha)^2$, one has the identity

$$(\mathbf{a}\,\mathbf{u}_e - \alpha)^2 \;=\; \mathbf{u}_e^T\,\mathbf{a}^T\mathbf{a}\,\mathbf{u}_e \;-\; 2\,\alpha\,\mathbf{a}\,\mathbf{u}_e \;+\; \alpha^2. \tag{3.8}$$

By setting $\mathbf{a} = \mathbf{A}_i$ and $\alpha = e_i^{\varepsilon}$, Eq. (3.8) gives

$$r_i^2 \;=\; \mathbf{u}_e^T\,\mathbf{A}_i^T\mathbf{A}_i\,\mathbf{u}_e \;-\; 2\,e_i^{\varepsilon}\,\mathbf{A}_i\,\mathbf{u}_e \;+\; \left(e_i^{\varepsilon}\right)^2. \tag{3.9}$$

Summation over all sensors. Substituting (3.9) into (3.7) and collecting like terms yields

$$\begin{aligned}\Psi_e(\mathbf{u}_e) = \mathbf{u}_e^T\Big(\frac{L}{N_e}\sum_{i=1}^{N_e}\lambda_i\,\mathbf{A}_i^T\mathbf{A}_i\Big)\mathbf{u}_e \;-\; 2\,\mathbf{u}_e^T\Big(\frac{L}{N_e}\sum_{i=1}^{N_e}\lambda_i\,\mathbf{A}_i^T e_i^{\varepsilon}\Big)\\ +\;\frac{L}{N_e}\sum_{i=1}^{N_e}\lambda_i\left(e_i^{\varepsilon}\right)^2.\end{aligned} \tag{3.10}$$

Element matrices. Define the element matrices and the constant term as

$$\mathbf{K}'_e \coloneqq \frac{L}{N_e} \sum_{i=1}^{N_e} \lambda_i \, \mathbf{A}_i^T \mathbf{A}_i, \tag{3.11}$$

$$\mathbf{f}'_e \coloneqq \frac{L}{N_e} \sum_{i=1}^{N_e} \lambda_i \, \mathbf{A}_i^T e_i^{\varepsilon}, \tag{3.12}$$

$$c \coloneqq \frac{L}{N_e} \sum_{i=1}^{N_e} \lambda_i \left(e_i^{\varepsilon}\right)^2. \tag{3.13}$$

With these definitions, Eq. (3.10) takes the standard quadratic form

$$\Psi_e(\mathbf{u}_e) \;=\; \mathbf{u}_e^T \, \mathbf{K}'_e \, \mathbf{u}_e \;-\; 2 \, \mathbf{u}_e^T \, \mathbf{f}'_e \;+\; c. \tag{3.14}$$

Remark. (i) The term c in (3.13) depends only on measurements and does not affect the minimizer.

3.5 Governing equations and assembly

The stationary condition of the element functional $\Psi_e(\mathbf{u}_e)$ with respect to the nodal degrees of freedom yields the local normal equations:

$$\frac{\partial \Psi_e}{\partial \mathbf{u}_e} = 2 \, \mathbf{K}'_e \, \mathbf{u}_e - 2 \, \mathbf{f}'_e = \mathbf{0}, \tag{3.15}$$

which leads to the symmetric linear system

$$\boxed{\mathbf{K}'_e \, \mathbf{u}_e = \mathbf{f}'_e.} \tag{3.16}$$

Each element thus provides its own contribution to the global stiffness and force matrices. Following the standard finite element assembly procedure, all element matrices $\mathbf{K}'_e$ and vectors $\mathbf{f}'_e$ are combined according to the mesh connectivity, yielding the global system of equations:

$$\boxed{\mathbf{K}' \, \mathbf{u} = \mathbf{f}'.} \tag{3.17}$$

The vector $\mathbf{u}$ collects the global nodal degrees of freedom of the structure, while $\mathbf{K}'$ and $\mathbf{f}'$ represent the assembled stiffness and load matrices derived from the sensor information. Once the system (3.17) is solved for $\mathbf{u}$, the continuous displacement fields $u(x)$, $v(x)$, and $w(x)$ are reconstructed through the interpolation relations introduced in Chapter 2.

3.6 Discussion and consistency with classical iFEM

The present formulation is *agnostic* to the cross-section geometry: only the sensor offsets (y_i, z_i) enter the prediction operator $\mathbf{A}_i$ defined in Eq. (3.2). As a result, the SSB-iFEM can accommodate arbitrary cross-sections and sensor layouts, including configurations that are not aligned with canonical "faces" or that involve non-rectangular geometries.

When sensors are placed on different surfaces of the same cross-section, their offsets (y_i, z_i) naturally account for the geometric contribution of each location in the reconstructed strain field. Symmetric layouts (for instance, top/bottom or left/right pairs) implicitly capture both axial and bending effects, while completely unpaired configurations remain admissible within the same framework.

Therefore, the SSB-iFEM generalizes the classical iFEM approach: the displacement field is reconstructed directly from the measured strains without requiring pre-defined sensor pairing or symmetry conditions. In this sense, the SSB formulation extends the applicability of iFEM to more practical single-sided and non-symmetric instrumentation schemes, which are particularly relevant for aerospace and structural applications where sensor accessibility is limited.

Chapter 4

Verification in MATLAB

This chapter verifies the proposed inverse formulations for Euler–Bernoulli (EB) beams through reproducible MATLAB computations. Two inverse schemes are compared:

1. the *Single-Sensor-Based* iFEM (SSB-iFEM), driven by surface axial strains measured at arbitrary offsets (y_i, z_i) from the neutral line;

2. the *classical* EB iFEM, driven by the mid-line axial strain ε and the bending curvatures κ_{zz} and κ_{yy}.

All MATLAB computations strictly follow the Euler–Bernoulli sign convention defined in Chapter 2, namely $\phi_y = -w_{,x}$, $\omega_z = v_{,x}$, $\kappa_{zz} = -w_{,xx}$, and $\kappa_{yy} = -v_{,xx}$, ensuring full consistency between the theoretical operators and their numerical implementation.

4.1 From element-level operators to global solution

This section details the computational workflow adopted in MATLAB, from the evaluation of element-level operators to the global assembly and solution. The formulation is identical for the classical iFEM and the SSB-iFEM; only the definition of the local matrices differs (cf. Chapters 2 and 3).

(1) Element-level data and local operators. For each element e with length L_e and nodal DOFs $\mathbf{u}_e^\ell$ defined in the local reference frame, we evaluate:

- the shape functions N_1, N_2 and $H_1, \ldots, H_4$ and their second derivatives at the required stations (Section 2.2, Eqs. (2.18)–(2.21));

- the strain–displacement row operators $\mathbf{B}_u(\xi)$, $\mathbf{B}_w(\xi)$, $\mathbf{B}_v(\xi)$ at the prescribed stations $\xi_i = s_i/L_e$;
- the element matrices/vectors from the least-squares functional:
  - *classical* (mid-line $\varepsilon, \kappa_{zz}, \kappa_{yy}$):
    $$\mathbf{K}_e^\ell = \mathbf{A}_e + \mathbf{A}_{kzz} + \mathbf{A}_{kyy}, \qquad \mathbf{f}_e^\ell = \mathbf{b}_e + \mathbf{b}_{kzz} + \mathbf{b}_{kyy};$$
  - *SSB* (sensor-wise surface strains):
    $$\mathbf{K}_e^\ell = \frac{L_e}{N_e} \sum_{i=1}^{N_e} \lambda_i \, \mathbf{A}_i^\top \mathbf{A}_i, \qquad \mathbf{f}_e^\ell = \frac{L_e}{N_e} \sum_{i=1}^{N_e} \lambda_i \, \mathbf{A}_i^\top e_i^\varepsilon,$$
    with $\mathbf{A}_i = \mathbf{B}_u(\xi_i) + z_i \mathbf{B}_w(\xi_i) + y_i \mathbf{B}_v(\xi_i)$.

All matrices $\mathbf{K}_e^\ell$ are symmetric by construction. The weights λ_i activate/attenuate individual sensors and are set to 1 unless otherwise noted.

(2) Local-to-global transformation. Each element is defined in its own local reference frame $(x_{\text{loc}}, y_{\text{loc}}, z_{\text{loc}})$ for convenience in the kinematic evaluation. Quantities referred to this frame are denoted by the superscript (ℓ), while those expressed in the global frame (X, Y, Z) carry the superscript (g). To assemble the global equations, local operators are rotated into the global frame (X, Y, Z) by the reduced rotation operator $\mathbf{\Lambda}_e \in \mathbb{R}^{10\times 10}$, obtained from the full block-diagonal rotation blkdiag(R_e, R_e, R_e, R_e) (with $R_e \in \mathbb{R}^{3\times 3}$ the direction-cosine matrix of the element) by retaining the ten DOFs of the Euler–Bernoulli beam (five per node). The transformed contributions read

$$\mathbf{K}_e^g = \mathbf{\Lambda}_e^\top \, \mathbf{K}_e^\ell \, \mathbf{\Lambda}_e, \qquad \mathbf{f}_e^g = \mathbf{\Lambda}_e^\top \, \mathbf{f}_e^\ell.$$

At post–processing, local displacements follow from the global solution via $\mathbf{q}^\ell = \mathbf{\Lambda}_e^\top \, \mathbf{q}^g$.

(3) Connectivity and assembly. Each element e is associated with its connectivity array `C_Se(e,:)`, which stores the global degree-of-freedom (DOF) indices corresponding to the ten local variables $\{u_1, v_1, w_1, \phi_{y1}, \omega_{z1}, u_2, v_2, w_2, \phi_{y2}, \omega_{z2}\}$. Let $I_e \subset \{1, \ldots, n_{\text{DOF}}\}$ denote this ordered set of global indices. Within the element loop, the global stiffness matrix $\mathbf{K}$ and right-hand-side vector $\mathbf{F}$ are assembled as

$$\mathbf{K}(I_e, I_e) \; \mathrel{+}= \; \mathbf{K}_e^{(g)}, \qquad \mathbf{F}(I_e) \; \mathrel{+}= \; \mathbf{F}_e^{(g)}.$$

Here, $\mathbf{K}_e^{(g)}$ and $\mathbf{F}_e^{(g)}$ are the element contributions rotated into the global frame. All matrices are stored and initialized before assembly. Symmetry of each element stiffness matrix $\mathbf{K}_e^{(g)}$ ensures that the assembled system remains symmetric.

(4) Boundary conditions and solution. Essential boundary conditions (clamps or prescribed DOFs) are enforced by eliminating the corresponding rows and columns of the global system. Let `fixedDOF` be the vector of constrained DOF indices and `freeDOF` the complementary set. The reduced system

$$\mathbf{K}_{FF}\,\mathbf{q}_F = \mathbf{F}_F,$$

is then solved directly in MATLAB.

(5) Recovery and field reconstruction. From the global displacement vector $\mathbf{q}$, the local element DOFs are recovered as

$$\mathbf{q}_e^{(\ell)} = \mathbf{\Lambda}_e\,\mathbf{q}_{I_e},$$

where $\mathbf{\Lambda}_e$ is the element rotation matrix mapping global to local coordinates. The continuous displacement fields along the element are then reconstructed by the standard interpolation relations:

$$\begin{aligned} u(s) &= N_1(s)\,u_1 + N_2(s)\,u_2, \\ w(s) &= H_1(s)\,w_1 - L\,H_2(s)\,\phi_{y1} + H_3(s)\,w_2 - L\,H_4(s)\,\phi_{y2}, \\ v(s) &= H_1(s)\,v_1 + L\,H_2(s)\,\omega_{z1} + H_3(s)\,v_2 + L\,H_4(s)\,\omega_{z2}. \end{aligned}$$

Station-wise strains (mid-line and/or surface) are then evaluated using the operators $\mathbf{B}_u$, $\mathbf{B}_w$, and $\mathbf{B}_v$.

Algorithmic summary. For clarity, the overall computational pipeline is:

1. Build the matrices R_e, the reduced rotation operators $\mathbf{\Lambda}_e$, and the connectivity sets I_e for all elements.
2. For each element e: evaluate the strain–displacement operators $\mathbf{B}_u, \mathbf{B}_v, \mathbf{B}_w$ at the prescribed sensor stations; compute the local matrices and vectors $(\mathbf{K}_e^{(\ell)}, \mathbf{f}_e^{(\ell)})$; rotate them to the global frame to obtain $(\mathbf{K}_e^{(g)}, \mathbf{f}_e^{(g)})$.
3. Assemble the global stiffness matrix $\mathbf{K}$ and right-hand-side (load-equivalent) vector $\mathbf{F}$ over the mesh by accumulation over all elements.
4. Apply essential boundary conditions to form the reduced system, and solve for the free degrees of freedom $\mathbf{q}_F$.
5. Recover the local displacements $\mathbf{q}_e^{(\ell)}$, reconstruct the fields u, v, w, and evaluate comparisons.

Implementation notes. All computations are implemented in MATLAB using fully vectorized operations. The global stiffness matrix $\mathbf{K}$ and right-hand-side vector $\mathbf{F}$ are stored and assembled by direct accumulation over the global indices I_e. The global numbering of the degrees of freedom follows the consistent order $\{u, v, w, \phi_y, \omega_z\}$ per node.

The sensor weights λ_i are defined element-wise as row vectors and can take any value in $[0, 1]$. Setting $\lambda_i = 0$ effectively disables a sensor without altering matrix dimensions, allowing the simulation of missing or excluded measurements.

All local operators strictly adhere to the sign convention $\phi_y = -w_{,x}$ and $\omega_z = +v_{,x}$, ensuring full consistency with the theoretical formulation in Chapter 2. During post–processing, both the predicted and analytical strain fields are evaluated under the same orientation and conventions, enabling a direct and unambiguous comparison of results.

4.2 Numerical Scenarios and Validation Strategy

The numerical validation of the proposed formulation is carried out through a series of simulation scenarios of increasing complexity. Each scenario represents a distinct test case designed to assess specific aspects of the *Single-Sensor-Based* inverse Finite Element Method (SSB-iFEM) when applied to Euler–Bernoulli beam elements.

Objectives. The primary goals of the numerical campaign are:

- to verify the correctness and numerical consistency of the implemented MATLAB code;
- to assess the accuracy of displacement-field reconstruction under different sensor layouts;
- to investigate the sensitivity of the SSB-iFEM to the number and spatial distribution of strain sensors;
- and, where applicable, to compare the SSB-iFEM results with those of the classical iFEM formulation.

Scenario design. The analysis proceeds from simple, fully controlled cases to more realistic configurations.

- The first set of scenarios (A–C) involves *simple benchmark beams* with analytically prescribed displacement fields, from which the corresponding surface–strain inputs are computed exactly. These cases serve to validate the element operators and verify the correctness of the implementation under controlled layouts.
- Subsequent sets will consider *more complex beam geometries* (e.g., L-, Z-shaped members) and boundary conditions. For each such beam, the same four analyses will be repeated systematically: (i) all four faces instrumented and paired (SSB vs. classical iFEM); (ii) three sensors with two paired and one single; (iii) three unpaired sensors (two top, one bottom); (iv) three unpaired sensors on the same face. This pattern isolates the effect of sensor pairing/reduction on observability and accuracy.

Comparison and evaluation. For each scenario, the reconstructed displacement components are compared against their analytical (or reference) counterparts. Relative errors are reported both station-wise and globally. In Scenario A, SSB and classical iFEM are evaluated under identical, noiseless conditions to assess numerical equivalence. Scenarios B, C and D focus on the SSB formulation under reduced, unpaired layouts on the mid-width line ($y = 0$), where only u and w are reconstructed (no sensitivity to κ_{yy}).

Common framework. All scenarios share a consistent computational setup:

- Euler–Bernoulli beam elements with five DOFs per node;
- MATLAB implementation (vectorized element assembly);
- Sensor layout is specified *per element*: for complex beams, each EB element carries its own stations (defined in the element's local x-abscissa) according to the three analysis patterns.
- identical preprocessing of synthetic (noise-free) surface–strain data and uniform channel weights unless stated otherwise;
- identical post-processing for strain residuals, station-wise comparisons, and field plots;
- error metrics computed on the reconstructed displacements.

Structure of presentation. Each scenario is presented according to the following structure:

1. **Setup and input data:** geometry, boundary conditions, and sensor configuration;
2. **Reference solution:** analytical or external dataset used for validation;
3. **Reconstruction results:** displacement fields, numerical errors, and diagnostic quantities;
4. **Discussion:** interpretation of accuracy and sensitivity trends.

In the following sections, each scenario is detailed according to this structure, with direct numerical comparisons and discussion of the most relevant outcomes.

Chapter 5

Simple Beams

5.1 Scenario A: straight cantilever beam, single element

1) Setup and input data

Straight prismatic Euler–Bernoulli (EB) beam of length $L = 10m$ with rectangular cross-section $b = h = 0.1m$, axis aligned with the global x-direction. A *clamped end* (cantilever root) is imposed at $x = 0$. The element local frame $(x_{\text{loc}}, y_{\text{loc}}, z_{\text{loc}})$ is chosen coincident with the global (x, y, z); consequently, the element rotation operator is the identity on the EB degrees of freedom (DOFs) and the reduced mapping $\mathbf{\Lambda}_e$ simply selects the ten translational/rotational DOFs.

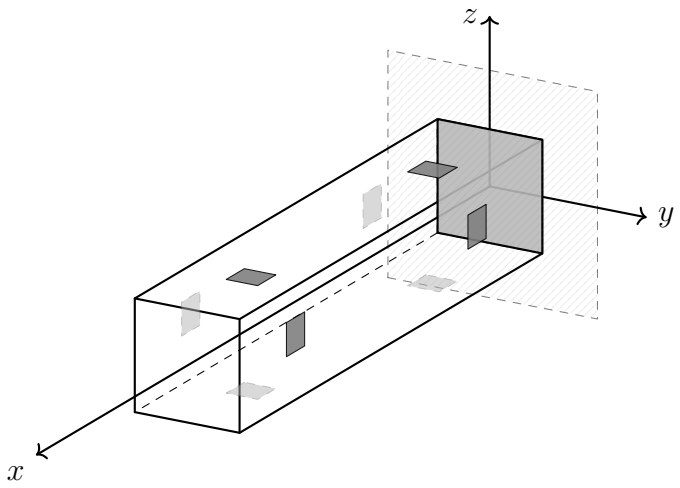

Figure 5.1: Scenario A: straight prismatic EB cantilever (clamped end at $x = 0$, grey plate and hatched background). Global frame (x, y, z) shown at the centroid of the left section. Surface–strain sensors (squares) are mounted on the four side faces at two axial stations, $x/L = \{0.2, 0.8\}$: darker squares indicate sensors on the visible faces ($y = B,\ z = H$), lighter dashed squares those on the hidden faces ($y = 0,\ z = 0$). Section width b is along y, height h along z.

Remark on magnitudes and units. The analytical fields used below are low-degree polynomials chosen to test numerical consistency rather than to model a specific load case. Some magnitudes are not representative of a physical cantilever under standard loading; they serve only as exact targets for reconstruction. Strains are dimensionless; curvatures κ_{yy}, κ_{zz} have units m^{-1}.

2) Reference solution

Prescribed analytical displacement fields (chosen to satisfy the clamped boundary at $x = 0$):

$$\begin{aligned} u(x) &= 4x, \\ v(x) &= -14x^3 + 6x^2, \\ w(x) &= 7x^3 + 4x^2. \end{aligned}$$

By construction, the fields obey the EB clamped boundary conditions at $x = 0$:

$$u(0) = v(0) = w(0) = 0, \qquad v_{,x}(0) = 0, \qquad w_{,x}(0) = 0,$$

so that both rotations vanish at $x = 0$.

Associated EB strain measures:

$$\begin{aligned}\varepsilon(x) &= u_{,x}(x) = 4,\\ \kappa_{zz}(x) &= -w_{,xx}(x) = -(42x+8),\\ \kappa_{yy}(x) &= -v_{,xx}(x) = 84x - 12.\end{aligned}$$

Two stations are used at $\xi = \{0.2, 0.8\}$ (i.e. $s = \{2, 8\}\,\mathrm{m}$). For the *SSB-iFEM* (sensor-based), surface strains are generated as

$$\varepsilon_s(x_i, y_i, z_i) = \varepsilon(x_i) + z_i\,\kappa_{zz}(x_i) + y_i\,\kappa_{yy}(x_i),$$

with $(y_i, z_i) \in \{(0, \pm h/2), (\pm b/2, 0)\}$. For the *classical* iFEM, the channels $\{\varepsilon, \kappa_{zz}, \kappa_{yy}\}$ are sampled directly at the same abscissae. Uniform weights $\lambda_i = 1$ are used for all active channels.

3) Reconstruction results

Element matrices are formed in the local frame, mapped to the global frame via $\mathbf{\Lambda}_e$, assembled at the structure level, and the clamped end at $x = 0$ is enforced by DOF elimination. The reduced linear system is solved by direct factorization.

Table 5.1 compares analytical and reconstructed displacements at the stations. In this noiseless consistency test, SSB and classical iFEM coincide at machine precision (max DOF difference $= 2.60 \times 10^{-15}$). Relative errors are $< 10^{-12}$ for u and w, while v exhibits a small but nonzero discrepancy because it is obtained by twice integrating κ_{yy}, which is estimated from face–strain differences and is therefore more sensitive to numerical round-off; the relative errors are 0.034% at $s = 2m$ and 0.0057% at $s = 8m$.

Table 5.1: Scenario A — Displacements at stations $s = \{2, 8\}\,\mathrm{m}$. Values in metres; rel. err refers to SSB vs. analytical.

Quantity	Station	Unit	Analytical	SSB-iFEM	Classical	rel. err (SSB)
u	$s = 2$	m	8.0000	8.0000	8.0000	$< 10^{-12}$
	$s = 8$	m	32.0000	32.0000	32.0000	$< 10^{-12}$
w	$s = 2$	m	72.0000	72.0000	72.0000	$< 10^{-12}$
	$s = 8$	m	3840.0000	3840.0000	3840.0000	$< 10^{-12}$
v	$s = 2$	m	−88.0000	−87.9700	−87.9700	3.40×10^{-4} (0.034%)
	$s = 8$	m	−6784.0000	−6783.6159	−6783.6159	5.66×10^{-5} (0.0057%)

Figure 5.2 reports the pointwise differences $\Delta u(s) = u_{\mathrm{SSB}}(s) - u_{\mathrm{CLS}}(s)$, $\Delta w(s)$, and $\Delta v(s)$, which remain at numerical round-off over the whole span.

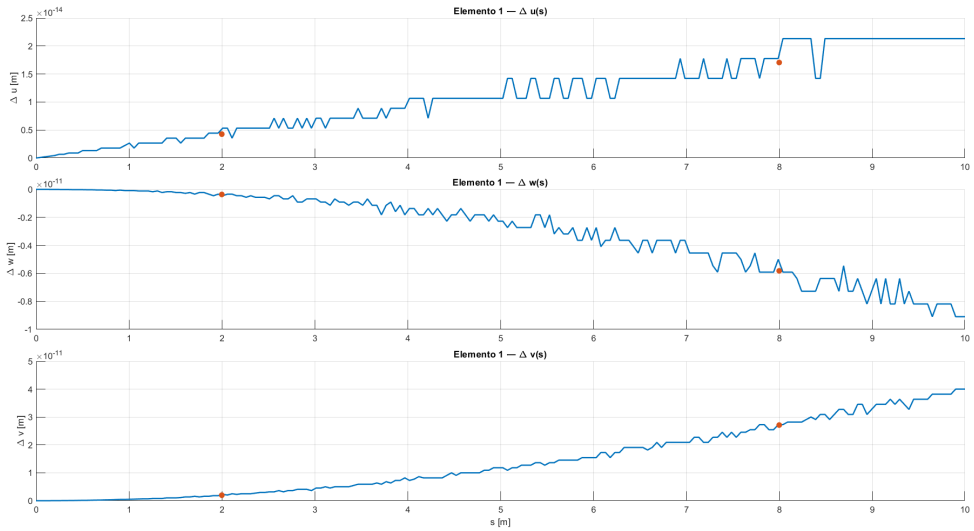

Figure 5.2: Scenario A — Pointwise differences $\Delta u(s)$, $\Delta w(s)$, $\Delta v(s)$ between SSB and classical iFEM. Markers denote the stations $s = \{2, 8\}$ m.

Figure 5.3 compares analytical displacements (solid lines) with SSB (circles) and classical (squares) at the two stations; the symbols overlap the analytical curves within plotting resolution for u and w, while the minor offset in v at $s = 8m$ matches Table 5.1.

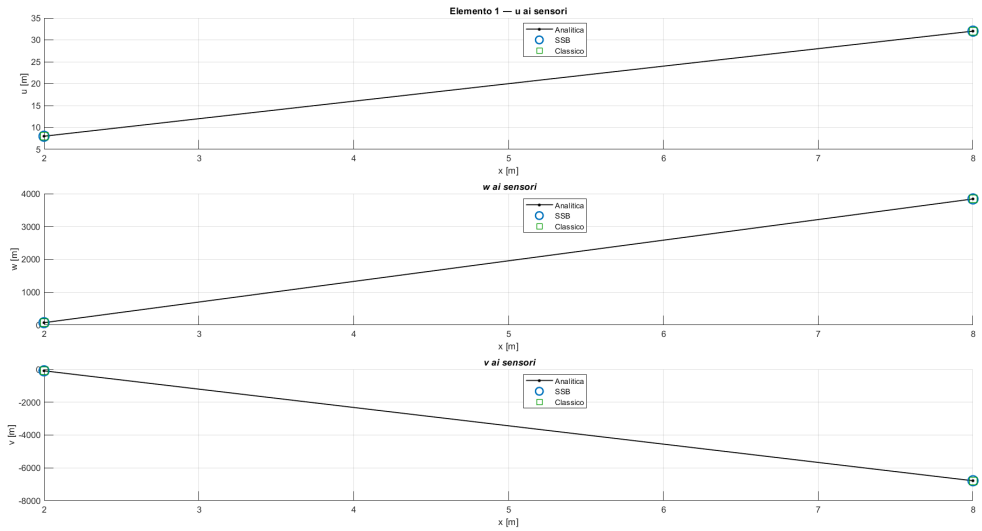

Figure 5.3: Scenario A — Analytical displacements (lines) vs. SSB (circles) and classical (squares) at the stations.

4) Discussion

- **Consistency.** With coincident local/global frames and noiseless inputs, SSB and classical iFEM deliver indistinguishable reconstructions (max DOF difference 2.60×10^{-15}); the SSB–classical field differences (Fig. 5.2) sit at numerical round-off over the span.
- **Equivalence.** With identical station abscissae and uniform weights, SSB-iFEM (surface strains on the four faces) and the classical iFEM (direct $\{\varepsilon, \kappa_{zz}, \kappa_{yy}\}$) are equivalent on this scenario; the reconstructions overlap at machine precision in Figs. 5.2–5.3 and in the diagnostics, as expected.
- **Sensor layout.** With sensors installed on all four faces and paired at each station, the full displacement field can be reconstructed. Subsequent scenarios consider reduced layouts (i.e., not all four faces and not always paired).

5.2 Scenario B: single element, *unpaired* sensors on mid-width ($y = 0$; SSB only)

1) Setup and input data

Straight prismatic Euler–Bernoulli (EB) beam of length $L = 10m$ with rectangular cross-section $b = h = 0.1m$, axis aligned with the global x-direction. A *clamped end* (cantilever root) is imposed at $x = 0$. The element local frame $(x_{\text{loc}}, y_{\text{loc}}, z_{\text{loc}})$ is chosen coincident with the global (x, y, z); consequently, the element rotation operator is the identity on the EB degrees of freedom (DOFs) and the reduced mapping $\mathbf{\Lambda}_e$ simply selects the ten translational/rotational DOFs.

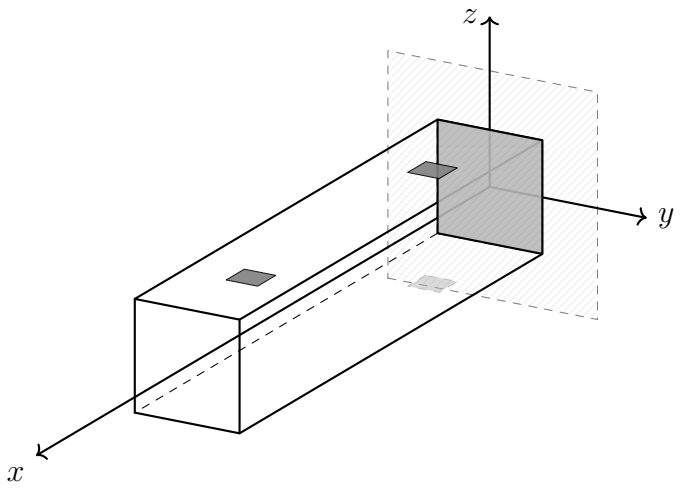

Figure 5.4: Scenario B: SSB-only with *unpaired* sensors on the mid-width line ($y = 0$). Two sensors at $x/L = 0.2$ (top and bottom faces at $z = \pm h/2$) and one sensor at $x/L = 0.8$ (top face). This layout excites ε and κ_{zz} via the z-offset, but provides no sensitivity to κ_{yy} (no y-offset); accordingly, v is not reconstructed in this scenario for a cleaner analysis focused on u and w. Section width b is along y, height h along z.

2) Reference solution

Analytical displacement fields and EB measures as in Scenario A (they satisfy the clamped boundary conditions at $x = 0$). *Note.* In this scenario only u and w are reconstructed; v is not estimated because the chosen layout has no lateral sensors (no sensitivity to κ_{yy}).

Sensor layout (SSB-only). Unpaired single-surface stations on the mid-width line ($y = 0$): two sensors at $\xi = 0.2$ (top and bottom faces) and one

sensor at $\xi = 0.8$ (top face), i.e.

$$(y, z) \in \left\{ \left(0, \tfrac{h}{2}\right)_{\xi=0.2}, \ \left(0, -\tfrac{h}{2}\right)_{\xi=0.2}, \ \left(0, \tfrac{h}{2}\right)_{\xi=0.8} \right\}.$$

With $y_i = 0$, each surface strain reduces to

$$\varepsilon_s(x_i, 0, z_i) = \varepsilon(x_i) + z_i\, \kappa_{zz}(x_i) = \Big(\mathbf{B}_u(x_i) + z_i\, \mathbf{B}_w(x_i)\Big)\, \mathbf{u}_e \ =: \ \mathbf{A}_i\, \mathbf{u}_e.$$

Exact surface-strain values ε_s are computed at $s = \{2, 2, 8\}$ m ($\xi = \{0.2, 0.2, 0.8\}$). Uniform weights are used ($\lambda_i = 1$).

3) Reconstruction results

Element matrices are formed in the local frame, mapped to the global frame via $\mathbf{\Lambda}_e$, assembled at the structure level, and the clamped end at $x = 0$ is enforced by DOF elimination. The reduced linear system is solved by direct factorization.

Table 5.2 reports analytical vs SSB-iFEM values at the distinct stations $s = \{2, 8\}$ m (the two sensors at $s = 2$ share the same u, w). Stationwise relative errors are 0 for u; for w they are 6.32×10^{-15} at $s = 2m$ and 1.42×10^{-15} at $s = 8m$.

Table 5.2: Scenario B — Analytical vs SSB-iFEM displacements at stations $s = \{2, 8\}$ m ($y = 0$ layout; only u, w are observable). Values in metres; rel. err refers to SSB vs. analytical.

Quantity	Station	Unit	Analytical	SSB-iFEM	rel. err (SSB)
u	$s = 2$	m	8.0000	8.0000	0
	$s = 8$	m	32.0000	32.0000	0
w	$s = 2$	m	72.0000	72.0000	6.32×10^{-15}
	$s = 8$	m	3840.0000	3840.0000	1.42×10^{-15}

Figure 5.5 shows the reconstructed fields along the element.

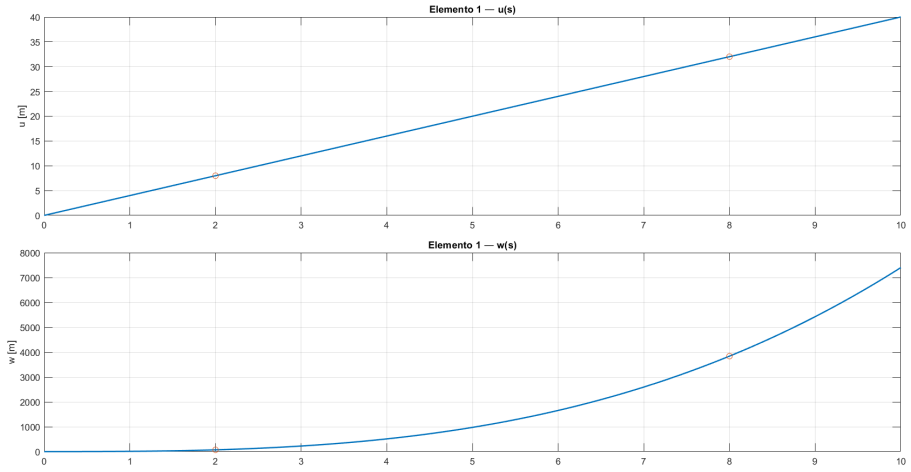

Figure 5.5: Scenario B — Reconstructed fields $u(s)$ and $w(s)$ (SSB only; sensors on $y = 0$). Markers denote the sensor abscissae. u, w match the analytical trend within numerical precision.

Figure 5.6 overlays analytical values (solid lines) and SSB predictions (markers) at the three sensor abscissae $s = \{2, 2, 8\}$ m. The double marker at $s = 2$ corresponds to the top/bottom sensors at the same station: they share the same u, w but contribute with opposite sign to κ_{zz} in ε_s.

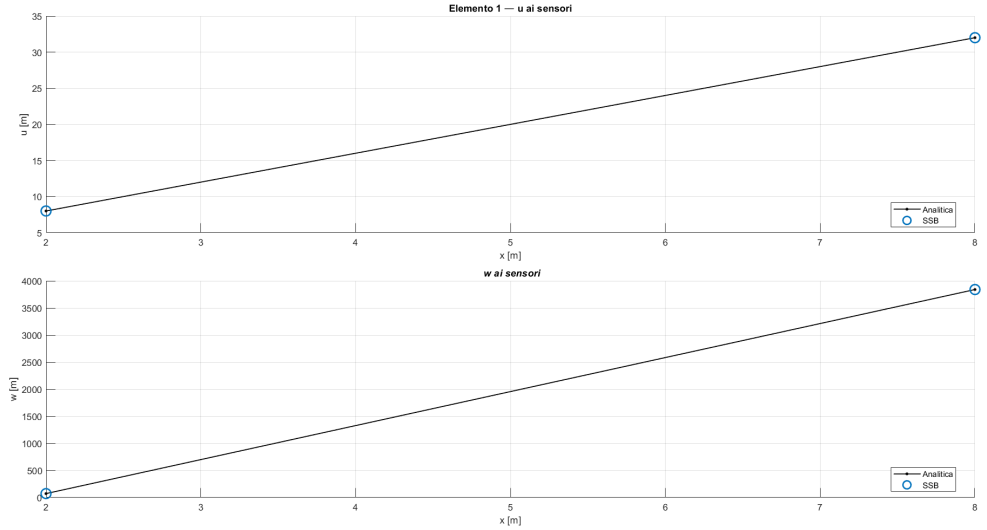

Figure 5.6: Scenario B — Analytical (lines) vs SSB (markers) at $s = \{2, 2, 8\}$ m. Top/bottom sensors at $s = 2$ lie at $z = \pm h/2$ (with $y = 0$): they provide identical u, w but opposite bending contribution in the surface-strain measurement $\varepsilon_s = \varepsilon + z\,\kappa_{zz}$.

4) Discussion

- **Consistency.** With coincident local/global frames and noiseless inputs, the observed fields u and w match the analytical solution at numerical round-off.
- **Observability.** A mid-width ($y = 0$) layout excites ε and κ_{zz} (via the z-offset), enabling accurate recovery of u and w; v is not reconstructed here because the layout has no lateral sensors (no sensitivity to κ_{yy}).
- **Sensor layout.** Compared to Scenario A, this reduced and unpaired layout does not provide full-field observability; adding sensors off the mid-width line and pairing faces restores sensitivity to κ_{yy} and the reconstruction of v.
- **SSB vs. classical under unpaired layouts.** In beam problems, the SSB formulation operates directly on surface–strain data; even without paired sensors on all faces, as long as the active faces provide sensitivity to the target curvature(s), the corresponding displacement components can be recovered. By contrast, the classical iFEM requires the channels $\{\varepsilon, \kappa_{zz}, \kappa_{yy}\}$ explicitly; in practice this entails paired sensors (top–bottom and/or left–right) to form curvature estimates.

5.3 Scenario C: single element, *unpaired* sensors on mid-width ($y = 0$; SSB only)

1) Setup and input data

Straight prismatic Euler–Bernoulli (EB) beam of length $L = 10m$ with rectangular cross-section $b = h = 0.1m$, axis aligned with the global x-direction. A *clamped end* (cantilever root) is imposed at $x = 0$. The element local frame $(x_{\text{loc}}, y_{\text{loc}}, z_{\text{loc}})$ is chosen coincident with the global (x, y, z); consequently, the element rotation operator is the identity on the EB degrees of freedom (DOFs) and the reduced mapping $\mathbf{\Lambda}_e$ simply selects the ten translational/rotational DOFs.

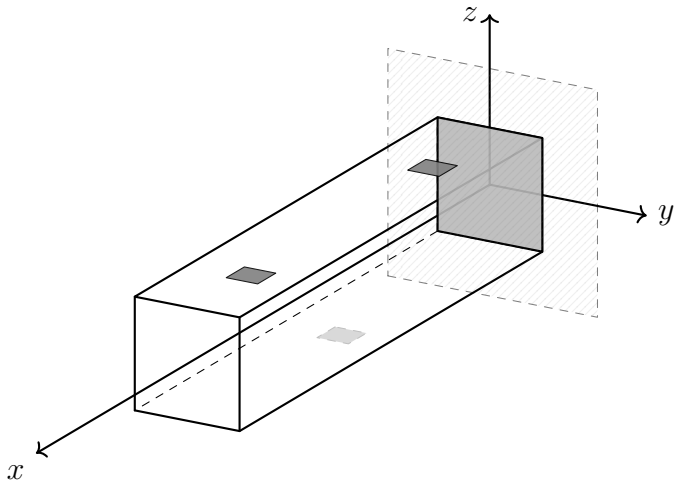

Figure 5.7: Scenario C: SSB-only with *unpaired* sensors on the mid-width line ($y = 0$). Three stations at $x/L = \{0.2, 0.5, 0.8\}$: top–bottom–top faces at $z = \{+h/2, -h/2, +h/2\}$ (with $y = 0$). This layout excites ε and κ_{zz} via the z-offset, but provides no sensitivity to κ_{yy} (no y-offset); accordingly, v is not reconstructed in this scenario for a cleaner analysis focused on u and w. Section width b is along y, height h along z.

2) Reference solution

Analytical displacement fields and EB measures as in Scenario A (they satisfy the clamped boundary conditions at $x = 0$). *Note.* In this scenario only u and w are reconstructed; v is not estimated because the chosen layout has no lateral sensors (no sensitivity to κ_{yy}).

Sensor layout (SSB-only). Unpaired single-surface stations on the mid-width line ($y = 0$):

$$(y, z) \in \left\{ \left(0, \tfrac{h}{2}\right)_{\xi=0.2}, \ \left(0, -\tfrac{h}{2}\right)_{\xi=0.5}, \ \left(0, \tfrac{h}{2}\right)_{\xi=0.8} \right\},$$
$$\xi = \{0.2,\, 0.5,\, 0.8\} \Rightarrow s = \{2,\, 5,\, 8\}\,\mathrm{m}.$$

With $y_i = 0$, each surface strain reduces to

$$\varepsilon_s(x_i, 0, z_i) = \varepsilon(x_i) + z_i\, \kappa_{zz}(x_i) = \Big(\mathbf{B}_u(x_i) + z_i\, \mathbf{B}_w(x_i)\Big)\, \mathbf{u}_e \ =: \ \mathbf{A}_i\, \mathbf{u}_e.$$

Exact surface-strain values ε_s are computed at $s = \{2, 5, 8\}\,\mathrm{m}$ with uniform weights $\lambda_i = 1$.

3) Reconstruction results

Element matrices are formed in the local frame, mapped to the global frame via $\mathbf{\Lambda}_e$, assembled at the structure level, and the clamped end at $x = 0$ is enforced by DOF elimination. The reduced linear system is solved by direct factorization.

Table 5.3 reports analytical vs SSB-iFEM values at the stations $s = \{2, 5, 8\}\,\mathrm{m}$. Stationwise relative errors are 0 for u; for w they are 0 at $s = 2m$, 1.17×10^{-16} at $s = 5m$, and 3.55×10^{-16} at $s = 8m$.

Table 5.3: Scenario C — Analytical vs SSB-iFEM displacements at stations $s = \{2, 5, 8\}\,\mathrm{m}$ ($y = 0$ layout; only u, w are observable). Values in metres; rel. err refers to SSB vs. analytical.

Quantity	Station	Unit	Analytical	SSB-iFEM	rel. err (SSB)
u	$s = 2$	m	8.0000	8.0000	0
	$s = 5$	m	20.0000	20.0000	0
	$s = 8$	m	32.0000	32.0000	0
w	$s = 2$	m	72.0000	72.0000	0
	$s = 5$	m	975.0000	975.0000	1.17×10^{-16}
	$s = 8$	m	3840.0000	3840.0000	3.55×10^{-16}

Figure 5.8 shows the reconstructed fields along the element.

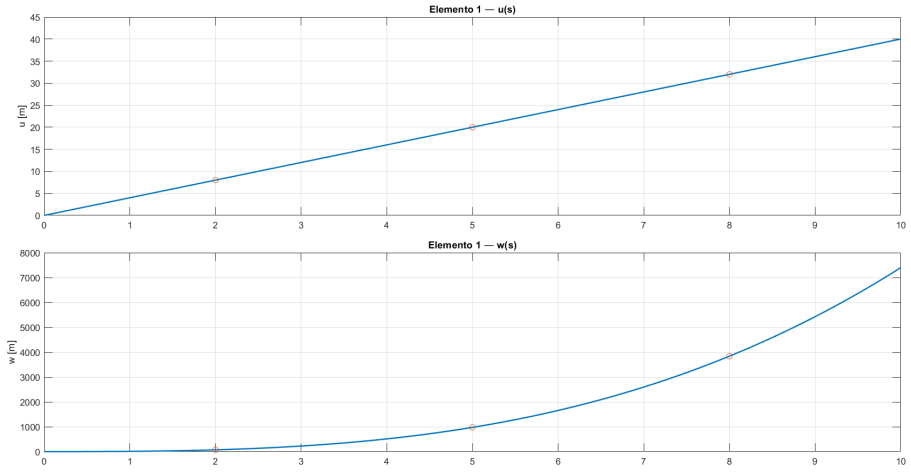

Figure 5.8: Scenario C — Reconstructed fields $u(s)$ and $w(s)$ (SSB only; sensors on $y = 0$). Markers denote the sensor abscissae $s = \{2, 5, 8\}$ m. u, w match the analytical trend within numerical precision.

Figure 5.9 overlays analytical values (solid lines) and SSB predictions (markers) at the three sensor abscissae.

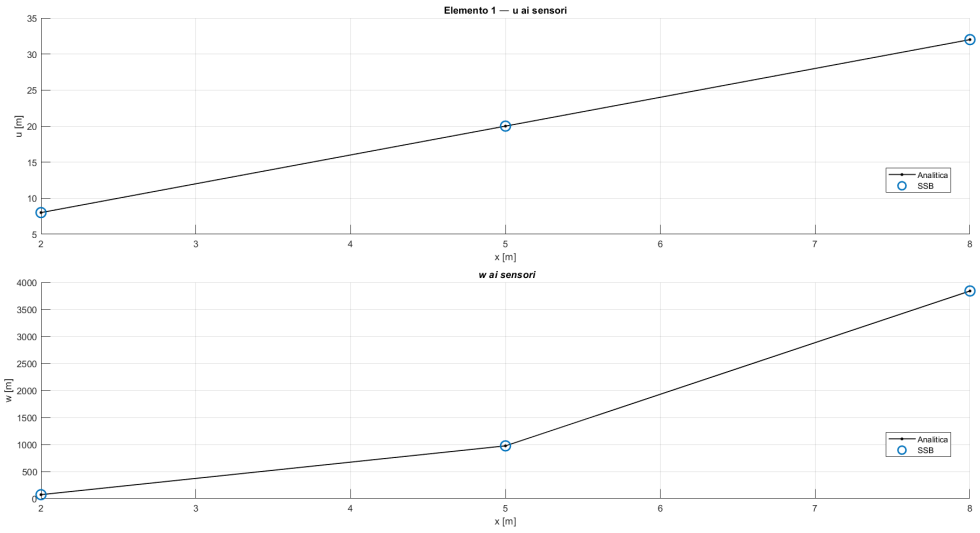

Figure 5.9: Scenario C — Analytical (lines) vs SSB (markers) at $s = \{2, 5, 8\}$ m. Top/bottom sensors ($z = \pm h/2$, $y = 0$) provide identical u, w but opposite bending contribution in the surface-strain measurement $\varepsilon_s = \varepsilon + z\,\kappa_{zz}$.

4) Discussion

- **Consistency.** With coincident local/global frames and noiseless inputs, the observed fields u and w match the analytical solution at numerical round-off.
- **Observability.** A mid-width ($y = 0$) layout excites ε and κ_{zz} (via the z-offset), enabling accurate recovery of u and w; v is not reconstructed here because the layout has no lateral sensors (no sensitivity to κ_{yy}).
- **Sensor layout.** Compared to Scenario A, this reduced and unpaired layout does not provide full-field observability; adding sensors off the mid-width line and pairing faces restores sensitivity to κ_{yy} and the reconstruction of v.
- **SSB under unpaired layouts.** In the beam case, even with only three single (unpaired) sensors - provided that at least one sensor lies on each of the two opposite faces involved (e.g., top and bottom for κ_{zz}) - the SSB formulation accurately reconstructs the corresponding displacement field (here u and w).

Chapter 6

Complex Beam Configurations

6.1 Overview

This chapter extends the verification campaign of Chapter 4 to *complex beam configurations*, i.e. multi-element assemblies with changes of orientation, joints, and boundary conditions that are representative of practical aerospace and mechanical structures. The goal is to assess the performance and practicality of the *Single-Sensor-Based* iFEM (SSB-iFEM) on geometries where local-to-global frame rotations, corner continuity, and limited sensor accessibility play a primary role.

Scope and questions. We address the following questions: (i) how closely SSB-iFEM matches the classical Euler–Bernoulli (EB) iFEM when both are provided with equivalent information; (ii) to what extent accurate reconstruction can be maintained with reduced and/or unpaired sensor layouts constrained by accessibility; (iii) how geometry-induced rotations and joints (corners) impact observability and the reconstruction of the target displacement components.

Test matrix. Three structures are considered: (1) a cantilever L-beam (two EB elements joined at a right angle); (2) a cantilever Z-beam (three EB elements with two corners); (3) a T-beam with double pinned ends (pinned–pinned global boundary conditions with a branching joint). For each structure, four analysis cases are run with station abscissae expressed in parent coordinates $\xi = x/L$:

- **Case A** — *Classical iFEM vs SSB-iFEM (baseline)*: full, paired instrumentation; direct comparison of reconstructions.

- **Case B** — *SSB-iFEM, paired at* $\xi = 0.2$ *+ top at* $\xi = 0.8$: reduced set with one paired station and one single-sided sensor.
- **Case C** — *SSB-iFEM, top at* $\xi = 0.2, 0.8$ *+ bottom at* $\xi = 0.5$: three unpaired sensors distributed along the span.
- **Case D** — *SSB-iFEM, top-only at* $\xi = 0.2, 0.5, 0.8$: single-sided instrumentation (most restrictive accessibility scenario).

Unless otherwise noted, sensors are placed on the mid-width line ($y = 0$); their offsets enter the prediction operator via $\mathbf{A}_i = \mathbf{B}_u(\xi_i) + z_i\,\mathbf{B}_w(\xi_i) + y_i\,\mathbf{B}_v(\xi_i)$ (cf. Chapter 3).

Kinematics, frames, and assembly. All analyses employ EB kinematics and the sign convention of Chapter 2 ($\phi_y = -w_{,x}$, $\omega_z = v_{,x}$, $\kappa_{zz} = -w_{,xx}$, $\kappa_{yy} = -v_{,xx}$). Element operators are evaluated in local frames and mapped to the global frame through the reduced rotation $\mathbf{\Lambda}_e$; corner nodes enforce compatibility across incident elements. The global system is assembled and essential boundary conditions are applied by DOF elimination, as in Section 4.1.

Data generation and reference solution (forward FEM). Unlike Chapter 4, where analytical fields were prescribed, here both the input measurements and the reference outputs are produced by an independent forward FEM tool (provided by the advisor). For each structure and case, we supply to the forward solver the geometry (nodal coordinates, element connectivity), boundary conditions, and external loads. The solver returns: (i) the global nodal displacement vector $\mathbf{q}^{\text{ref}}$ used as reference solution; and (ii) section/surface strain measures sampled along each element at the prescribed parent abscissae.

Measurements for the inverse analyses are then prepared as follows:

- **SSB-iFEM input (surface strain).** At each sensor station with local offsets (y_i, z_i), the available surface axial strains ε_s are passed *directly* to the inverse formulation as $\varepsilon_s(x_i, y_i, z_i)$.
- **Classical iFEM input (mid-line & curvatures).** The channels $\{\varepsilon, \kappa_{zz}, \kappa_{yy}\}$ are *constructed* from paired surface measurements taken at the same abscissa using Euler–Bernoulli kinematics.
  For symmetric top/bottom stations at $z = \pm h/2$ this reduces to $\varepsilon = (\varepsilon_{\text{top}} + \varepsilon_{\text{bot}})/2$ and $\kappa_{zz} = (\varepsilon_{\text{top}} - \varepsilon_{\text{bot}})/h$. Analogously, with left/right sensors at $y = \pm b/2$: $\kappa_{yy} = (\varepsilon_{\text{right}} - \varepsilon_{\text{left}})/b$.
- **Reference for comparison.** The nodal DOFs $\mathbf{q}^{\text{ref}}$ from the forward solver provide the target displacements for all error metrics and plots.

The forward FEM uses the same Euler–Bernoulli kinematics and sign con-

vention as in Chapter 2, ensuring consistent local/global frames and station definitions. Material properties and loads are needed only by the forward solver to generate the synthetic measurements and reference solution; the inverse formulations themselves do not require them. Unless otherwise stated, measurements are noise-free and all active sensors have unit weight ($\lambda_i = 1$).

Observability considerations. As discussed in Chapter 3, the displacement components that are observable depend on the available offsets (y_i, z_i): offsets in z provide sensitivity to κ_{zz} (bending about y) and thus to w; offsets in y provide sensitivity to κ_{yy} (bending about z) and thus to v. Layouts with $y_i = 0$ (single-sided along the mid-width) are therefore informative for (u, w, ϕ_y) but do not excite v unless at least one sensor has $y_i \neq 0$. The chapter deliberately includes single-sided and unpaired layouts to reflect realistic accessibility constraints.

Evaluation metrics and visualisation. For each case we report: (i) nodal errors on the observed DOFs in ∞- and 2-norms; (ii) station-wise field comparisons along each element; and (iii) the *static deformed configuration* of the structure, plotted in the global frame to qualitatively illustrate the reconstructed shape. Unless stated otherwise, measurements are noise-free and all active sensors carry unit weight $\lambda_i = 1$.

6.2 Structure 1: Cantilever L-Beam

Geometry and mesh. The L-beam is modeled as a two–element Euler–Bernoulli (EB) assembly lying in the global X–Z plane. The nodal coordinates (in metres) are

$$\mathbf{x}_1 = (0, 0, 0), \qquad \mathbf{x}_2 = (3L, 0, 0), \qquad \mathbf{x}_3 = (3L, 0, 2L), \qquad L = 10.$$

Element connectivity is $\mathcal{C}_e = \{(1, 2), (2, 3)\}$. Each element adopts a local frame with x_{loc} aligned with the element axis, $y_{\text{loc}} \parallel Y$, and $z_{\text{loc}} = x_{\text{loc}} \times y_{\text{loc}}$, so that $\mathbf{\Lambda}_e$ consistently maps local EB DOFs to the global frame.

Cross-section. A constant rectangular cross-section is assumed with width $b = 1$ (along y) and height $h = 1$ (along z). Only geometric data enter the inverse formulation; material properties are not required by iFEM.

Kinematics and sign conventions. All operators follow the EB kinematics and the sign convention of Chapter 2: $\phi_y = -w_{,x}$, $\omega_z = v_{,x}$, $\kappa_{zz} = -w_{,xx}$, $\kappa_{yy} = -v_{,xx}$. Element operators are evaluated in local frames and rotated to the global frame by $\mathbf{\Lambda}_e$ prior to assembly.

Boundary conditions. A clamp is imposed at node 1 (all five EB DOFs fixed). To restrict the analysis to in-plane response (X–Z), the out-of-plane DOFs are suppressed at the free nodes by enforcing $v = \omega_z = 0$ at nodes 2 and 3. Corner compatibility at node 2 is enforced automatically by the common nodal DOFs.

Static deformed configuration (visualization). Under a nodal load at node 3 along global $+X$, $\mathbf{F} = \{10^{-4}, 0, 0\}$ N, the static deformed configuration is plotted (Figure 6.1). This visualization is independent of the inverse formulation and is common to all cases A–D.

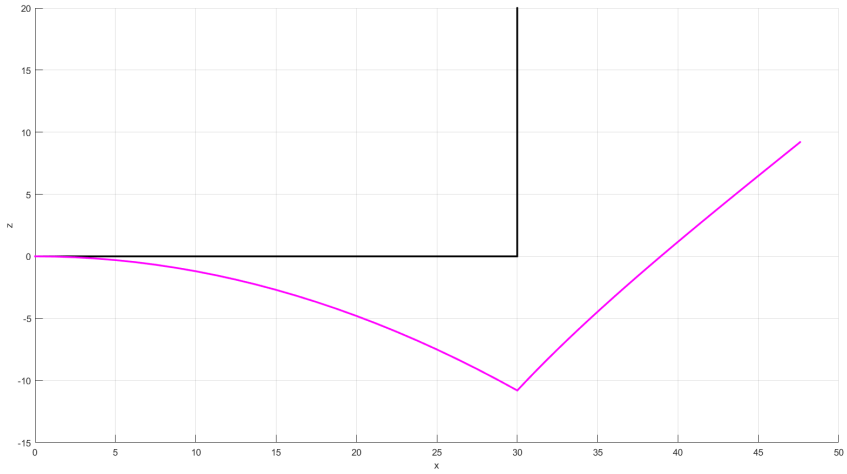

Figure 6.1: Cantilever L-beam — static deformed configuration under a nodal load $\mathbf{F} = \{10^{-4}, 0, 0\}$ N at node 3 (global $+X$). Black: undeformed centerline; magenta: deformed shape. Axes in metres. The same deformed shape applies to all sensor-layout cases A–D.

Sensor stations (cases A–D). Sensor abscissae are parameterized by the parent coordinate $\xi = x/L \in [0, 1]$ on each element. The four analyses in Sections 6.2.1–6.2.4 use: *Case A* (paired, baseline comparison with classical iFEM); *Case B* (paired at $\xi = 0.2$ and top at $\xi = 0.8$); *Case C* (top at $\xi = 0.2, 0.8$ and bottom at $\xi = 0.5$); *Case D* (top-only at $\xi = 0.2, 0.5, 0.8$). Unless otherwise noted, sensors lie on the mid-width line ($y = 0$), and their offsets (y_i, z_i) enter the prediction operator via $\mathbf{A}_i = \mathbf{B}_u(\xi_i) + z_i\,\mathbf{B}_w(\xi_i) + y_i\,\mathbf{B}_v(\xi_i)$ (cf. Chapter 3).

6.2.1 Case A — Classical iFEM vs SSB-iFEM (baseline)

1) Setup and instrumentation

The geometry, mesh, and boundary conditions are those detailed in Section 6.2. Two axial stations per element are instrumented at parent abscissae $\xi = \{0.2, 0.8\}$. All gauges lie on the mid-width line ($y = 0$) and are mounted in paired configuration on the top/bottom faces ($z = \pm h/2$), as sketched in Fig. 6.2. The resulting surface-strain measurements used by the SSB-iFEM are reported in Table 6.1.

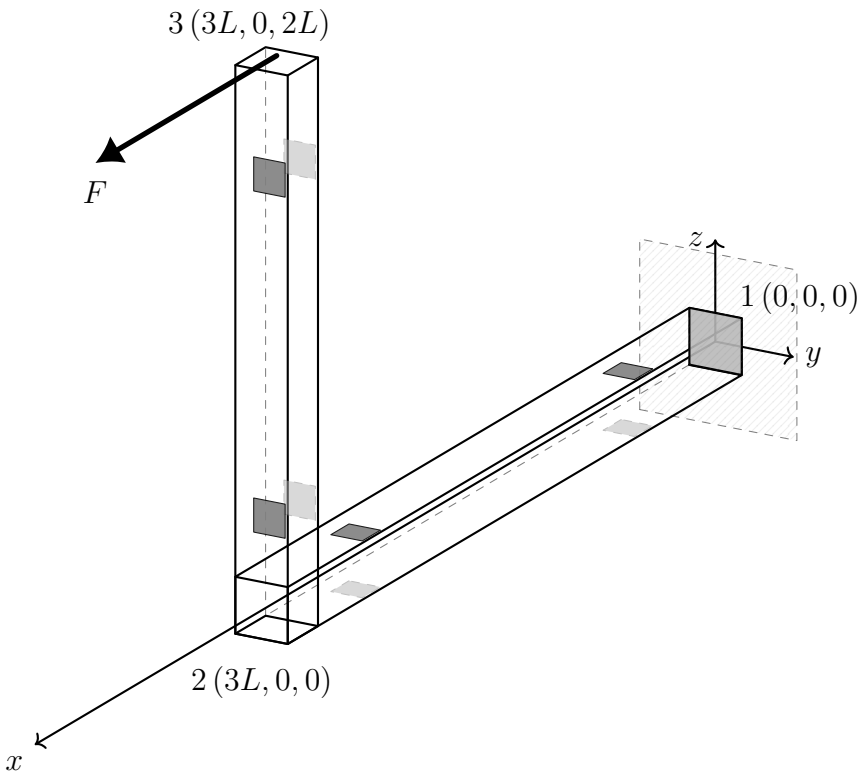

Figure 6.2: Cantilever L-beam: geometry, global axes, clamp at node 1, and paired sensors at $\xi = \{0.2, 0.8\}$ on the top/bottom faces. Cross-section $b = h = 1$. The symbolic load F is used only to illustrate the static deformed configuration elsewhere.

Measured channels (SSB input). The *SSB-iFEM* uses the surface axial strains ε_s recorded at the sensor offsets; the complete dataset across elements and stations is summarized in Table 6.1.

Table 6.1: Case A — Measured surface axial strains ε_s (dimensionless) at sensor stations for both elements. Sensors lie on the mid-width line ($y = 0$) at $z = \pm h/2$ (top/bottom).

Element	ξ	$\varepsilon_s^{\text{top}}$	$\varepsilon_s^{\text{bot}}$
1	0.2	0.0121	−0.0119
1	0.8	0.0121	−0.0119
2	0.2	0.0096	−0.0096
2	0.8	0.0024	−0.0024

Classical channels (derived from paired faces). The *classical* EB iFEM uses mid-line strain and curvature channels constructed from the

paired faces at the same section. With $h = 1$,

$$\varepsilon = \tfrac{1}{2}\left(\varepsilon_s^{\text{top}} + \varepsilon_s^{\text{bot}}\right), \qquad \kappa_{zz} = \varepsilon_s^{\text{top}} - \varepsilon_s^{\text{bot}}, \qquad (\kappa_{yy} = 0 \text{ since } y_i = 0).$$

Applying these relations to Table 6.1 yields the classical channels collected in Table 6.2.

Table 6.2: Case A — Classical iFEM channels at sensor stations. Mid-line axial strain ε (dimensionless) and bending curvature κ_{zz} [m^{-1}].

Element	ξ	ε	κ_{zz}
1	0.2	1.0000e−4	2.4000e−2
1	0.8	1.0000e−4	2.4000e−2
2	0.2	0.0000	1.9200e−2
2	0.8	0.0000	4.8000e−3

2) Reference

The independent forward FEM solver (provided by the advisor) supplies the global nodal displacement vector used as reference solution. For the in-plane DOFs at nodes 2–3 (ordered as $(u_2, w_2, \phi_{y2}, u_3, w_3, \phi_{y3})$) we obtain

$$\mathbf{q}^{\text{ref}} = \begin{bmatrix} 3.0000\text{e}{-3} & -1.0800\text{e}1 & -7.2000\text{e}{-1} & 1.7600\text{e}1 & -1.0800\text{e}1 & -9.6000\text{e}{-1} \end{bmatrix}^{\top},$$

which are the reference values also reported in Table 6.3 for direct comparison against the reconstructions.

3) Reconstruction results

Using the SSB inputs of Table 6.1 and the classical channels of Table 6.2, both inverse schemes deliver virtually identical reconstructions at the free nodes. Unless otherwise noted, all metrics are computed on the vector of nodal discrepancies with respect to the reference solution, restricted to the known in-plane DOFs at nodes 2–3, ordered as $(u_2, w_2, \phi_{y2}, u_3, w_3, \phi_{y3})$.

Table 6.3: Case A — Nodal quantities at free nodes (values). u, w in m; ϕ_y in rad. The three columns (True, SSB, CLS) enable a direct side-by-side comparison with the reference solution.

Node	DOF	Unit	Reference	SSB	CLS
2	u	m	3.0000e−3	3.0000e−3	3.0000e−3
2	w	m	−1.0800e1	−1.0800e1	−1.0800e1
2	ϕ_y	rad	−7.2000e−1	−7.2000e−1	−7.2000e−1
3	u	m	1.7603e1	1.7603e1	1.7603e1
3	w	m	−1.0800e1	−1.0800e1	−1.0800e1
3	ϕ_y	rad	−9.6000e−1	−9.6000e−1	−9.6000e−1

All SSB and CLS entries coincide with the reference values within plotting precision, showing that both inverse schemes reproduce the nodal DOFs essentially exactly in this baseline, fully paired layout.

Table 6.4: Case A — Direct nodal differences (Δ = SSB − CLS) at free nodes. These entries quantify the method-to-method discrepancy per DOF.

Node	DOF	Δu [m]	Δw [m]	$\Delta\phi_y$ [rad]
2		−4.3370e−19	5.4180e−12	2.7530e−13
3		−5.5000e−12	5.4180e−12	2.7470e−13

All differences are at the level of numerical round-off ($\sim 10^{-12}$), confirming that SSB and CLS deliver practically indistinguishable nodal reconstructions.

Table 6.5: Case A — Global metrics w.r.t. reference solution (free nodes). Definitions for an error vector $e \in \mathbb{R}^n$: RMSE $= \sqrt{\frac{1}{n}\sum_{i=1}^{n} e_i^2}$, $\|e\|_\infty = \max_i |e_i|$. Here e stacks (SSB−ref) or (CLS−ref) on $(u_2, w_2, \phi_{y2}, u_3, w_3, \phi_{y3})$.

Metric	SSB	CLS
RMSE	9.7640e−13	2.8770e−12
$\|\cdot\|_\infty$	1.3840e−12	4.1280e−12

Both RMSE and $\|\cdot\|_\infty$ are of order 10^{-12}–10^{-13}, i.e. at machine precision. The slightly smaller SSB figures indicate a marginal advantage in this noiseless, fully paired configuration, but the differences are not practically significant.

Table 6.6: Case A — Aggregate SSB–CLS discrepancy at free nodes (global metrics). Definitions for the method-to-method difference vector $d \in \mathbb{R}^n$ (SSB−CLS): RMSE $= \sqrt{\frac{1}{n}\sum_{i=1}^{n} d_i^2}$, $\|d\|_\infty = \max_i |d_i|$, $\|d\|_1 = \sum_{i=1}^{n} |d_i|$.

Metric	SSB − CLS
RMSE	2.9850e−12
$\|\cdot\|_\infty$	5.5000e−12
$\|\cdot\|_1$	1.6890e−12

These aggregate figures condense the small per-DOF differences of Table 6.4 into vector norms. The values remain at round-off, reinforcing the baseline equivalence between SSB-iFEM and classical iFEM for the present, fully paired layout.

Element-wise field differences. Figures 6.3–6.4 plot the pointwise differences $\Delta u(s) = u_{\mathrm{SSB}}(s) - u_{\mathrm{CLS}}(s)$ and $\Delta w(s) = w_{\mathrm{SSB}}(s) - w_{\mathrm{CLS}}(s)$ along the local abscissa s of each element (markers at the instrumented stations). The curves remain at round-off across both elements, including at the measurement stations, showing that the two inverse schemes reconstruct essentially the same fields.

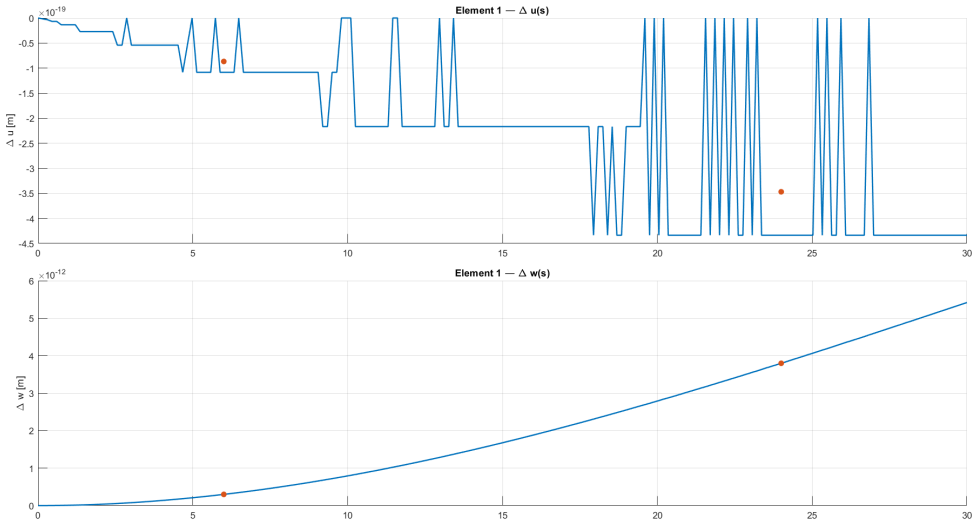

Figure 6.3: Case A (L-beam), Element 1. Pointwise differences $\Delta u(s)$ and $\Delta w(s)$ between SSB and classical iFEM. Markers: sensor stations at $\xi = \{0.2, 0.8\}$.

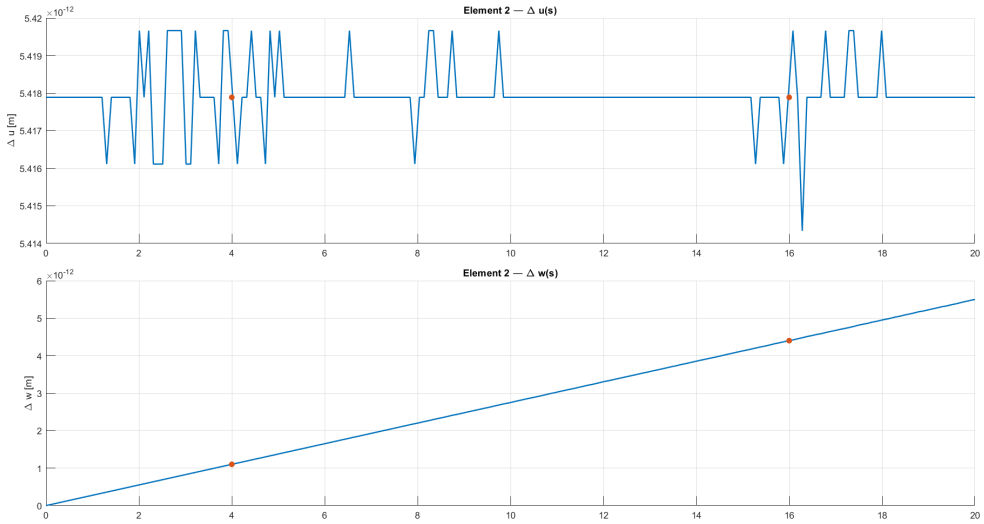

Figure 6.4: Case A (L-beam), Element 2. Pointwise differences $\Delta u(s)$ and $\Delta w(s)$ between SSB and classical iFEM. Markers: sensor stations at $\xi = \{0.2, 0.8\}$.

4) Discussion

- **Baseline equivalence.** With paired top/bottom sensors at both stations and $y_i = 0$, SSB-iFEM and classical EB iFEM achieve coincident reconstructions at machine precision (Tables 6.4–6.6; Figs. 6.3–6.4).
- **Implication for subsequent cases.** The results confirm that full pairing on accessible faces is sufficient for high-accuracy recovery of (u, w, ϕ_y) on the L-beam. Sections 6.2.2–6.2.4 progressively relax pairing and sidedness to assess robustness under practical accessibility constraints.

6.2.2 Case B — SSB-iFEM: paired sensors at $\xi = 0.2$ and top sensor at $\xi = 0.8$

1) Setup and instrumentation

The geometry, mesh, kinematics, boundary conditions, and sign convention are the same as in Section 6.2. Instrumentation differs from Case A as follows: for each element, two axial stations are used at parent abscissae $\xi = \{0.2, 0.8\}$; at $\xi = 0.2$ a *paired* top/bottom installation is available on the mid-width line ($y = 0$, faces $z = \pm h/2$), while at $\xi = 0.8$ only the *top* face ($z = +h/2$) is instrumented.

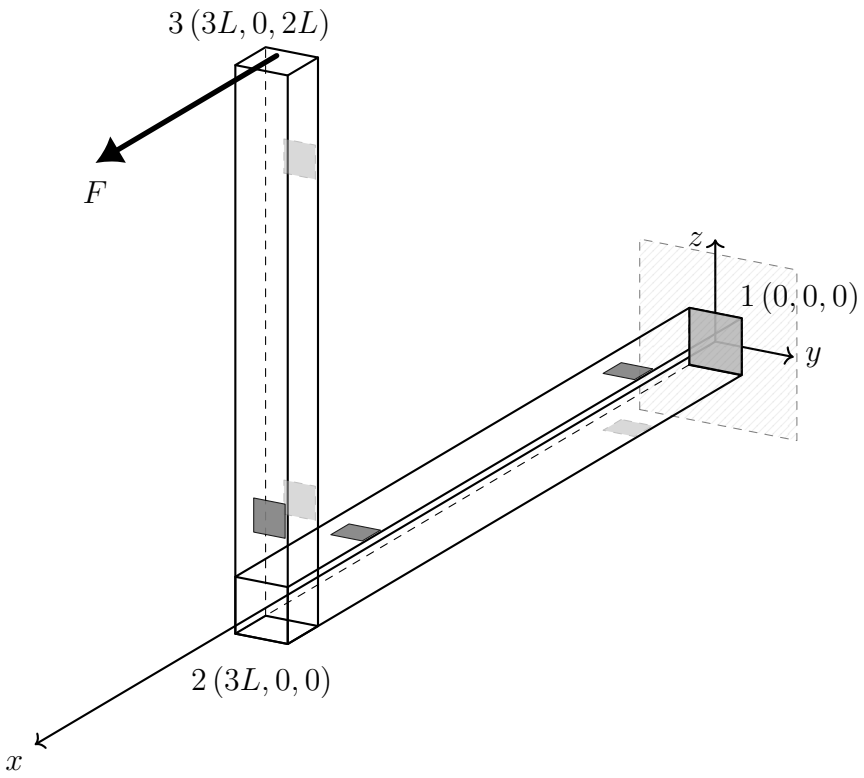

Figure 6.5: Case B (L-beam): sensor layout. Paired top/bottom at $\xi = 0.2$ on each element; top-only at $\xi = 0.8$. All sensors lie on the mid-width line ($y = 0$).

Measured channels (SSB input). Surface axial strains ε_s at the available offsets ($y_i = 0,\ z_i = \pm h/2$) are those already listed for Case A at the same stations; here, the bottom reading at $\xi = 0.8$ is *not* used. Table 6.7 collects the channels by element and station (a dash marks unavailable sensors).

Table 6.7: Case B — Measured surface strains ε_s (dimensionless) at sensor stations. Top/bottom refer to $z = \pm h/2$; "—" denotes an intentionally absent sensor (top-only at $\xi = 0.8$).

Element	ξ	$\varepsilon_s^{\text{top}}$	$\varepsilon_s^{\text{bot}}$
1	0.2	0.0121	−0.0119
1	0.8	0.0121	—
2	0.2	0.0096	−0.0096
2	0.8	0.0024	—

2) Reference (comparison target)

The reference nodal displacement vector $\mathbf{q}^{\text{ref}}$ is provided by the forward FEM tool used throughout Chapter 5 (Section 6.1). We compare the SSB-iFEM reconstruction against this reference on the known in-plane DOFs at nodes 2–3: $(u_2, w_2, \phi_{y2}, u_3, w_3, \phi_{y3})$.

3) Reconstruction results

With the reduced-but-informative layout of Table 6.7, the SSB-iFEM reproduces the reference solution at machine precision.

Table 6.8: Case B — Nodal quantities at free nodes (values). u, w in m; ϕ_y in rad.

Node	DOF	Unit	Reference	SSB
2	u	m	3.0000e−3	3.0000e−3
2	w	m	−1.0800e1	−1.0800e1
2	ϕ_y	rad	−7.2000e−1	−7.2000e−1
3	u	m	1.7600e1	1.7600e1
3	w	m	−1.0800e1	−1.0800e1
3	ϕ_y	rad	−9.6000e−1	−9.6000e−1

Global relative metrics (free nodes, known DOFs) confirm the negligible discrepancy:

$$\frac{\|\text{err}\|_\infty}{\|\text{ref}\|_\infty} = 1.433 \times 10^{-14}, \qquad \frac{\|\text{err}\|_2}{\|\text{ref}\|_2} = 1.358 \times 10^{-14}.$$

For completeness, per–element relative figures are 1.250×10^{-14} and 1.252×10^{-14} on Element 1, and 1.433×10^{-14} and 1.358×10^{-14} on Element 2.

Sensor diagnostics. For each element, the left bar–plot reports the residuals of the surface–strain channels,

$$r_i \;=\; \varepsilon_{s,i}^{\text{pred}} \;-\; \varepsilon_{s,i}^{\text{meas}},$$

with one bar per sensor station in the order used by the input arrays. The predicted strain at station ξ_i (with local offsets y_i, z_i) is obtained from the reconstructed local DOFs $\mathbf{q}_{\text{loc}}$ via

$$\varepsilon_{s,i}^{\text{pred}} \;=\; \Big(\mathbf{B}_u(\xi_i) \;+\; z_i\, \mathbf{B}_w(\xi_i) \;+\; y_i\, \mathbf{B}_v(\xi_i) \Big)\, \mathbf{q}_{\text{loc}}.$$

The right scatter–plot compares measured vs. predicted strains (one marker per sensor) and includes the 1:1 reference line; points lying on the 1:1 indicate perfect agreement, whereas systematic offsets (parallel clouds) and slope deviations reveal bias or scaling effects.

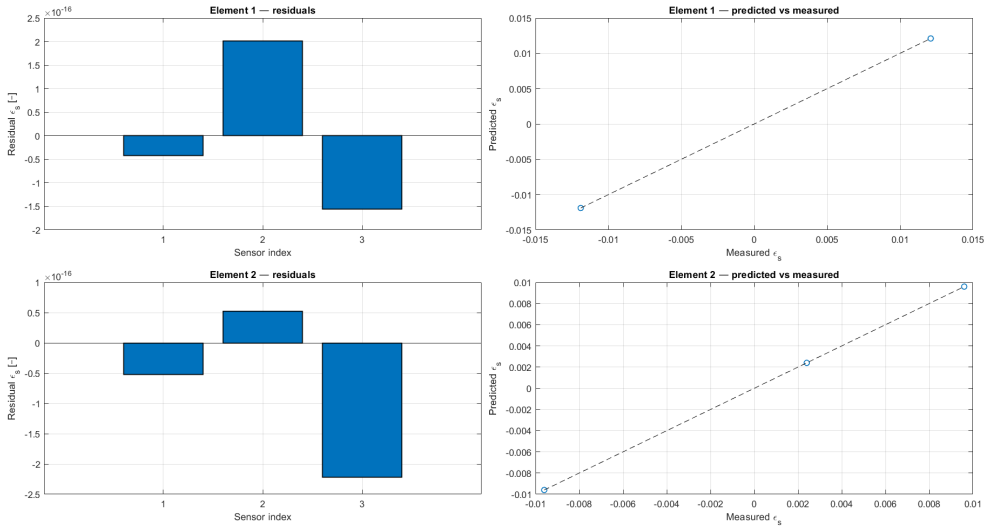

Figure 6.6: Case B (L-beam). Left: sensor residuals by element. Right: predicted vs measured ε_s with 1:1 guideline.

4) Discussion

- **Accuracy with reduced channels.** Despite the missing bottom reading at $\xi = 0.8$ on each element, the paired station at $\xi = 0.2$ plus a single top channel at $\xi = 0.8$ is sufficient to reproduce (u, w, ϕ_y) at machine precision on this L-beam.

- **Diagnostics.** The residual and 1:1 plots (Fig. 6.6) show negligible bias and dispersion, corroborating the bar-chart and metric-based assessments.

- **Implication.** Case B confirms that SSB-iFEM remains robust under mild accessibility constraints (paired+single-sided layout), anticipating the more restrictive layouts explored in Cases C–D.

6.2.3 Case C — SSB-iFEM: top sensors at $\xi = 0.2$, $\xi = 0.8$; bottom sensor at $\xi = 0.5$

1) Setup and instrumentation

The geometry, mesh, and boundary conditions are those of Section 6.2. Each element is instrumented with three surface–strain gauges along the mid-width line ($y = 0$): *top* face at $\xi = 0.2$, *bottom* face at $\xi = 0.5$, and *top* face at $\xi = 0.8$ (i.e., $z = \{+h/2, -h/2, +h/2\}$).

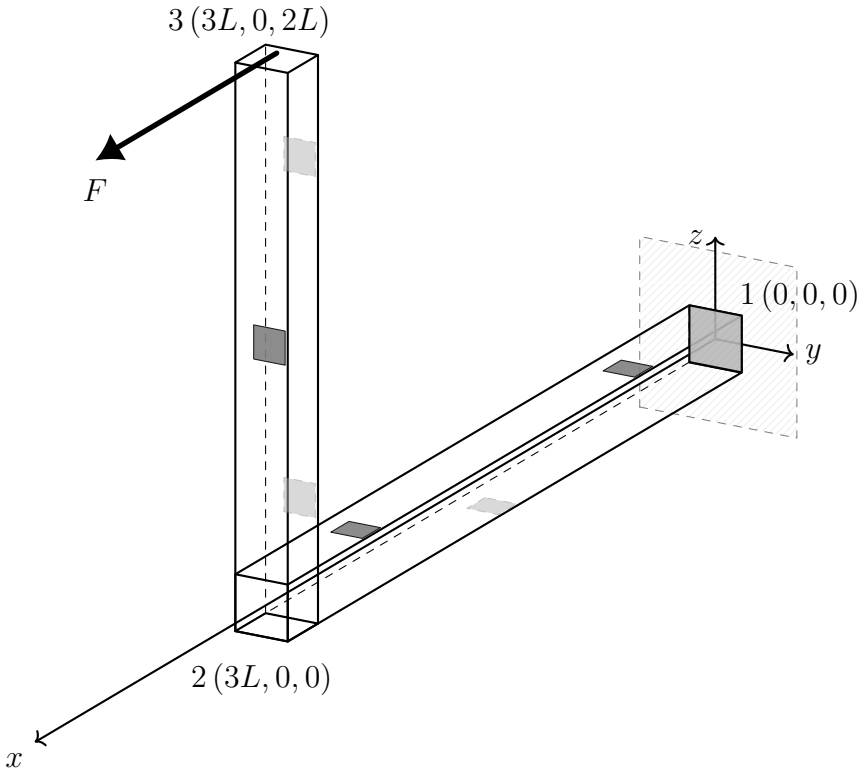

Figure 6.7: Case C (L-beam): sensor layout. Top sensors at $\xi = 0.2$ and $\xi = 0.8$; bottom sensor at $\xi = 0.5$. All sensors lie on the mid-width line ($y = 0$).

Measured channels. *SSB-iFEM input* consists of the surface axial strains ε_s at the sensor offsets. Table 6.9 lists the measured values (rounded) at the three stations of each element.

Table 6.9: Case C — Measured surface axial strains ε_s (dimensionless) at sensor stations for both elements. Sensors lie on the mid-width line ($y = 0$) at $z = \pm h/2$ (top/bottom).

Element	ξ	Face	ε_s
1	0.2	top	0.0121
1	0.5	bottom	−0.0119
1	0.8	top	0.0121
2	0.2	top	0.0096
2	0.5	bottom	−0.0060
2	0.8	top	0.0024

2) Reference (comparison target)

The reference nodal displacement vector $\mathbf{q}^{\text{ref}}$ is provided by the forward FEM tool used throughout Chapter 5 (Section 6.1). We compare the SSB-iFEM reconstruction against this reference on the known in-plane DOFs at nodes 2–3: $(u_2, w_2, \phi_{y2}, u_3, w_3, \phi_{y3})$.

3) Reconstruction results

Using the SSB inputs of Table 6.9, the inverse analysis matches the reference at machine precision.

Table 6.10: Case C — Nodal quantities at free nodes (values). u, w in m; ϕ_y in rad.

Node	DOF	Unit	Reference	SSB
2	u	m	3.0000e−3	3.0000e−3
2	w	m	−1.0800e1	−1.0800e1
2	ϕ_y	rad	−7.2000e−1	−7.2000e−1
3	u	m	1.7600e1	1.7600e1
3	w	m	−1.0800e1	−1.0800e1
3	ϕ_y	rad	−9.6000e−1	−9.6000e−1

Relative error metrics. Global relative errors (excluding constrained DOFs) and per–element summaries are reported in Tables 6.11–6.12. Here $\|\cdot\|_\infty$ is the max norm over the stacked vector of nodal DOFs, and $\|\cdot\|_2$ the Euclidean norm; we quote the ratio $\|\text{err}\|/\|\text{ref}\|$ as provided by the post-processor.

Table 6.11: Case C — Global relative error metrics (free nodes).

Metric	Value
$\|\text{err}\|_\infty / \|\text{ref}\|_\infty$	7.5680e−15
$\|\text{err}\|_2 / \|\text{ref}\|_2$	9.4700e−15

Table 6.12: Case C — Per–element relative errors.

Element	$\|\text{err}\|_\infty / \|\text{ref}\|_\infty$	$\|\text{err}\|_2 / \|\text{ref}\|_2$
1	1.2340e−14	1.2320e−14
2	7.5680e−15	9.4700e−15

Sensor diagnostics. For each element, the left bar–plot reports the residuals of the surface–strain channels,

$$r_i \;=\; \varepsilon_{s,i}^{\text{pred}} \;-\; \varepsilon_{s,i}^{\text{meas}},$$

with one bar per sensor station in the order used by the input arrays. The predicted strain at station ξ_i (with local offsets y_i, z_i) is obtained from the reconstructed local DOFs $\mathbf{q}_{\text{loc}}$ via

$$\varepsilon_{s,i}^{\text{pred}} \;=\; \Big(\mathbf{B}_u(\xi_i) \;+\; z_i\, \mathbf{B}_w(\xi_i) \;+\; y_i\, \mathbf{B}_v(\xi_i) \Big)\, \mathbf{q}_{\text{loc}}.$$

The right scatter–plot compares measured vs. predicted strains (one marker per sensor) and includes the 1:1 reference line; points lying on the 1:1 indicate perfect agreement, whereas systematic offsets (parallel clouds) and slope deviations reveal bias or scaling effects.

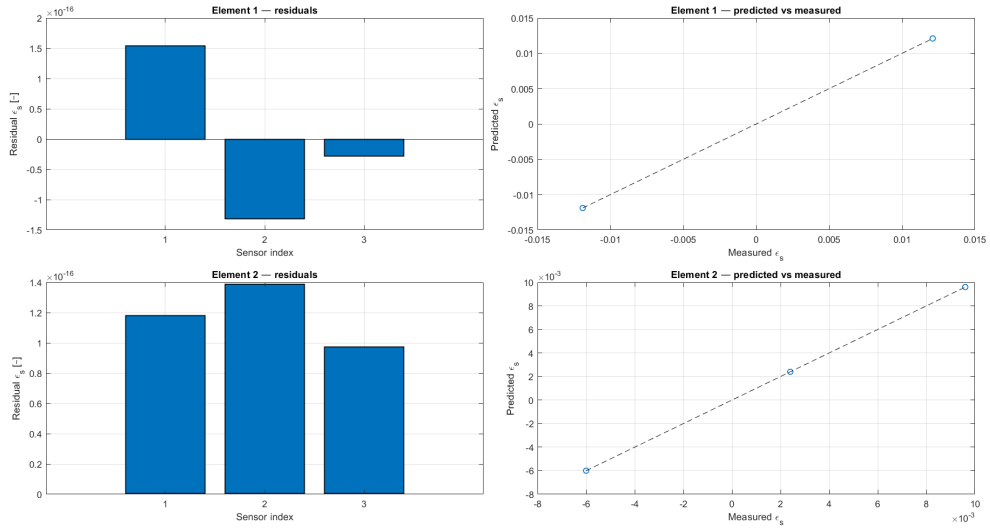

Figure 6.8: Case C (L-beam). Left: residuals per sensor (Element 1 on top, Element 2 bottom). Right: predicted vs. measured ε_s with 1:1 guideline.

4) Discussion

- **Accuracy with mixed sidedness.** A three-sensor layout per element (top–bottom–top) still achieves machine-precision agreement on the known DOFs. The bottom station at $\xi = 0.5$ restores local pairing for bending about y, maintaining excellent observability of (u, w, ϕ_y).
- **Practical note.** Even without full pairing at both stations, distributing the three sensors as in Case C provides a robust constraint set for SSB on the L-beam.

6.2.4 Case D — SSB-iFEM: top-only sensors at $\xi = \{0.2, 0.5, 0.8\}$

1) Setup and instrumentation

Geometry, mesh, kinematics, and boundary conditions are those of Section 6.2. Each element is instrumented with *three top-face* surface–strain sensors at parent abscissae $\xi = \{0.2, 0.5, 0.8\}$; all stations lie on the mid-width line ($y = 0$) and at $z = +h/2$ (top).

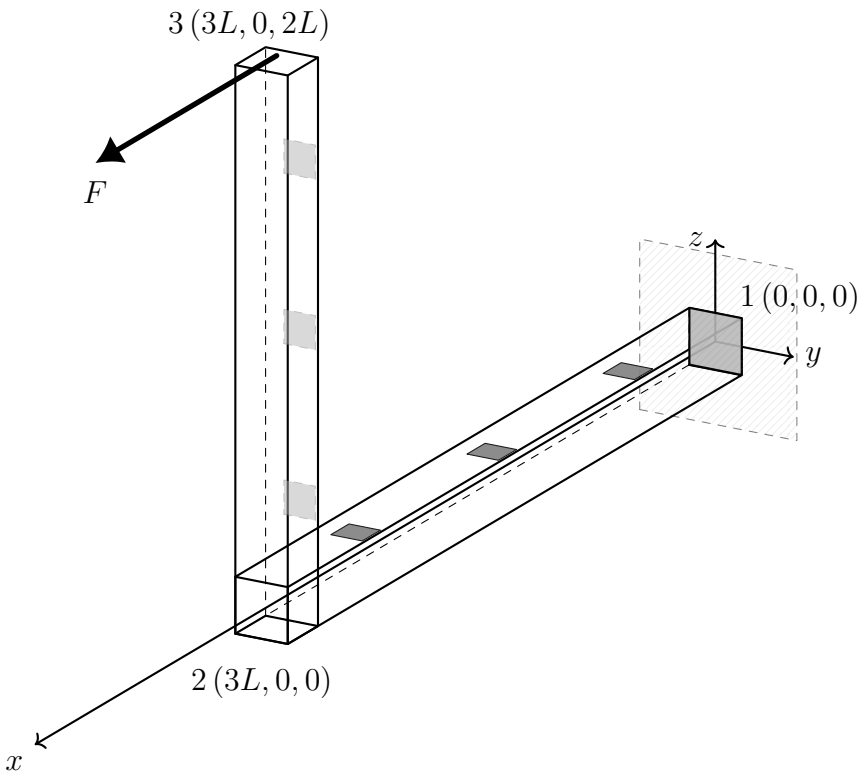

Figure 6.9: Case D (L-beam): sensor layout. Top-only sensors at $\xi = \{0.2, 0.5, 0.8\}$ on each element; all sensors on the mid-width line ($y = 0$).

Measured channels. The SSB-iFEM input consists of the surface axial strains ε_s at the sensor offsets (top face, $z = +h/2$). The measured values are:

Table 6.13: Case D — Measured surface axial strains ε_s (dimensionless) at the three top-face stations on each element.

Element	ξ	0.2	0.5	0.8
1	$\varepsilon_s^{\text{top}}$	0.0121	0.0121	0.0121
2	$\varepsilon_s^{\text{top}}$	0.0096	0.0060	0.0024

2) Reference (comparison target)

As in the previous cases, the forward FEM solver provides the *reference* nodal DOFs at the free nodes $(u_2, w_2, \phi_{y2}, u_3, w_3, \phi_{y3})$ used for all comparisons (see Section 6.2).

3) Reconstruction results

With top-only instrumentation ($y_i = 0$ and $z_i = +h/2$ at all stations), the SSB system lacks the paired top/bottom information needed to disentangle mid-line strain ε from bending curvature κ_{zz}. Consequently, the inverse fit becomes ill-conditioned and the reconstructed nodal quantities deviate markedly from the reference solution.

Nodal values and relative errors. Table 6.14 reports SSB vs. reference at free nodes, together with the relative error (in %). Large errors at both nodes confirm the inadequacy of top-only layouts for this configuration.

Table 6.14: Case D — Nodal quantities at free nodes (values and relative errors). u, w in m; ϕ_y in rad.

Node	DOF	Unit	SSB	Reference	Rel. err [%]
2	u	m	3.5410e−1	3.0000e−3	11 703.6550
2	w	m	−2.6670e−1	−1.0800e1	97.5300
2	ϕ_y	rad	1.7780e−2	7.2000e−1	97.5300
3	u	m	4.0710e−2	1.7600e1	99.7690
3	w	m	−7.3260e−2	−1.0800e1	99.3220
3	ϕ_y	rad	−1.2910e−1	9.6000e−1	113.4500

Aggregate relative metrics. Global relative errors (excluding constrained DOFs) and per–element figures are summarised in Table 6.15. Here $\|\cdot\|_\infty$ is the infinity norm (max absolute component) and $\|\cdot\|_2$ is the Euclidean norm.

Table 6.15: Case D — Global relative errors w.r.t. the reference solution.

Quantity	$\|\text{err}\|_\infty/\|\text{ref}\|_\infty$	$\|\text{err}\|_2/\|\text{ref}\|_2$
Whole structure	9.9770	9.9230
Element 1	9.7530	9.7580
Element 2	9.9770	9.9230

4) Discussion

- **Observability shortfall.** With top-only sensors ($z = +h/2$ at all stations), the SSB prediction operator cannot separate the mid-line strain

ε from the curvature κ_{zz}; the problem is effectively under–determined and ill-conditioned.

- **Impact on accuracy.** The loss of pairing drives large biases at the free nodes (Table 6.14) and near-unit global relative errors (Table 6.15).
- **Design implication.** For EB beams, at least one paired top/bottom station per element (or equivalent multi-face information) is necessary to achieve accurate reconstructions of (u, w, ϕ_y); single-sided, unpaired layouts should be avoided unless supplemented by additional information or regularisation.

6.3 Structure 2: Cantilever Z-Beam

Geometry and mesh. The Z-beam is modeled as a three–element Euler–Bernoulli (EB) assembly lying in the global X–Z plane. The nodal coordinates (in metres) are

$$\mathbf{x}_1 = (0, 0, 0), \qquad \mathbf{x}_2 = (3L, 0, 0), \qquad \mathbf{x}_3 = (3L, 0, 4L), \qquad \mathbf{x}_4 = (7L, 0, 4L),$$
$$L = 10$$

Element connectivity is $\mathcal{C}_e = \{(1, 2), (2, 3), (3, 4)\}$. Each element adopts a local frame with x_{loc} aligned with the element axis, $y_{\text{loc}} \parallel Y$, and $z_{\text{loc}} = x_{\text{loc}} \times y_{\text{loc}}$, so that $\mathbf{\Lambda}_e$ consistently maps local EB DOFs to the global frame.

Cross-section. A constant rectangular cross-section is assumed with width $b = 1$ (along y) and height $h = 1$ (along z). Only geometric data enter the inverse formulation; material properties are not required by iFEM.

Kinematics and sign conventions. All operators follow the EB kinematics and the sign convention of Chapter 2: $\phi_y = -w_{,x}$, $\omega_z = v_{,x}$, $\kappa_{zz} = -w_{,xx}$, $\kappa_{yy} = -v_{,xx}$. Element operators are evaluated in local frames and rotated to the global frame by $\mathbf{\Lambda}_e$ prior to assembly.

Boundary conditions. A clamp is imposed at node 1 (all five EB DOFs fixed). To restrict the analysis to in-plane response (X–Z), the out-of-plane DOFs are suppressed at the free nodes by enforcing $v = \omega_z = 0$ at nodes 2, 3 and 4. Corner compatibilities at nodes 2 and 3 are enforced automatically by the common nodal DOFs.

Static deformed configuration (visualization). Under a nodal load at node 4 along global $+X$, $\mathbf{F} = \{10^{-4}, 0, 0\}$ N, the static deformed configuration is plotted (Figure 6.10). This visualization is independent of the inverse formulation and is common to all cases A–D.

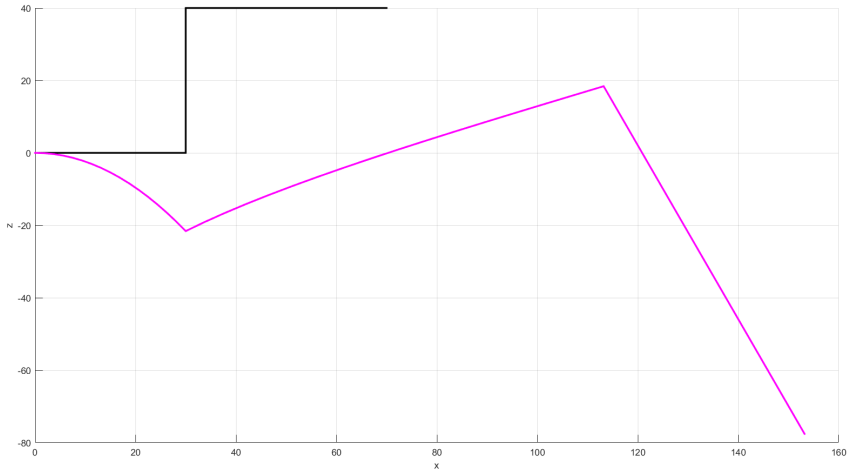

Figure 6.10: Cantilever Z-beam — static deformed configuration under a nodal load $\mathbf{F} = \{10^{-4}, 0, 0\}$ N at node 4 (global $+X$). Black: undeformed centerline; magenta: deformed shape. Axes in metres. The same deformed shape applies to all sensor-layout cases A–D.

Sensor stations (cases A–D). Sensor abscissae are parameterized by the parent coordinate $\xi = x/L \in [0, 1]$ on each element. The four analyses in Sections 6.3.1–6.3.4 use: *Case A* (paired, baseline comparison with classical iFEM); *Case B* (paired at $\xi = 0.2$ and top at $\xi = 0.8$); *Case C* (top at $\xi = 0.2, 0.8$ and bottom at $\xi = 0.5$); *Case D* (top-only at $\xi = 0.2, 0.5, 0.8$). Unless otherwise noted, sensors lie on the mid-width line ($y = 0$), and their offsets (y_i, z_i) enter the prediction operator via $\mathbf{A}_i = \mathbf{B}_u(\xi_i) + z_i\,\mathbf{B}_w(\xi_i) + y_i\,\mathbf{B}_v(\xi_i)$ (cf. Chapter 3).

6.3.1 Case A — Classical iFEM vs SSB-iFEM (baseline)

1) Setup and instrumentation

The geometry, mesh, and boundary conditions are those detailed in Section 6.3. Two axial stations per element are instrumented at parent abscissae $\xi = \{0.2, 0.8\}$. All gauges lie on the mid-width line ($y = 0$) and are mounted in paired configuration on the top/bottom faces ($z = \pm h/2$), as sketched in Fig. 6.11. The resulting surface-strain measurements used by the SSB-iFEM are reported in Table 6.16.

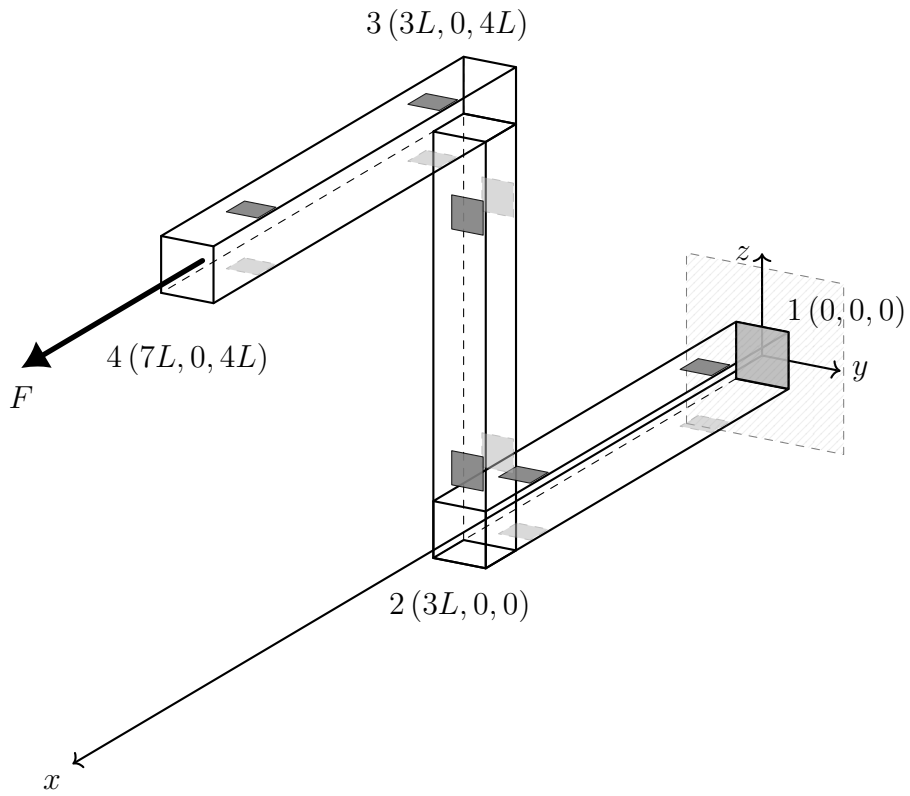

Figure 6.11: Cantilever Z-beam: geometry, global axes, clamp at node 1, and paired sensors at $\xi = \{0.2, 0.8\}$ on the top/bottom faces of all three elements. Cross-section $b = h = 1$. The symbolic load F is used only to illustrate the static deformed configuration elsewhere.

Measured channels (SSB input). The *SSB-iFEM* uses the surface axial strains ε_s recorded at the sensor offsets; the complete dataset across elements and stations is summarized in Table 6.16.

Table 6.16: Case A — Measured surface axial strains ε_s (dimensionless) at sensor stations for all three elements. Sensors lie on the mid-width line ($y = 0$) at $z = \pm h/2$ (top/bottom).

Element	ξ	$\varepsilon_s^{\text{top}}$	$\varepsilon_s^{\text{bot}}$
1	0.2	0.0241	−0.0239
1	0.8	0.0241	−0.0239
2	0.2	0.0192	−0.0192
2	0.8	0.0048	−0.0048
3	0.2	0.0001	0.0001
3	0.8	0.0001	0.0001

Classical channels (derived from paired faces). The *classical* EB iFEM uses mid-line strain and curvature channels constructed from the paired faces at the same section. With $h = 1$,

$$\varepsilon = \tfrac{1}{2}\left(\varepsilon_s^{\text{top}} + \varepsilon_s^{\text{bot}}\right), \qquad \kappa_{zz} = \varepsilon_s^{\text{top}} - \varepsilon_s^{\text{bot}}, \qquad (\kappa_{yy} = 0 \text{ since } y_i = 0).$$

Applying these relations to Table 6.16 yields the classical channels collected in Table 6.17.

Table 6.17: Case A — Classical iFEM channels at sensor stations. Mid-line axial strain ε (dimensionless) and bending curvature κ_{zz} [m^{-1}].

Element	ξ	ε	κ_{zz}
1	0.2	1.0000e−4	4.8000e−2
1	0.8	1.0000e−4	4.8000e−2
2	0.2	0.0000	3.8400e−2
2	0.8	0.0000	9.6000e−3
3	0.2	1.0000e−4	0.0000
3	0.8	1.0000e−4	0.0000

2) Reference

The independent forward FEM solver (provided by the advisor) supplies the global nodal displacement vector used as reference solution. For the in-plane DOFs at nodes 2–4 (ordered as $(u_2, w_2, \phi_{y2}; u_3, w_3, \phi_{y3}; u_4, w_4, \phi_{y4})$) we obtain

$$\mathbf{q}^{\text{ref}} = \begin{bmatrix} 3.0000\text{e}{-3} & -2.1600\text{e}1 & -1.4400 \\ 8.3203\text{e}1 & -2.1600\text{e}1 & -2.4000 \\ 8.3207\text{e}1 & -1.1760\text{e}2 & -2.4000 \end{bmatrix}^{\top},$$

which are the reference values also reported in Table 6.18 for direct comparison against the reconstructions.

3) Reconstruction results

Using the SSB inputs of Table 6.16 and the classical channels of Table 6.17, both inverse schemes deliver virtually identical reconstructions at the free nodes. Unless otherwise noted, all metrics are computed on the vector of nodal discrepancies with respect to the reference solution, restricted to the known in-plane DOFs at nodes 2–4, ordered as $(u_2, w_2, \phi_{y2}, u_3, w_3, \phi_{y3}, u_4, w_4, \phi_{y4})$.

Table 6.18: Case A — Nodal quantities at free nodes (values). u, w in m; ϕ_y in rad. The three columns (Reference, SSB, CLS) enable a direct side-by-side comparison with the reference solution.

Node	DOF	Unit	Reference	SSB	CLS
2	u	m	3.0000e−3	3.0000e−3	3.0000e−3
2	w	m	−2.1600e1	−2.1600e1	−2.1600e1
2	ϕ_y	rad	−1.4400	−1.4400	−1.4400
3	u	m	8.3203e1	8.3203e1	8.3203e1
3	w	m	−2.1600e1	−2.1600e1	−2.1600e1
3	ϕ_y	rad	−2.4000	−2.4000	−2.4000
4	u	m	8.3207e1	8.3207e1	8.3207e1
4	w	m	−1.1760e2	−1.1760e2	−1.1760e2
4	ϕ_y	rad	−2.4000	−2.4000	−2.4000

All SSB and CLS entries coincide with the reference values within plotting precision, showing that both inverse schemes reproduce the nodal DOFs essentially exactly in this baseline, fully paired layout.

Table 6.19: Case A — Direct nodal differences (Δ = SSB − CLS) at free nodes. These entries quantify the method-to-method discrepancy per DOF.

Node	DOF	Δu [m]	Δw [m]	$\Delta\phi_y$ [rad]
2		1.8680e−15	1.9640e−11	1.3040e−12
3		−7.4520e−11	1.9640e−11	2.1560e−12
4		−7.4490e−11	1.0580e−10	2.1550e−12

All differences are at the level of numerical round-off ($\sim 10^{-10}$ or smaller compared to the absolute DOF magnitudes), confirming that SSB and CLS deliver practically indistinguishable nodal reconstructions.

Table 6.20: Case A — Global metrics w.r.t. reference solution (free nodes). Definitions for an error vector $e \in \mathbb{R}^n$: RMSE $= \sqrt{\frac{1}{n}\sum_{i=1}^{n} e_i^2}$, $\|e\|_\infty = \max_i |e_i|$. Here e stacks (SSB−ref) or (CLS−ref) on $(u_2, w_2, \phi_{y2}, u_3, w_3, \phi_{y3}, u_4, w_4, \phi_{y4})$.

Metric	SSB	CLS
RMSE	4.4970e−11	9.5620e−11
$\|\cdot\|_\infty$	9.4100e−11	1.9990e−10

Both RMSE and $\|\cdot\|_\infty$ are of order 10^{-11}–10^{-10}, i.e. negligible when compared with the absolute DOF magnitudes (tens of metres and radians). The slightly smaller SSB figures indicate a marginal advantage in this noiseless, fully paired configuration, but the differences are not practically significant.

Table 6.21: Case A — Aggregate SSB–CLS discrepancy at free nodes (global metrics). Definitions for the method-to-method difference vector $d \in \mathbb{R}^n$ (SSB−CLS): RMSE $= \sqrt{\frac{1}{n}\sum_{i=1}^{n} d_i^2}$, $\|d\|_\infty = \max_i |d_i|$, $\|d\|_1 = \sum_{i=1}^{n} |d_i|$.

Metric	SSB − CLS
RMSE	3.9230e−11
$\|\cdot\|_\infty$	1.0580e−10
$\|\cdot\|_1$	1.9980e−11

These aggregate figures condense the small per-DOF differences of Table 6.19 into vector norms. The values remain very small, reinforcing the baseline equivalence between SSB-iFEM and classical iFEM for the present, fully paired layout.

Element-wise field differences. Figures 6.12–6.14 plot the pointwise differences $\Delta u(s) = u_{\mathrm{SSB}}(s) - u_{\mathrm{CLS}}(s)$ and $\Delta w(s) = w_{\mathrm{SSB}}(s) - w_{\mathrm{CLS}}(s)$ along the local abscissa s of each element (markers at the instrumented stations). The curves remain at round-off across all three elements, including at the measurement stations, showing that the two inverse schemes reconstruct essentially the same fields.

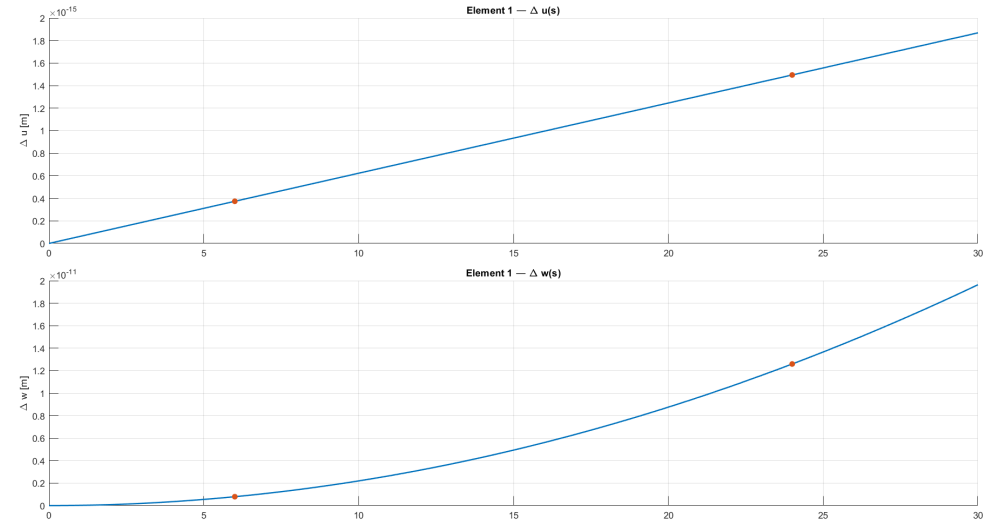

Figure 6.12: Case A (Z-beam), Element 1. Pointwise differences $\Delta u(s)$ and $\Delta w(s)$ between SSB and classical iFEM. Markers: sensor stations at $\xi = \{0.2, 0.8\}$.

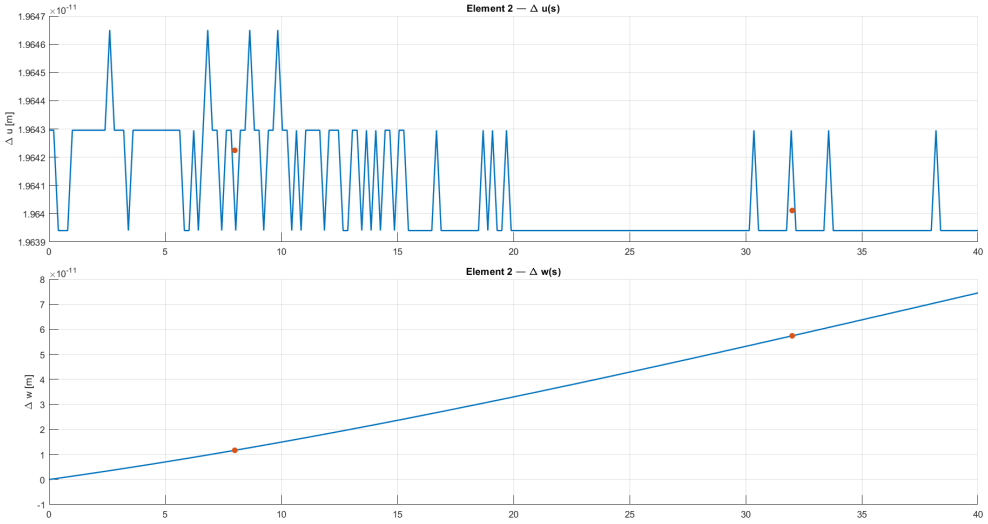

Figure 6.13: Case A (Z-beam), Element 2. Pointwise differences $\Delta u(s)$ and $\Delta w(s)$ between SSB and classical iFEM. Markers: sensor stations at $\xi = \{0.2, 0.8\}$.

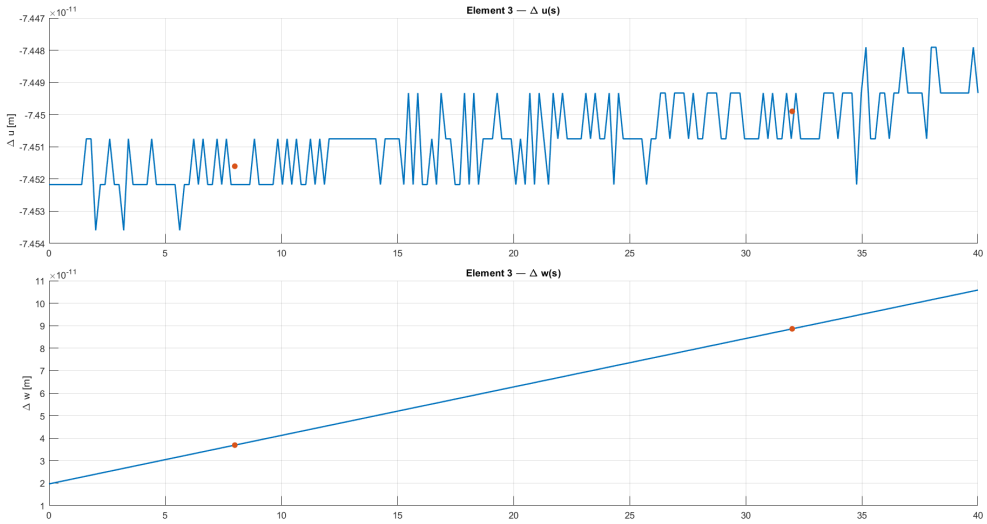

Figure 6.14: Case A (Z-beam), Element 3. Pointwise differences $\Delta u(s)$ and $\Delta w(s)$ between SSB and classical iFEM. Markers: sensor stations at $\xi = \{0.2, 0.8\}$.

4) Discussion

- **Baseline equivalence.** With paired top/bottom sensors at both stations and $y_i = 0$, SSB-iFEM and classical EB iFEM achieve coincident reconstructions up to numerical round-off (Tables 6.19–6.21; Figs. 6.12–6.14).
- **Implication for subsequent cases.** The results confirm that full pairing on accessible faces is sufficient for high-accuracy recovery of (u, w, ϕ_y) on the Z-beam. Sections 6.3.2–6.3.4 progressively relax pairing and sidedness to assess robustness under practical accessibility constraints.

6.3.2 Case B — SSB-iFEM: paired sensors at $\xi = 0.2$ and top sensor at $\xi = 0.8$

1) Setup and instrumentation

The geometry, mesh, kinematics, boundary conditions, and sign convention are the same as in Section 6.3. Instrumentation differs from Case A as follows: for each element, two axial stations are used at parent abscissae $\xi = \{0.2, 0.8\}$; at $\xi = 0.2$ a *paired* top/bottom installation is available on the mid-width line ($y = 0$, faces $z = \pm h/2$), while at $\xi = 0.8$ only the *top* face ($z = +h/2$) is instrumented.

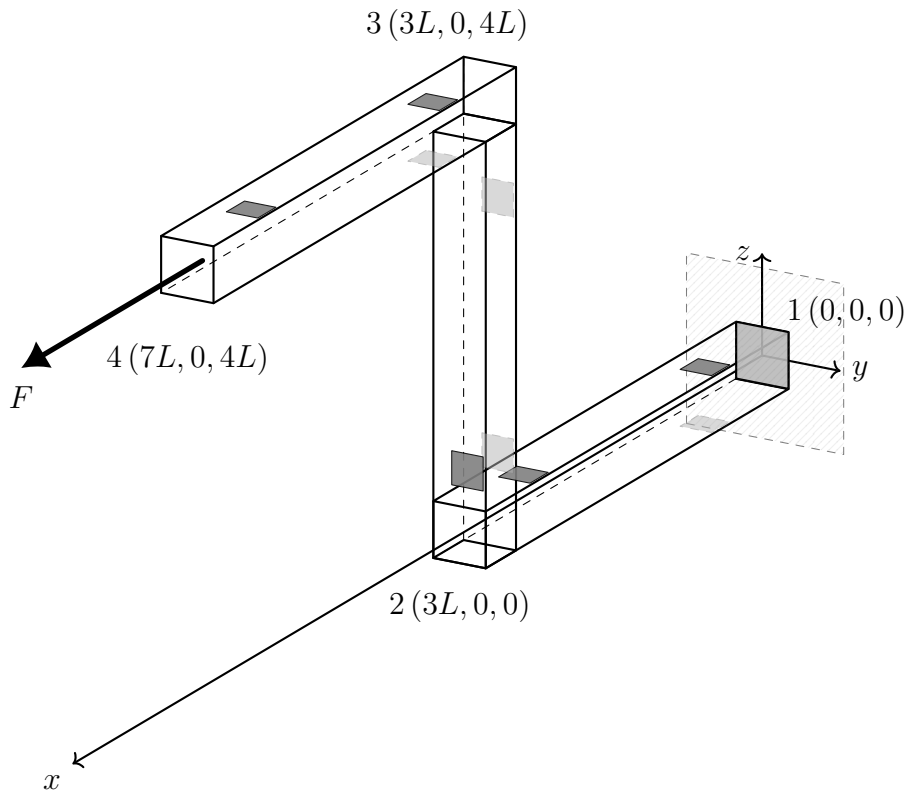

Figure 6.15: Case B (Z-beam): sensor layout. Paired top/bottom at $\xi = 0.2$ on each element; top-only at $\xi = 0.8$. All sensors lie on the mid-width line ($y = 0$).

Measured channels (SSB input). Surface axial strains ε_s at the available offsets ($y_i = 0,\ z_i = \pm h/2$) are the same as in Case A at the corresponding stations; here, the bottom reading at $\xi = 0.8$ is *not* used. Table 6.22 collects the channels by element and station (a dash marks unavailable sensors).

Table 6.22: Case B — Measured surface strains ε_s (dimensionless) at sensor stations. Top/bottom refer to $z = \pm h/2$; "—" denotes an intentionally absent sensor (top-only at $\xi = 0.8$).

Element	ξ	$\varepsilon_s^{\text{top}}$	$\varepsilon_s^{\text{bot}}$
1	0.2	0.0241	−0.0239
1	0.8	0.0241	—
2	0.2	0.0192	−0.0192
2	0.8	0.0048	—
3	0.2	0.0001	0.0001
3	0.8	0.0001	—

2) Reference (comparison target)

The reference nodal displacement vector $\mathbf{q}^{\text{ref}}$ is provided by the same forward FEM tool used in Case A. Accordingly, the comparison is performed on the known in-plane DOFs at nodes 2–4:

$$(u_2, w_2, \phi_{y2}, u_3, w_3, \phi_{y3}, u_4, w_4, \phi_{y4}),$$

whose reference values coincide with those listed in Table 6.18.

3) Reconstruction results

With the reduced-but-informative layout of Table 6.22, the SSB-iFEM reproduces the reference solution with essentially zero error.

Table 6.23: Case B — Nodal quantities at free nodes (values). u, w in m; ϕ_y in rad.

Node	DOF	Unit	Reference	SSB
2	u	m	3.0000e−3	3.0000e−3
2	w	m	−2.1600e1	−2.1600e1
2	ϕ_y	rad	−1.4400	−1.4400
3	u	m	8.3203e1	8.3203e1
3	w	m	−2.1600e1	−2.1600e1
3	ϕ_y	rad	−2.4000	−2.4000
4	u	m	8.3207e1	8.3207e1
4	w	m	−1.1760e2	−1.1760e2
4	ϕ_y	rad	−2.4000	−2.4000

Global relative metrics (free nodes, known DOFs) confirm the negligible discrepancy:

$$\frac{\|\mathrm{err}\|_\infty}{\|\mathrm{ref}\|_\infty} = 9.226 \times 10^{-13}, \qquad \frac{\|\mathrm{err}\|_2}{\|\mathrm{ref}\|_2} = 9.216 \times 10^{-13}.$$

For completeness, per–element relative figures are 8.467×10^{-13} and 8.482×10^{-13} on Element 1, 9.252×10^{-13} and 9.166×10^{-13} on Element 2, and 9.226×10^{-13} and 9.228×10^{-13} on Element 3 (for $\|\cdot\|_\infty/\|\cdot\|_\infty$ and $\|\cdot\|_2/\|\cdot\|_2$, respectively). The node-wise relative errors reported by the solver are effectively zero (machine precision) for all DOFs.

Sensor diagnostics. For each element, the left bar–plot reports the residuals of the surface–strain channels,

$$r_i \;=\; \varepsilon_{s,i}^{\mathrm{pred}} \;-\; \varepsilon_{s,i}^{\mathrm{meas}},$$

with one bar per sensor in the order used by the input arrays (three channels per element: top and bottom at $\xi = 0.2$, top-only at $\xi = 0.8$). The predicted strain at station ξ_i (with local offsets y_i, z_i) is obtained from the reconstructed local DOFs $\mathbf{q}_{\mathrm{loc}}$ via

$$\varepsilon_{s,i}^{\mathrm{pred}} \;=\; \Big(\mathbf{B}_u(\xi_i) \;+\; z_i\, \mathbf{B}_w(\xi_i) \;+\; y_i\, \mathbf{B}_v(\xi_i) \Big)\, \mathbf{q}_{\mathrm{loc}}.$$

The right scatter–plots compare measured vs. predicted strains (one marker per sensor) and include the 1:1 reference line; points lying on the 1:1 indicate perfect agreement, whereas systematic offsets (parallel clouds) and slope deviations would reveal bias or scaling effects.

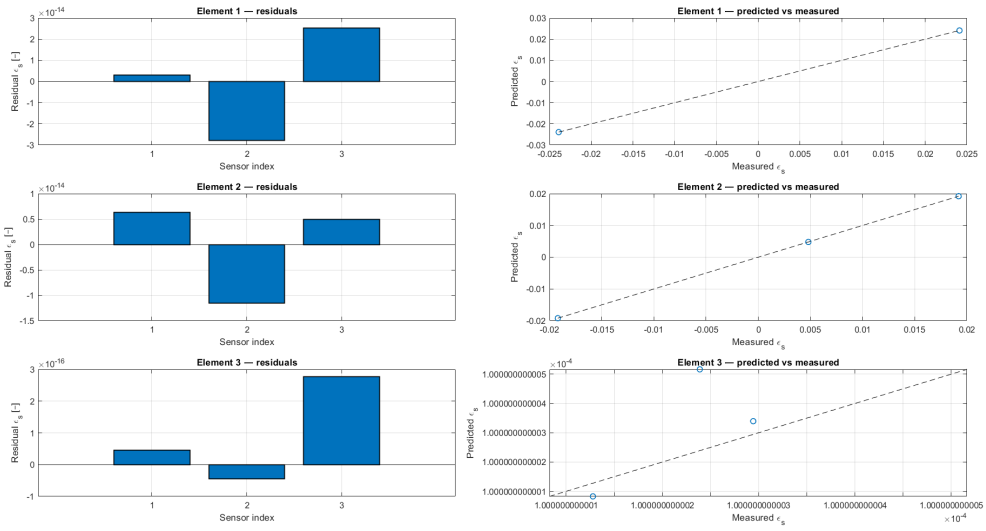

Figure 6.16: Case B (Z-beam). Left: sensor residuals by element. Right: predicted vs measured ε_s with 1:1 guideline.

4) Discussion

- **Accuracy with reduced channels.** Despite the missing bottom reading at $\xi = 0.8$ on each element, the paired station at $\xi = 0.2$ plus a single top channel at $\xi = 0.8$ is sufficient to reproduce (u, w, ϕ_y) at essentially machine precision on the Z-beam.
- **Diagnostics.** The residual and 1:1 plots (Fig. 6.16) show negligible bias and dispersion, corroborating the metric-based assessment and confirming that the strain data are fully consistent with the reconstructed displacement field.
- **Implication.** Case B confirms that SSB-iFEM remains robust under mild accessibility constraints (paired+single-sided layout) also for the more articulated Z-beam, anticipating the more restrictive layouts explored in Cases C–D.

6.3.3 Case C — SSB-iFEM: top sensors at $\xi = 0.2$, $\xi = 0.8$; bottom sensor at $\xi = 0.5$

1) Setup and instrumentation

The geometry, mesh, and boundary conditions are those of Section 6.3. Each element is instrumented with three surface–strain gauges along the mid-width

line ($y = 0$): *top* face at $\xi = 0.2$, *bottom* face at $\xi = 0.5$, and *top* face at $\xi = 0.8$ (i.e., $z = \{+h/2, -h/2, +h/2\}$ for all three elements).

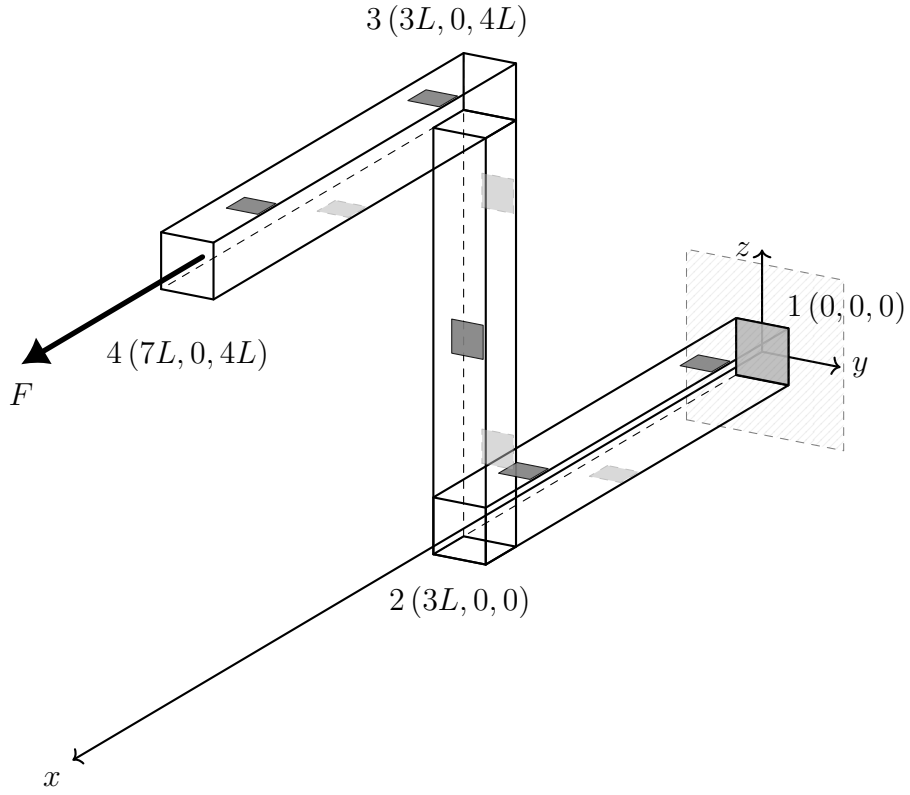

Figure 6.17: Case C (Z-beam): sensor layout. Top sensors at $\xi = 0.2$ and $\xi = 0.8$; bottom sensor at $\xi = 0.5$ on each element. All sensors lie on the mid-width line ($y = 0$).

Measured channels. *SSB-iFEM input* consists of the surface axial strains ε_s at the sensor offsets. Table 6.24 lists the measured values (rounded) at the three stations of each element.

Table 6.24: Case C — Measured surface axial strains ε_s (dimensionless) at sensor stations for all three elements. Sensors lie on the mid-width line ($y = 0$) at $z = \pm h/2$ (top/bottom).

Element	ξ	Face	ε_s
1	0.2	top	0.0241
1	0.5	bottom	−0.0239
1	0.8	top	0.0241
2	0.2	top	0.0192
2	0.5	bottom	−0.0120
2	0.8	top	0.0048
3	0.2	top	0.0001
3	0.5	bottom	0.0001
3	0.8	top	0.0001

2) Reference (comparison target)

The reference nodal displacement vector $\mathbf{q}^{\text{ref}}$ is provided by the same forward FEM tool used in Cases A–B. The comparison is performed on the known in-plane DOFs at nodes 2–4:

$$(u_2, w_2, \phi_{y2}, u_3, w_3, \phi_{y3}, u_4, w_4, \phi_{y4}),$$

whose reference values are those already listed in Table 6.18.

3) Reconstruction results

Using the SSB inputs of Table 6.24, the inverse analysis matches the reference within numerical precision.

Table 6.25: Case C — Nodal quantities at free nodes (values). u, w in m; ϕ_y in rad.

Node	DOF	Unit	Reference	SSB
2	u	m	3.0000e−3	3.0000e−3
2	w	m	−2.1600e1	−2.1600e1
2	ϕ_y	rad	−1.4400	−1.4400
3	u	m	8.3203e1	8.3203e1
3	w	m	−2.1600e1	−2.1600e1
3	ϕ_y	rad	−2.4000	−2.4000
4	u	m	8.3207e1	8.3207e1
4	w	m	−1.1760e2	−1.1760e2
4	ϕ_y	rad	−2.4000	−2.4000

Relative error metrics. Global relative errors (excluding constrained DOFs) and per–element summaries are reported below. Here $\|\cdot\|_\infty$ is the max norm over the stacked vector of nodal DOFs, and $\|\cdot\|_2$ the Euclidean norm; we quote the ratio $\|\text{err}\|/\|\text{ref}\|$ as provided by the post-processor.

Table 6.26: Case C — Global relative error metrics (free nodes).

Metric	Value
$\|\text{err}\|_\infty/\|\text{ref}\|_\infty$	2.1470e−13
$\|\text{err}\|_2/\|\text{ref}\|_2$	2.1550e−13

Table 6.27: Case C — Per–element relative errors.

Element	$\|\text{err}\|_\infty/\|\text{ref}\|_\infty$	$\|\text{err}\|_2/\|\text{ref}\|_2$
1	2.1180e−13	2.1190e−13
2	2.1640e−13	2.1600e−13
3	2.1470e−13	2.1550e−13

The node-wise relative errors reported by the solver are effectively zero (printed as 0.000 %) for all DOFs at nodes 2–4.

Sensor diagnostics. For each element, the left bar–plot reports the residuals of the surface–strain channels,

$$r_i \;=\; \varepsilon_{s,i}^{\text{pred}} \;-\; \varepsilon_{s,i}^{\text{meas}},$$

with one bar per sensor in the order used by the input arrays (three channels per element, corresponding to the stations at $\xi = 0.2$, 0.5, and 0.8). The predicted strain at station ξ_i (with local offsets y_i, z_i) is obtained from the reconstructed local DOFs $\mathbf{q}_{\text{loc}}$ via

$$\varepsilon_{s,i}^{\text{pred}} \;=\; \Big(\mathbf{B}_u(\xi_i) \;+\; z_i\,\mathbf{B}_w(\xi_i) \;+\; y_i\,\mathbf{B}_v(\xi_i)\Big)\,\mathbf{q}_{\text{loc}}.$$

The right scatter–plots compare measured vs. predicted strains (one marker per sensor) and include the 1:1 reference line; points lying on the 1:1 indicate perfect agreement, whereas systematic offsets (parallel clouds) and slope deviations would reveal bias or scaling effects.

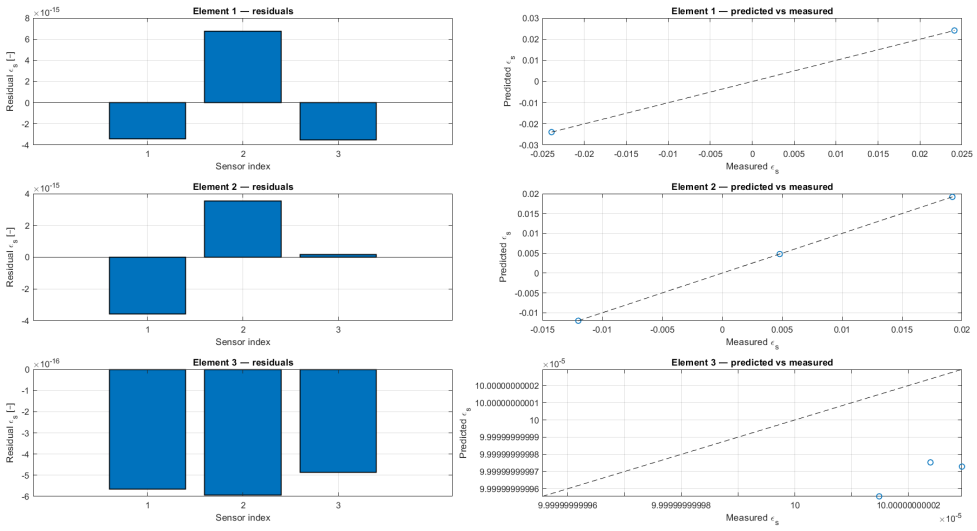

Figure 6.18: Case C (Z-beam). Left: residuals per sensor (Elements 1–3 from top to bottom). Right: predicted vs. measured ε_s with 1:1 guideline.

4) Discussion

- **Accuracy with mixed sidedness.** A three-sensor layout per element (top–bottom–top at $\xi = 0.2, 0.5, 0.8$) still achieves agreement with the reference solution at essentially machine precision. The bottom station at $\xi = 0.5$ restores local pairing for bending about y, maintaining excellent observability of (u, w, ϕ_y) on the Z-beam.

- **Practical note.** Even without full pairing at all stations, distributing the three sensors as in Case C provides a robust constraint set for SSB on this more articulated Z-shaped structure.

6.3.4 Case D — SSB-iFEM: top-only sensors at $\xi = 0.2, 0.5, 0.8$

1) Setup and instrumentation

Geometry, mesh, kinematics, and boundary conditions are those of Section 6.3. Each element is instrumented with *three top-face* surface–strain sensors at parent abscissae $\xi = \{0.2, 0.5, 0.8\}$; all stations lie on the mid-width line ($y = 0$) and at $z = +h/2$ (top).

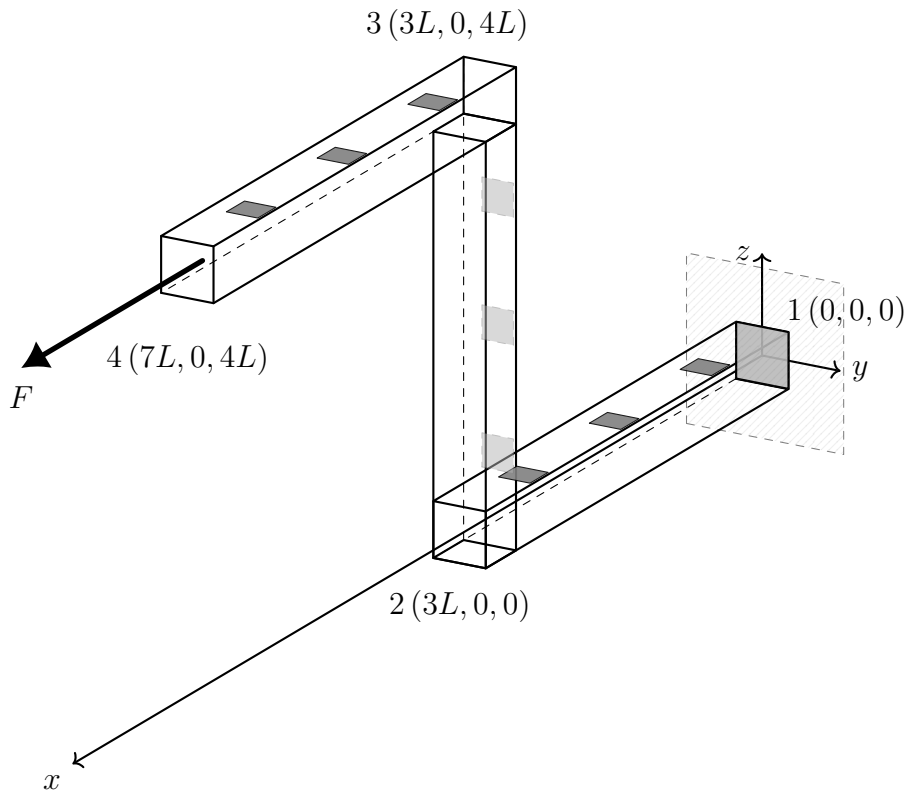

Figure 6.19: Case D (Z-beam): sensor layout. Top-only sensors at $\xi = \{0.2, 0.5, 0.8\}$ on each element; all sensors on the mid-width line ($y = 0$).

Measured channels. The SSB-iFEM input consists of the surface axial strains ε_s at the sensor offsets (top face, $z = +h/2$). The measured values are:

Table 6.28: Case D — Measured surface axial strains ε_s (dimensionless) at the three top-face stations on each element.

Element	ξ	$\varepsilon_s(0.2)$	$\varepsilon_s(0.5)$	$\varepsilon_s(0.8)$
1		0.0241	0.0241	0.0241
2		0.0192	0.0120	0.0048
3		0.0001	0.0001	0.0001

2) Reference (comparison target)

As in the previous cases, the forward FEM solver provides the *reference* nodal DOFs at the free nodes

$$(u_2, w_2, \phi_{y2}, u_3, w_3, \phi_{y3}, u_4, w_4, \phi_{y4}),$$

which are the same reference values reported in Table 6.18. Only the SSB-iFEM reconstruction is considered here, since the classical iFEM formulation would require paired top/bottom measurements to build curvature channels.

3) Reconstruction results

With top-only instrumentation ($y_i = 0$ and $z_i = +h/2$ at all stations), the SSB system lacks the paired top/bottom information needed to disentangle mid-line strain ε from bending curvature κ_{zz}. Consequently, the inverse fit becomes ill-conditioned and the reconstructed nodal quantities deviate markedly from the reference solution.

Nodal values and relative errors. Table 6.29 reports SSB vs. reference at free nodes, together with the relative error (in %).

Table 6.29: Case D — Nodal quantities at free nodes (values and relative errors). u, w in m; ϕ_y in rad.

Node	DOF	Unit	SSB	Reference	Rel. err [%]
2	u	m	9.1050e−1	3.0000e−3	30 249.7100
2	w	m	5.6250	−2.1600e1	126.0400
2	ϕ_y	rad	−3.7500e−1	1.4400	126.0400
3	u	m	−1.3620e−1	8.3200e1	100.1640
3	w	m	5.9160	−2.1600e1	127.3890
3	ϕ_y	rad	2.6490e−3	2.4000	99.8900
4	u	m	−2.3700e−1	8.3210e1	100.2850
4	w	m	1.6190	−1.1760e2	101.3770
4	ϕ_y	rad	2.1220e−1	2.4000	91.1590

Aggregate relative metrics. Global relative errors (excluding constrained DOFs) and per–element figures are summarised in Table 6.30. Here $\|\cdot\|_\infty$ is the infinity norm (max absolute component) and $\|\cdot\|_2$ is the Euclidean norm.

Table 6.30: Case D — Relative errors w.r.t. the reference solution.

Quantity	$\|\text{err}\|_\infty/\|\text{ref}\|_\infty$	$\|\text{err}\|_2/\|\text{ref}\|_2$
Whole structure	1.0140	1.0180
Element 1	1.2600	1.2610
Element 2	1.0020	1.0370
Element 3	1.0140	1.0130

4) Discussion

- **Observability shortfall.** With top-only sensors ($z = +h/2$ at all stations), the SSB prediction operator cannot separate the mid-line strain ε from the curvature κ_{zz}; the problem is effectively under–determined and ill-conditioned.
- **Impact on accuracy.** The loss of pairing drives very large biases at the free nodes (Table 6.29) and near-unit (or larger) global relative errors (Table 6.30), in stark contrast with the machine-precision reconstructions of Cases A–C.
- **Design implication.** For Euler–Bernoulli beams such as the present Z-configuration, at least one paired top/bottom station per element (or equivalent multi-face information) is necessary to achieve accurate reconstructions of (u, w, ϕ_y); purely single-sided layouts should be avoided unless supplemented by additional information or regularisation.

6.4 Structure 3: Hinged T-Beam

Geometry and mesh. The T-beam is modeled as a three–element Euler–Bernoulli (EB) assembly lying in the global X–Z plane. The nodal coordinates (in metres) are

$$\mathbf{x}_1 = (0,0,0), \qquad \mathbf{x}_2 = (8L,0,0), \qquad \mathbf{x}_3 = (3L,0,3L), \qquad \mathbf{x}_4 = (3L,0,0),$$
$$L = 10.$$

Element connectivity is

$$\mathcal{C}_e = \{(1,4),\,(4,2),\,(4,3)\},$$

so that two elements form the horizontal flange and one element forms the vertical web of the T. Each element adopts a local frame with x_{loc} aligned with the element axis, $y_{\text{loc}} \parallel Y$, and $z_{\text{loc}} = x_{\text{loc}} \times y_{\text{loc}}$, so that $\mathbf{\Lambda}_e$ consistently maps local EB DOFs to the global frame.

Cross-section. A constant rectangular cross-section is assumed with width $b = 1$ (along y) and height $h = 1$ (along z). Only geometric data enter the inverse formulation; material properties are not required by iFEM.

Kinematics and sign conventions. All operators follow the EB kinematics and the sign convention of Chapter 2: $\phi_y = -w_{,x}$, $\omega_z = v_{,x}$, $\kappa_{zz} = -w_{,xx}$, $\kappa_{yy} = -v_{,xx}$. Element operators are evaluated in local frames and rotated to the global frame by $\mathbf{\Lambda}_e$ prior to assembly.

Boundary conditions. Hinged supports are imposed at nodes 1 and 2: all translational DOFs and the out-of-plane rotation are fixed, while the in-plane rotation about the Y axis is free,

$$u = v = w = \omega_z = 0, \qquad \phi_y \text{ free at nodes } 1,2.$$

To restrict the analysis to in-plane response (X–Z), the out-of-plane DOFs are also suppressed at the internal nodes by enforcing $v = \omega_z = 0$ at nodes 3 and 4. Kinematic compatibility at the junction node 4 (intersection between flange and web) is enforced automatically by the common nodal DOFs.

Static deformed configurations (visualization). Two reference static solutions from the forward FEM solver are used: a nodal load at node 3 along global $+X$, $\mathbf{F} = \{10^{-4}, 0, 0\}$ N (Fig. 6.20, cases A–D), and a distributed load

$q_x = 5 \times 10^{-4}$ N/m on the vertical web between nodes 4 and 3 in the global $+X$ direction (Fig. 6.21, cases E–F).

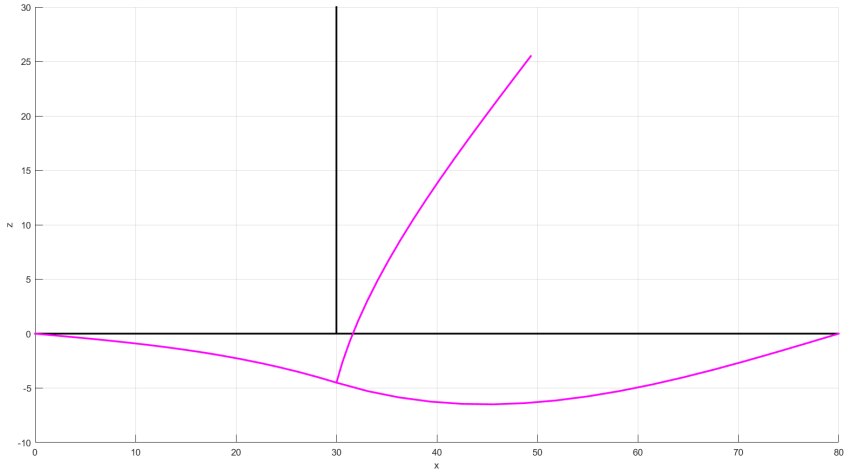

Figure 6.20: Hinged T-beam — static deformed configuration under a nodal load $\mathbf{F} = \{10^{-4}, 0, 0\}$ N at node 3 (global $+X$). Black: undeformed centerline; magenta: deformed shape. Axes in metres. This deformed shape is used for cases A–D.

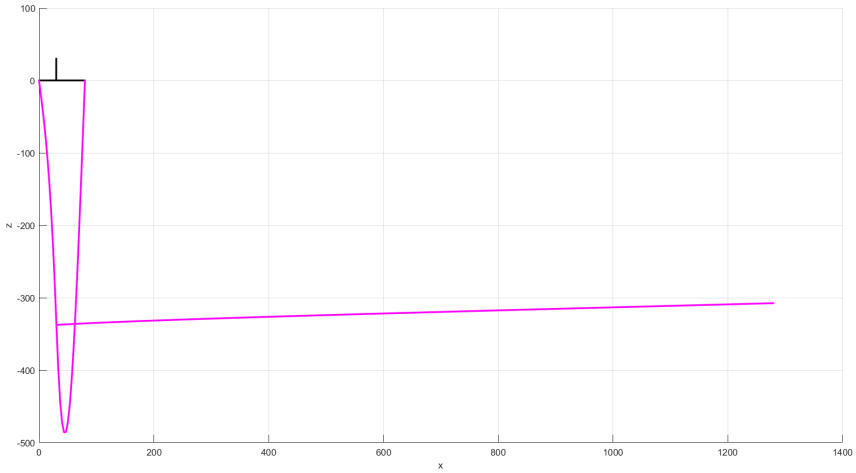

Figure 6.21: Hinged T-beam — static deformed configuration under a distributed load $q_x = 5 \times 10^{-4}$ N/m applied along the vertical web (element 4–3) in the global $+X$ direction. Black: undeformed centerline; magenta: deformed shape. Axes in metres. This deformed shape is used for cases E–F.

Sensor stations (cases A–F). Sensor abscissae are parameterized by the parent coordinate $\xi = x/L \in [0, 1]$ on each element. For the hinged T-beam, the following layouts are considered:

- *Case A* — Paired top/bottom sensors at $\xi = \{0.2, 0.8\}$ on each element (baseline comparison with classical iFEM).
- *Case B* — Paired sensors at $\xi = 0.2$ and top-only sensor at $\xi = 0.8$ on each element.
- *Case C* — Top sensors at $\xi = 0.2, 0.8$ and bottom sensor at $\xi = 0.5$ (top–bottom–top layout).
- *Case D* — Top-only sensors at $\xi = 0.2, 0.5, 0.8$ on each element.
- *Case E* — Same sensor layout as Case B, but the vertical web (between nodes 4 and 3) is subjected to a distributed load $q_x = 5 \times 10^{-4}$ N/m along global $+X$. In the forward FEM model used to generate the reference data the web is discretized into four equal EB elements, whereas the inverse model retains a single EB element for this segment.
- *Case F* — As in Case E (same distributed loading and forward FEM mesh), but the inverse model also subdivides the vertical web into two EB elements, each instrumented according to the Case B layout (paired at $\xi = 0.2$ and top-only at $\xi = 0.8$).

Unless otherwise noted, sensors lie on the mid-width line ($y = 0$), and their offsets (y_i, z_i) enter the prediction operator via

$$\mathbf{A}_i = \mathbf{B}_u(\xi_i) + z_i\,\mathbf{B}_w(\xi_i) + y_i\,\mathbf{B}_v(\xi_i)$$

(cf. Chapter 3).

6.4.1 Case A — Classical iFEM vs SSB-iFEM (baseline)

1) Setup and instrumentation

The geometry, mesh, and boundary conditions are those detailed in Section 6.4. Two axial stations per element are instrumented at parent abscissae $\xi = \{0.2, 0.8\}$. All gauges lie on the mid-width line ($y = 0$) and are mounted in paired configuration on the top/bottom faces ($z = \pm h/2$), as sketched in Fig. 6.22. The resulting surface-strain measurements used by the SSB-iFEM are reported in Table 6.31.

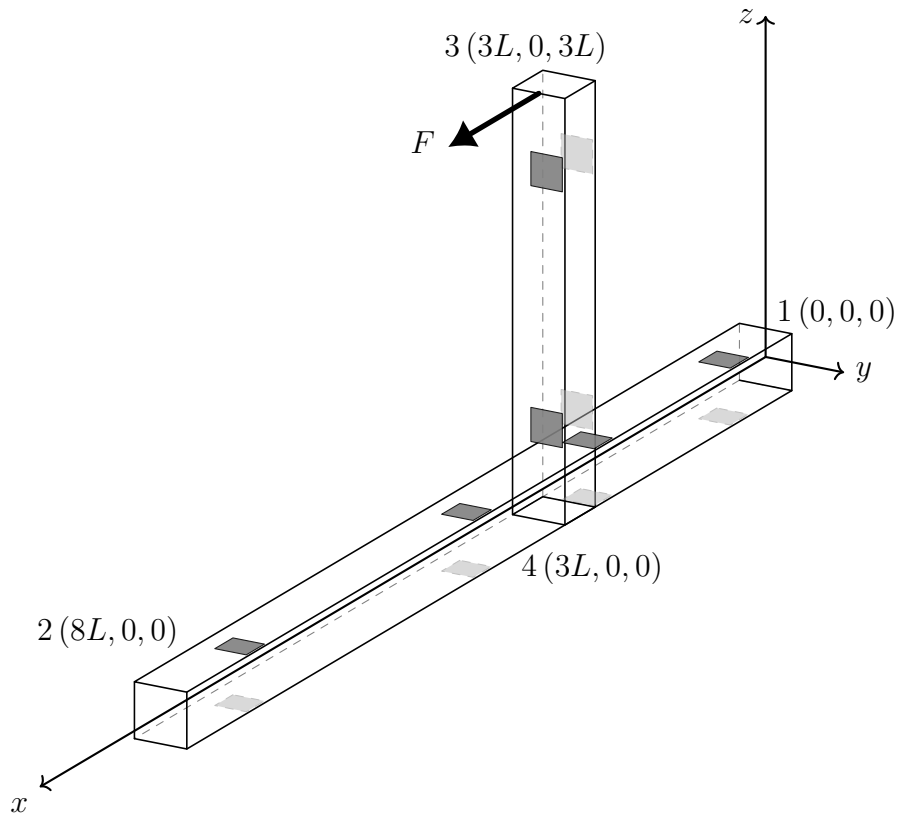

Figure 6.22: Hinged T-beam: geometry, global axes, pinned supports at nodes 1 and 2, and paired sensors at $\xi = \{0.2, 0.8\}$ on the top/bottom faces of all three elements. Cross-section $b = h = 1$. The symbolic load F is used only to illustrate the static deformed configuration elsewhere.

Measured channels (SSB input). The *SSB-iFEM* uses the surface axial strains ε_s recorded at the sensor offsets; the complete dataset across elements and stations is summarized in Table 6.31.

Table 6.31: Case A — Measured surface axial strains ε_s (dimensionless) at sensor stations for all three elements. Sensors lie on the mid-width line ($y = 0$) at $z = \pm h/2$ (top/bottom).

Element	ξ	$\varepsilon_s^{\text{top}}$	$\varepsilon_s^{\text{bot}}$
1	0.2	0.0014	−0.0013
1	0.8	0.0055	−0.0053
2	0.2	−0.0090	0.0090
2	0.8	−0.0023	0.0022
3	0.2	0.0144	−0.0144
3	0.8	0.0036	−0.0036

Classical channels (derived from paired faces). The *classical* EB iFEM uses mid-line strain and curvature channels constructed from the paired faces at the same section. With $h = 1$,

$$\varepsilon = \tfrac{1}{2}\left(\varepsilon_s^{\text{top}} + \varepsilon_s^{\text{bot}}\right), \qquad \kappa_{zz} = \varepsilon_s^{\text{top}} - \varepsilon_s^{\text{bot}}, \qquad (\kappa_{yy} = 0 \text{ since } y_i = 0).$$

Applying these relations to Table 6.31 yields the classical channels collected in Table 6.32.

Table 6.32: Case A — Classical iFEM channels at sensor stations. Mid-line axial strain ε (dimensionless) and bending curvature κ_{zz} [m^{-1}].

Element	ξ	ε	κ_{zz}
1	0.2	6.2500e−5	2.7000e−3
1	0.8	6.2500e−5	1.0800e−2
2	0.2	−3.7500e−5	−1.8000e−2
2	0.8	−3.7500e−5	−4.5000e−3
3	0.2	0.0000	2.8800e−2
3	0.8	0.0000	7.2000e−3

2) Reference

The independent forward FEM solver (provided by the advisor) supplies the global nodal displacement vector used as reference solution. For the in-plane DOFs at nodes 2–4 (ordered as $(u_2, w_2, \phi_{y2}; u_3, w_3, \phi_{y3}; u_4, w_4, \phi_{y4})$) we obtain

$$\mathbf{q}^{\text{ref}} = \begin{bmatrix} 0.0000 & 0.0000 & 2.7750\text{e}{-1} \\ 1.9352\text{e}1 & -4.5000 & -8.2500\text{e}{-1} \\ 1.8750\text{e}{-3} & -4.5000 & -2.8500\text{e}{-1} \end{bmatrix}^{\top},$$

which are the reference values also reported in Table 6.33 for direct comparison against the reconstructions.

3) Reconstruction results

Using the SSB inputs of Table 6.31 and the classical channels of Table 6.32, both inverse schemes deliver virtually identical reconstructions at the supported and internal nodes. Unless otherwise noted, all metrics are computed on the vector of nodal discrepancies with respect to the reference solution, restricted to the known in-plane DOFs at nodes 2–4, ordered as $(u_2, w_2, \phi_{y2}, u_3, w_3, \phi_{y3}, u_4, w_4, \phi_{y4})$.

Table 6.33: Case A — Nodal quantities at free/supported nodes (values). u, w in m; ϕ_y in rad. The three columns (Reference, SSB, CLS) enable a direct side-by-side comparison with the reference solution.

Node	DOF	Unit	Reference	SSB	CLS
2	u	m	0.0000	0.0000	0.0000
2	w	m	0.0000	0.0000	0.0000
2	ϕ_y	rad	2.7750e−1	2.7750e−1	2.7750e−1
3	u	m	1.9352e1	1.9352e1	1.9352e1
3	w	m	−4.5000	−4.5000	−4.5000
3	ϕ_y	rad	−8.2500e−1	−8.2500e−1	−8.2500e−1
4	u	m	1.8750e−3	1.8750e−3	1.8750e−3
4	w	m	−4.5000	−4.5000	−4.5000
4	ϕ_y	rad	−2.8500e−1	−2.8500e−1	−2.8500e−1

All SSB and CLS entries coincide with the reference values within plotting precision, showing that both inverse schemes reproduce the nodal DOFs essentially exactly in this baseline, fully paired layout.

Table 6.34: Case A — Direct nodal differences (Δ = SSB − CLS) at nodes 2–4. These entries quantify the method-to-method discrepancy per DOF.

Node	DOF	Δu [m]	Δw [m]	$\Delta\phi_y$ [rad]
2		0.0000	0.0000	−4.3850e−14
3		−4.6900e−13	1.1590e−12	1.5990e−14
4		2.3850e−18	1.1590e−12	1.5710e−14

All differences are at the level of numerical round-off ($\sim 10^{-12}$ or smaller compared to the absolute DOF magnitudes), confirming that SSB and CLS deliver practically indistinguishable nodal reconstructions.

Table 6.35: Case A — Global metrics w.r.t. reference solution (nodes 2–4). Definitions for an error vector $e \in \mathbb{R}^n$: RMSE $= \sqrt{\frac{1}{n}\sum_{i=1}^{n} e_i^2}$, $\|e\|_\infty = \max_i |e_i|$. Here e stacks (SSB−ref) or (CLS−ref) on $(u_2, w_2, \phi_{y2}, u_3, w_3, \phi_{y3}, u_4, w_4, \phi_{y4})$.

Metric	SSB	CLS
RMSE	2.2530e−14	5.3670e−13
$\|\cdot\|_\infty$	4.8850e−14	1.2080e−12

Table 6.36: Case A — Aggregate SSB–CLS discrepancy at nodes 2–4 (global metrics). Definitions for the method-to-method difference vector $d \in \mathbb{R}^n$ (SSB−CLS): RMSE $= \sqrt{\frac{1}{n}\sum_{i=1}^{n} d_i^2}$, $\|d\|_\infty = \max_i |d_i|$, $\|d\|_1 = \sum_{i=1}^{n} |d_i|$.

Metric	SSB − CLS
RMSE	4.4040e−13
$\|\cdot\|_\infty$	1.1590e−12
$\|\cdot\|_1$	1.9080e−13

These aggregate figures condense the small per-DOF differences of Table 6.34 into vector norms. The values remain very small, reinforcing the baseline equivalence between SSB-iFEM and classical iFEM for the present, fully paired layout on the hinged T-beam.

Element-wise field differences. Figures 6.23–6.25 plot the pointwise differences $\Delta u(s) = u_{\mathrm{SSB}}(s) - u_{\mathrm{CLS}}(s)$ and $\Delta w(s) = w_{\mathrm{SSB}}(s) - w_{\mathrm{CLS}}(s)$ along the local abscissa s of each element (markers at the instrumented stations). The curves remain at round-off across all three elements, including at the measurement stations, showing that the two inverse schemes reconstruct essentially the same fields.

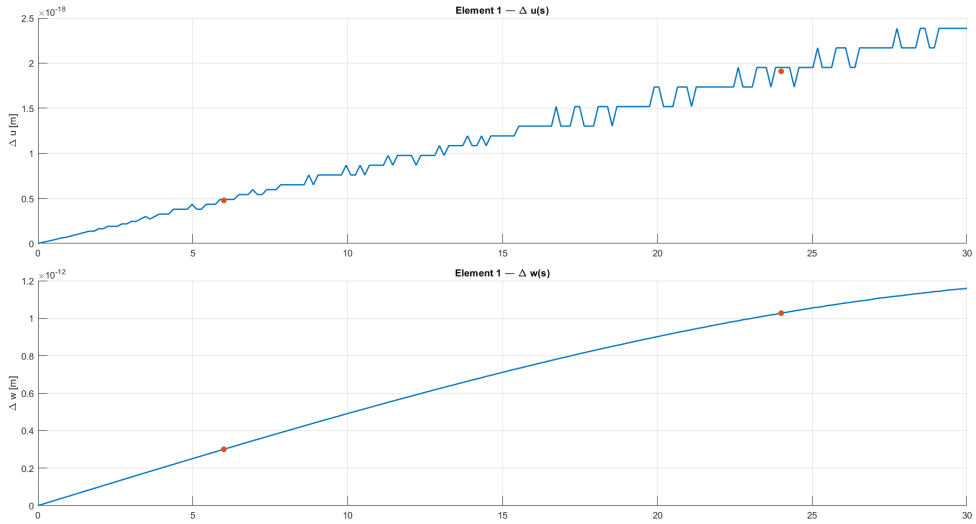

Figure 6.23: Case A (T-beam), Element 1. Pointwise differences $\Delta u(s)$ and $\Delta w(s)$ between SSB and classical iFEM. Markers: sensor stations at $\xi = \{0.2, 0.8\}$.

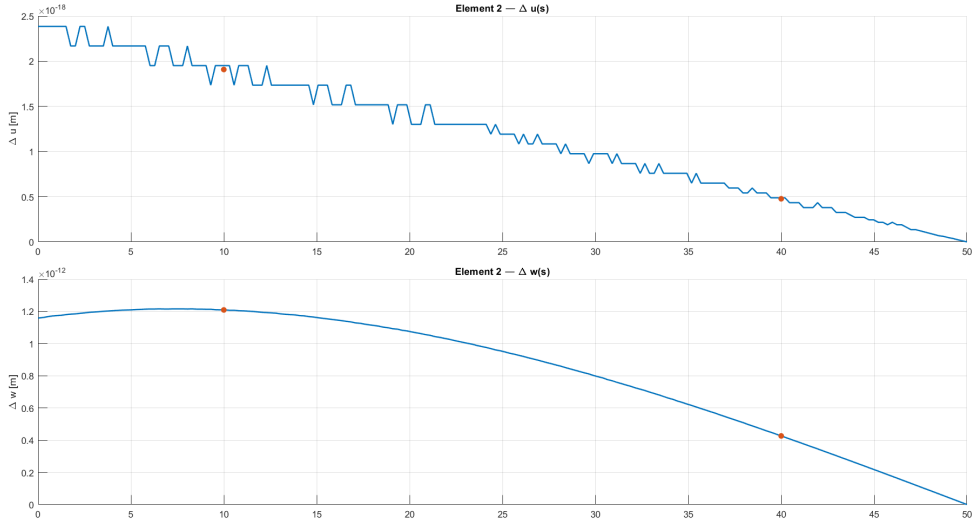

Figure 6.24: Case A (T-beam), Element 2. Pointwise differences $\Delta u(s)$ and $\Delta w(s)$ between SSB and classical iFEM. Markers: sensor stations at $\xi = \{0.2, 0.8\}$.

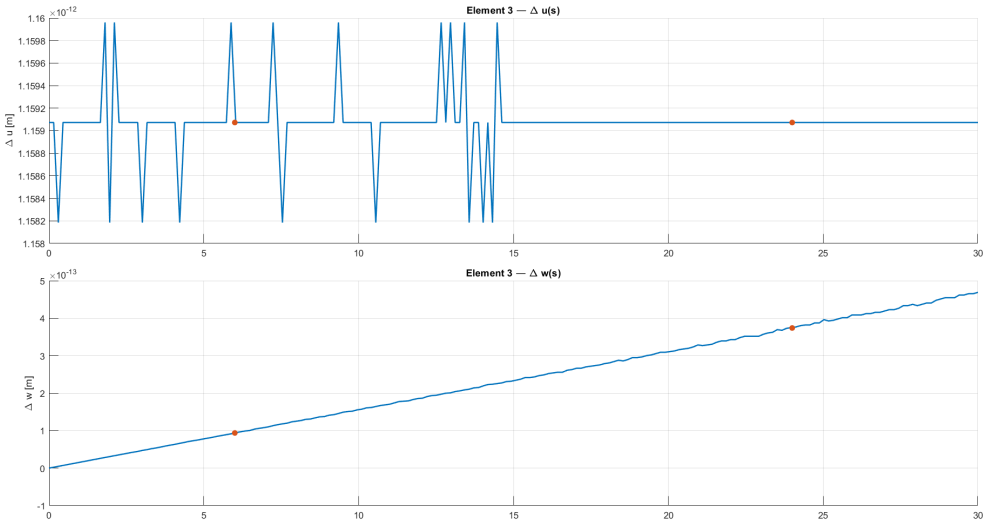

Figure 6.25: Case A (T-beam), Element 3. Pointwise differences $\Delta u(s)$ and $\Delta w(s)$ between SSB and classical iFEM. Markers: sensor stations at $\xi = \{0.2, 0.8\}$.

4) Discussion

- **Baseline equivalence.** With paired top/bottom sensors at both stations and $y_i = 0$, SSB-iFEM and classical EB iFEM achieve coincident reconstructions up to numerical round-off (Tables 6.34–6.36; Figs. 6.23–6.25).
- **Implication for subsequent cases.** The results confirm that full pairing on accessible faces is sufficient for high-accuracy recovery of (u, w, ϕ_y) on the hinged T-beam. Sections 6.4.2–6.4.4 (and the distributed-load cases E–F) progressively relax pairing and sidedness to assess robustness under practical accessibility and loading constraints.

6.4.2 Case B — SSB-iFEM: paired sensors at $\xi = 0.2$ and top sensor at $\xi = 0.8$

1) Setup and instrumentation

The geometry, mesh, kinematics, boundary conditions, and sign convention are the same as in Section 6.4. Instrumentation differs from Case A as follows: for each element, two axial stations are used at parent abscissae $\xi = \{0.2, 0.8\}$; at $\xi = 0.2$ a *paired* top/bottom installation is available on the mid-width line ($y = 0$, faces $z = \pm h/2$), while at $\xi = 0.8$ only the *top* face ($z = +h/2$) is instrumented.

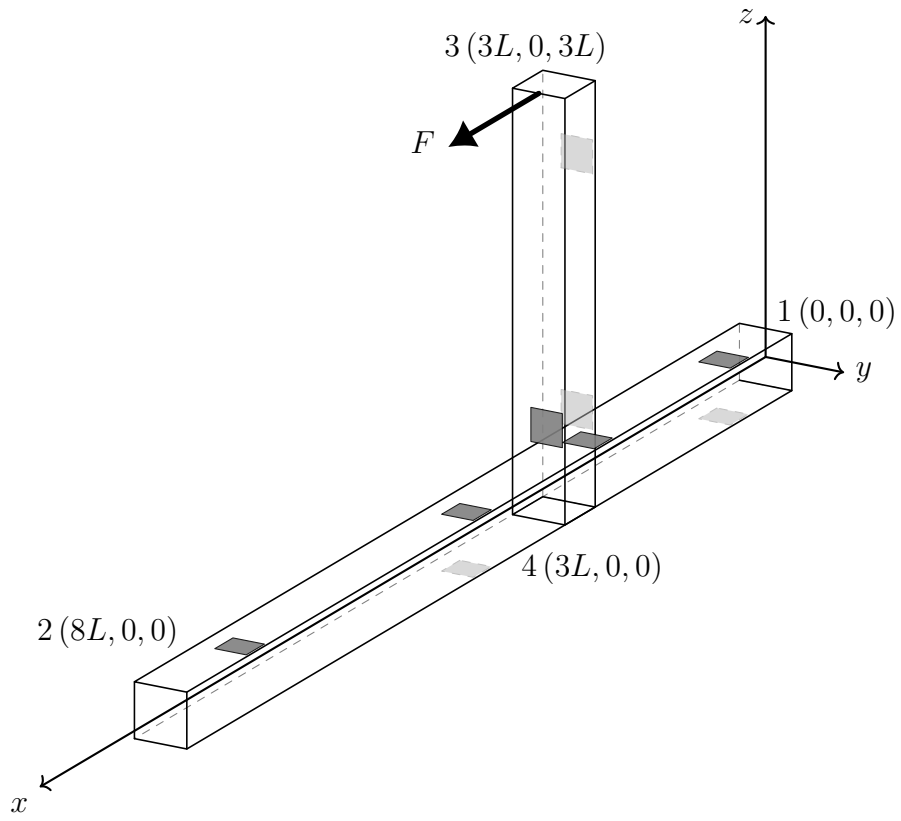

Figure 6.26: Case B (T-beam): sensor layout. Paired top/bottom at $\xi = 0.2$ on each element; top-only at $\xi = 0.8$. All sensors lie on the mid-width line ($y = 0$).

Measured channels (SSB input). Surface axial strains ε_s at the available offsets ($y_i = 0,\ z_i = \pm h/2$) are those of Case A at the same stations; here, the bottom reading at $\xi = 0.8$ is *not* used. Table 6.37 collects the channels by element and station (a dash marks unavailable sensors).

Table 6.37: Case B (T-beam) — Measured surface strains ε_s (dimensionless) at sensor stations. Top/bottom refer to $z = \pm h/2$; "—" denotes an intentionally absent sensor (top-only at $\xi = 0.8$).

Element	ξ	$\varepsilon_s^{\text{top}}$	$\varepsilon_s^{\text{bot}}$
1	0.2	0.0014	−0.0013
1	0.8	0.0055	—
2	0.2	−0.0090	0.0090
2	0.8	−0.0023	—
3	0.2	0.0144	−0.0144
3	0.8	0.0036	—

2) Reference (comparison target)

The reference nodal displacement vector $\mathbf{q}^{\text{ref}}$ is the same as in Case A (Section 6.4.1), supplied by the forward FEM solver for the hinged T-beam. Accordingly, the comparison is performed on the known in-plane DOFs at nodes 2–4,

$$(u_2, w_2, \phi_{y2}, u_3, w_3, \phi_{y3}, u_4, w_4, \phi_{y4}),$$

whose reference values are those reported in Table 6.33.

3) Reconstruction results

With the reduced-but-still-informative layout of Table 6.37, the SSB-iFEM reproduces the reference solution with practically zero error.

Table 6.38: Case B (T-beam) — Nodal quantities at free nodes (values). u, w in m; ϕ_y in rad.

Node	DOF	Unit	Reference	SSB
2	u	m	0.0000	0.0000
2	w	m	0.0000	0.0000
2	ϕ_y	rad	2.7750e−1	2.7750e−1
3	u	m	1.9352e1	1.9352e1
3	w	m	−4.5000	−4.5000
3	ϕ_y	rad	−8.2500e−1	−8.2500e−1
4	u	m	1.8750e−3	1.8750e−3
4	w	m	−4.5000	−4.5000
4	ϕ_y	rad	−2.8500e−1	−2.8500e−1

Global relative metrics (excluding constrained DOFs) confirm the negligible discrepancy:

$$\frac{\|\mathrm{err}\|_\infty}{\|\mathrm{ref}\|_\infty} = 4.117 \times 10^{-14}, \qquad \frac{\|\mathrm{err}\|_2}{\|\mathrm{ref}\|_2} = 5.532 \times 10^{-14}.$$

Per–element figures reported by the post-processor are 1.770×10^{-13} and 1.768×10^{-13} on Element 1, 1.770×10^{-13} and 1.764×10^{-13} on Element 2, and 4.117×10^{-14} and 5.529×10^{-14} on Element 3 (for $\|\cdot\|_\infty/\|\cdot\|_\infty$ and $\|\cdot\|_2/\|\cdot\|_2$, respectively). The node-wise relative errors reported by the solver are essentially zero (machine precision) for all DOFs.

Sensor diagnostics. For each element, the left bar–plot reports the residuals of the surface–strain channels,

$$r_i \;=\; \varepsilon_{s,i}^{\mathrm{pred}} \;-\; \varepsilon_{s,i}^{\mathrm{meas}},$$

with one bar per sensor in the order used by the input arrays (three channels per element: top and bottom at $\xi = 0.2$, top-only at $\xi = 0.8$). The predicted strain at station ξ_i (with local offsets y_i, z_i) is obtained from the reconstructed local DOFs $\mathbf{q}_{\mathrm{loc}}$ via

$$\varepsilon_{s,i}^{\mathrm{pred}} \;=\; \Big(\mathbf{B}_u(\xi_i) \;+\; z_i\, \mathbf{B}_w(\xi_i) \;+\; y_i\, \mathbf{B}_v(\xi_i) \Big)\, \mathbf{q}_{\mathrm{loc}}.$$

The right scatter–plots compare measured vs. predicted strains (one marker per sensor) and include the 1:1 reference line; points lying on the 1:1 indicate perfect agreement, whereas systematic offsets (parallel clouds) and slope deviations would reveal bias or scaling effects.

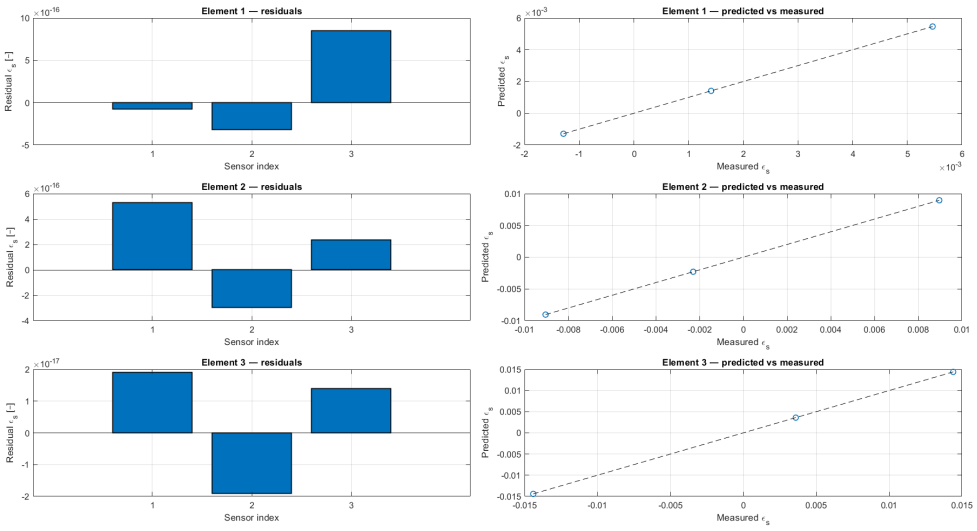

Figure 6.27: Case B (T-beam). Left: sensor residuals by element. Right: predicted vs measured ε_s with 1:1 guideline.

4) Discussion

- **Accuracy with reduced channels.** Despite the missing bottom reading at $\xi = 0.8$ on each element, the paired station at $\xi = 0.2$ plus a single top channel at $\xi = 0.8$ is sufficient to reproduce (u, w, ϕ_y) at essentially machine precision on the hinged T-beam.
- **Diagnostics.** The residual and 1:1 plots (Fig. 6.27) show negligible bias and dispersion, corroborating the metric-based assessment and confirming that the strain data are fully consistent with the reconstructed displacement field.
- **Implication.** Case B confirms that SSB-iFEM remains robust under mild accessibility constraints (paired+single-sided layout) also for the more articulated T-beam, anticipating the more restrictive layouts explored in Cases C–D.

6.4.3 Case C — SSB-iFEM: top sensors at $\xi = 0.2$, $\xi = 0.8$; bottom sensor at $\xi = 0.5$

1) Setup and instrumentation

The geometry, mesh, and boundary conditions are those of Section 6.4. Each element is instrumented with three surface–strain gauges along the mid-width

line ($y = 0$): *top* face at $\xi = 0.2$, *bottom* face at $\xi = 0.5$, and *top* face at $\xi = 0.8$ (i.e. $z = \{+h/2, -h/2, +h/2\}$ for all three elements).

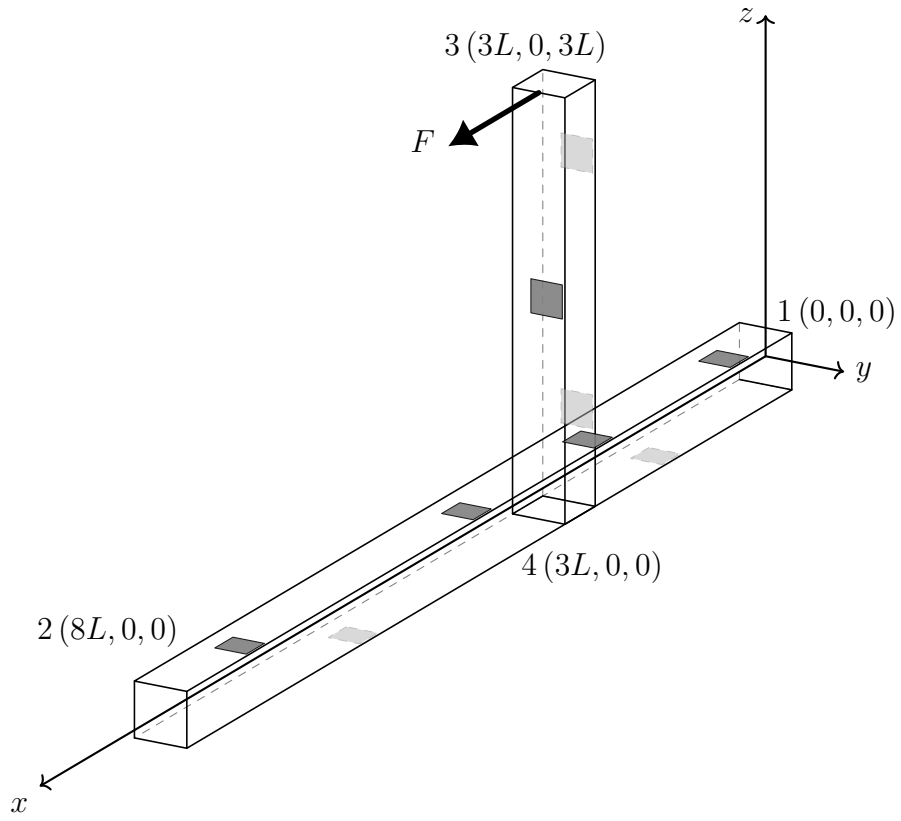

Figure 6.28: Case C (T-beam): sensor layout. Top sensors at $\xi = 0.2$ and $\xi = 0.8$; bottom sensor at $\xi = 0.5$ on each element. All sensors lie on the mid-width line ($y = 0$).

Measured channels. *SSB-iFEM input* consists of the surface axial strains ε_s at the sensor offsets. Table 6.39 lists the measured values (rounded) at the three stations of each element.

Table 6.39: Case C (T-beam) — Measured surface axial strains ε_s (dimensionless) at sensor stations for all three elements. Sensors lie on the mid-width line ($y = 0$) at $z = \pm h/2$ (top/bottom).

Element	ξ	Face	ε_s
1	0.2	top	0.0014
1	0.5	bottom	−0.0033
1	0.8	top	0.0055
2	0.2	top	−0.0090
2	0.5	bottom	0.0056
2	0.8	top	−0.0023
3	0.2	top	0.0144
3	0.5	bottom	−0.0090
3	0.8	top	0.0036

2) Reference (comparison target)

The reference nodal displacement vector $\mathbf{q}^{\text{ref}}$ is provided by the same forward FEM tool used in Cases A–B. The comparison is performed on the known in-plane DOFs at nodes 2–4:

$$(u_2, w_2, \phi_{y2}, u_3, w_3, \phi_{y3}, u_4, w_4, \phi_{y4}),$$

whose reference values are those already listed in Table 6.33.

3) Reconstruction results

Using the SSB inputs of Table 6.39, the inverse analysis matches the reference within numerical precision.

Table 6.40: Case C (T-beam) — Nodal quantities at free nodes (values). u, w in m; ϕ_y in rad.

Node	DOF	Unit	Reference	SSB
2	u	m	0.0000	0.0000
2	w	m	0.0000	0.0000
2	ϕ_y	rad	−2.7750e−1	−2.7750e−1
3	u	m	1.9352e1	1.9352e1
3	w	m	−4.5000	−4.5000
3	ϕ_y	rad	8.2500e−1	8.2500e−1
4	u	m	1.8750e−3	1.8750e−3
4	w	m	−4.5000	−4.5000
4	ϕ_y	rad	2.8500e−1	2.8500e−1

Relative error metrics. Global relative errors (excluding constrained DOFs) and per–element summaries are reported below. Here $\|\cdot\|_\infty$ is the max norm over the stacked vector of nodal DOFs, and $\|\cdot\|_2$ the Euclidean norm; we quote the ratio $\|\text{err}\|/\|\text{ref}\|$ as provided by the post-processor.

Table 6.41: Case C (T-beam) — Global relative error metrics (free nodes).

Metric	Value
$\|\text{err}\|_\infty/\|\text{ref}\|_\infty$	4.9570e−15
$\|\text{err}\|_2/\|\text{ref}\|_2$	6.8010e−15

Table 6.42: Case C (T-beam) — Per–element relative errors.

Element	$\|\text{err}\|_\infty/\|\text{ref}\|_\infty$	$\|\text{err}\|_2/\|\text{ref}\|_2$
1	2.1320e−14	2.1290e−14
2	2.1640e−14	2.1600e−14
3	4.9570e−15	6.7980e−15

The node-wise relative errors reported by the solver are effectively zero (printed as 0.000 %) for all DOFs at nodes 2–4.

Sensor diagnostics. For each element, the left bar–plot reports the residuals of the surface–strain channels,

$$r_i \;=\; \varepsilon_{s,i}^{\text{pred}} \;-\; \varepsilon_{s,i}^{\text{meas}},$$

with one bar per sensor in the order used by the input arrays (three channels per element, corresponding to the stations at $\xi = 0.2$, 0.5, and 0.8). The predicted strain at station ξ_i (with local offsets y_i, z_i) is obtained from the reconstructed local DOFs $\mathbf{q}_{\text{loc}}$ via

$$\varepsilon_{s,i}^{\text{pred}} \;=\; \Big(\mathbf{B}_u(\xi_i) \;+\; z_i\, \mathbf{B}_w(\xi_i) \;+\; y_i\, \mathbf{B}_v(\xi_i) \Big)\, \mathbf{q}_{\text{loc}}.$$

The right scatter–plots compare measured vs. predicted strains (one marker per sensor) and include the 1:1 reference line; points lying on the 1:1 indicate perfect agreement, whereas systematic offsets (parallel clouds) and slope deviations would reveal bias or scaling effects.

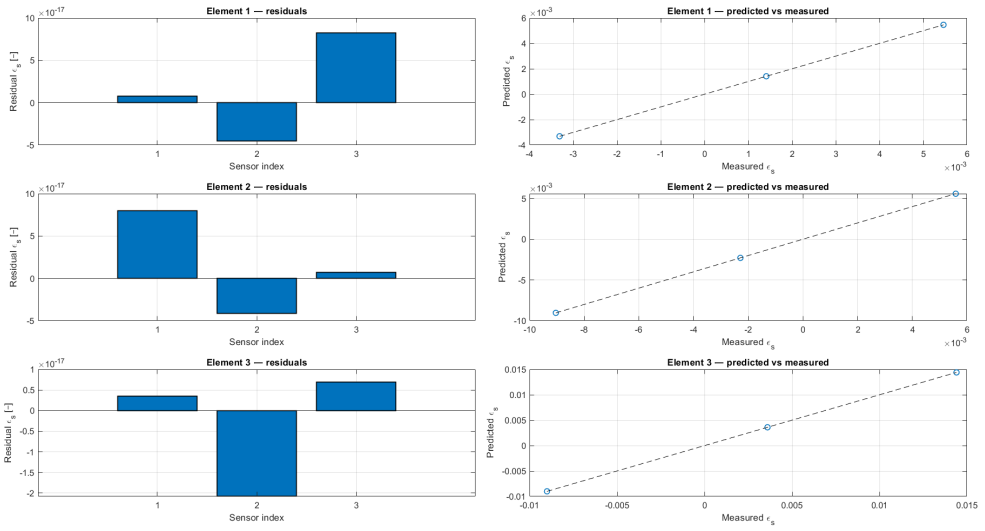

Figure 6.29: Case C (T-beam). Left: residuals per sensor (Elements 1–3 from top to bottom). Right: predicted vs. measured ε_s with 1:1 guideline.

4) Discussion

- **Accuracy with mixed sidedness.** A three-sensor layout per element (top–bottom–top at $\xi = 0.2$, 0.5, 0.8) still achieves agreement with the reference solution at essentially machine precision. The bottom station at $\xi = 0.5$ restores local pairing for bending about y, maintaining excellent observability of (u, w, ϕ_y) on the T-beam.

- **Practical note.** Even without full pairing at all stations, distributing the three sensors as in Case C provides a robust constraint set for SSB on this more articulated T-shaped structure.

6.4.4 Case D — SSB-iFEM: top-only sensors at $\xi = 0.2, 0.5, 0.8$

1) Setup and instrumentation

Geometry, mesh, kinematics, and boundary conditions are those of Section 6.4. Each element is instrumented with *three top-face* surface–strain sensors at parent abscissae $\xi = \{0.2, 0.5, 0.8\}$; all stations lie on the mid-width line ($y = 0$) and at $z = +h/2$ (top).

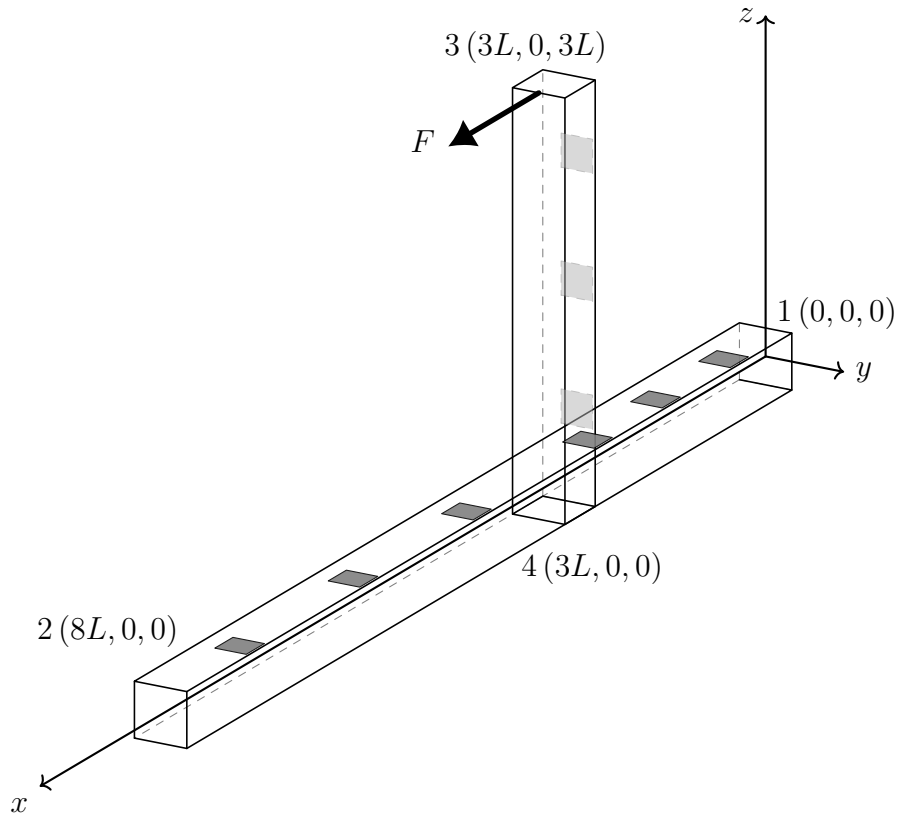

Figure 6.30: Case D (T-beam): sensor layout. Top-only sensors at $\xi = \{0.2, 0.5, 0.8\}$ on each element; all sensors on the mid-width line ($y = 0$).

Measured channels. The SSB-iFEM input consists of the surface axial strains ε_s at the sensor offsets (top face, $z = +h/2$). The measured values are:

Table 6.43: Case D (T-beam) — Measured surface axial strains ε_s (dimensionless) at the three top-face stations on each element.

Element	ξ	$\varepsilon_s(0.2)$	$\varepsilon_s(0.5)$	$\varepsilon_s(0.8)$
1		0.0014	0.0034	0.0055
2		−0.0090	−0.0057	−0.0023
3		0.0144	0.0090	0.0036

2) Reference (comparison target)

As in the previous cases, the forward FEM solver provides the *reference* nodal DOFs at the free nodes

$$(u_2, w_2, \phi_{y2}, u_3, w_3, \phi_{y3}, u_4, w_4, \phi_{y4}),$$

which are the same reference values reported in Table 6.33. Only the SSB-iFEM reconstruction is considered here, since the classical iFEM formulation would require paired top/bottom measurements to build curvature channels.

3) Reconstruction results

With top-only instrumentation ($y_i = 0$ and $z_i = +h/2$ at all stations), the SSB system lacks the paired top/bottom information needed to disentangle mid-line strain ε from bending curvature κ_{zz}. Consequently, the inverse fit becomes ill-conditioned and the reconstructed nodal quantities deviate markedly from the reference solution.

Nodal values and relative errors. Table 6.44 reports SSB vs. reference at free nodes, together with the relative error (in %).

Table 6.44: Case D (T-beam) — Nodal quantities at free nodes (values and relative errors). u, w in m; ϕ_y in rad.

Node	DOF	Unit	SSB	Reference	Rel. err [%]
2	u	m	0.0000	0.0000	0.0000
2	w	m	0.0000	0.0000	0.0000
2	ϕ_y	rad	2.6920e−1	−2.7750e−1	197.0160
3	u	m	3.2490	1.9350e1	83.2130
3	w	m	−4.4920	−4.5000	0.1840
3	ϕ_y	rad	2.6170e−1	8.2500e−1	68.2770
4	u	m	5.4860e−1	1.8750e−3	29 158.3330
4	w	m	−4.5000	−4.5000	0.0000
4	ϕ_y	rad	−2.6170e−1	2.8500e−1	191.8310

Aggregate relative metrics. Global relative errors (excluding constrained DOFs) and per–element figures are summarised in Table 6.45. Here $\| \cdot \|_\infty$ is the infinity norm (max absolute component) and $\| \cdot \|_2$ is the Euclidean norm.

Table 6.45: Case D (T-beam) — Relative errors w.r.t. the reference solution.

Quantity	$\|\text{err}\|_\infty / \|\text{ref}\|_\infty$	$\|\text{err}\|_2 / \|\text{ref}\|_2$
Whole structure	8.3210	7.9200
Element 1	1.2150	2.1000
Element 2	1.2150	2.0960
Element 3	8.3210	7.9120

4) Discussion

- **Observability shortfall.** With top-only sensors ($z = +h/2$ at all stations), the SSB prediction operator cannot separate the mid-line strain ε from the curvature κ_{zz}; the problem is effectively under–determined and ill-conditioned.
- **Impact on accuracy.** The loss of pairing drives very large biases at the free nodes (Table 6.44) and large global relative errors (Table 6.45), in stark contrast with the machine-precision reconstructions of Cases A–C.

- **Design implication.** For Euler–Bernoulli beams such as the present T-configuration, at least one paired top/bottom station per element (or equivalent multi-face information) is necessary to achieve accurate reconstructions of (u, w, ϕ_y); purely single-sided layouts should be avoided unless supplemented by additional information or regularisation.

6.4.5 Case E — T-beam, simply supported; uniform distributed load on the vertical leg; SSB-iFEM with one inverse element on the vertical

1) Setup and instrumentation

The structure is a T-shaped Euler–Bernoulli beam with *pinned–pinned* global boundary conditions at the two extremities of the horizontal member. A *uniform distributed load* of intensity $q = -5\times10^{-4}$ acts along the *local* x of the vertical leg (parallel to the global x). The forward (direct) FEM mesh splits the vertical branch into four equal segments to improve accuracy of internal fields; the inverse SSB-iFEM model uses *one* inverse element on the vertical branch in this case (the horizontal branches are modeled consistently with the L-beam convention of Chapter 5).

Instrumentation follows the "Case B" philosophy (paired at the first station, single-sided at the second): for each element, gauges are placed at parent abscissae $\xi = \{0.2, 0.8\}$ on the mid-width line ($y = 0$), with a *paired* top/bottom installation at $\xi = 0.2$ ($z = \pm h/2$) and a *top-only* gauge at $\xi = 0.8$ ($z = +h/2$).

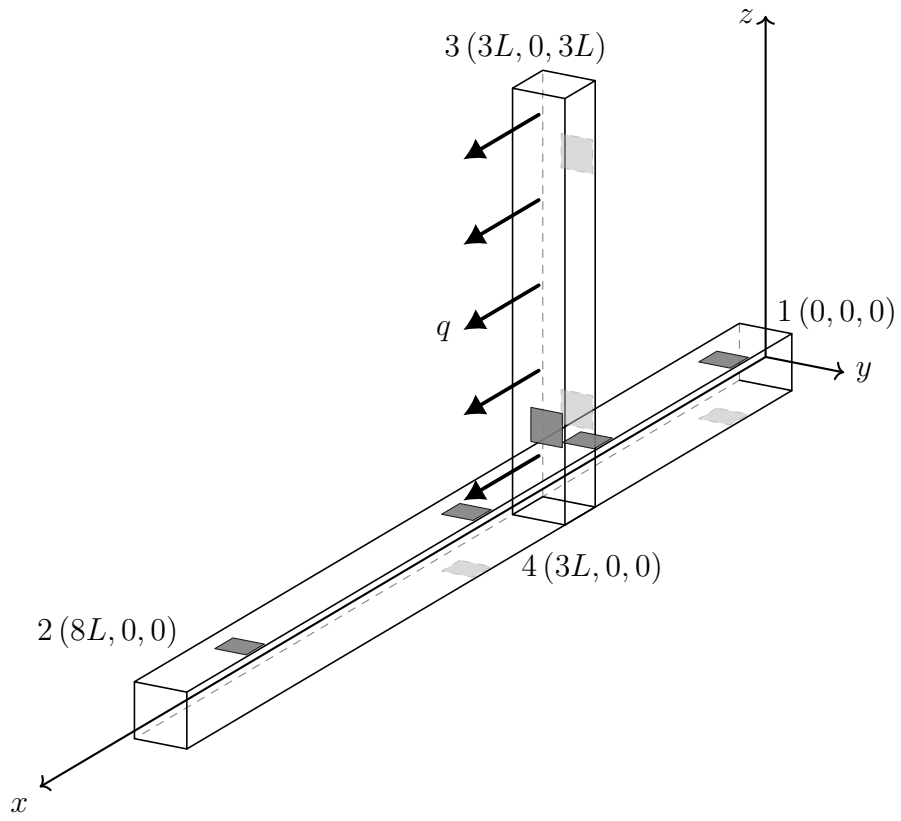

Figure 6.31: Case E (T-beam): geometry, supports (pinned ends on the horizontal member), vertical leg with uniform distributed load $q = -5{\times}10^{-4}$ along local x, and SSB sensor layout (paired top/bottom at $\xi = 0.2$; top-only at $\xi = 0.8$; all gauges at $y = 0$).

Measured channels (SSB input). Surface axial strains ε_s at the available offsets are reported below for each element and station (top/bottom refer to $z = \pm h/2$; all gauges at $y = 0$):

Table 6.46: Case E — Measured surface strains ε_s (dimensionless) by element and station.

Element	Station	$\varepsilon_s^{\text{top}}$ ($\xi = 0.2$)	$\varepsilon_s^{\text{bot}}$ ($\xi = 0.2$)	$\varepsilon_s^{\text{top}}$ ($\xi = 0.8$)
1		0.1106	−0.0919	0.4144
2		−0.6806	0.6694	−0.1744
3		0.8634	−0.8634	0.0534

2) Reference

The independent forward FEM solver (provided by the advisor) supplies the global nodal displacement vector used as reference solution. For the in-plane DOFs at nodes 1–4 (ordered as $(u_1, w_1, \phi_{y1};\ u_2, w_2, \phi_{y2};\ u_3, w_3, \phi_{y3};\ u_4, w_4, \phi_{y4})$) we obtain

$$\mathbf{q}^{\mathrm{ref}} = \begin{bmatrix} 0.0000 & 0.0000 & 6.1875 \\ 0.0000 & 0.0000 & -20.8125 \\ 1.2490\mathrm{e}3 & -3.3750\mathrm{e}2 & 4.8375\mathrm{e}1 \\ 2.8125\mathrm{e}{-1} & -3.3750\mathrm{e}2 & 2.1375\mathrm{e}1 \end{bmatrix}^{\top},$$

which are the reference values also reported in Table 6.48 for direct comparison against the reconstruction.

3) Reconstruction results

Global relative metrics (excluding constrained DOFs) and per–element figures are:

Table 6.47: Case E — Relative errors w.r.t. the reference solution (global and per element).

Scope	$\|\mathrm{err}\|_\infty/\|\mathrm{ref}\|_\infty$	$\|\mathrm{err}\|_2/\|\mathrm{ref}\|_2$
Whole structure	6.0800e−3	5.6870e−3
Element 1	1.7700e−13	1.7680e−13
Element 2	1.7700e−13	1.7640e−13
Element 3	6.0800e−3	5.6870e−3

Nodal comparisons (values and relative errors in %):

Table 6.48: Case E — Nodal quantities at all nodes (values and relative errors). u, w in m; ϕ_y in rad.

Node	DOF	Unit	SSB		Reference		Rel. err [%]
1	u	m	0.0000		0.0000		0.0000
1	w	m	0.0000		0.0000		0.0000
1	ϕ_y	rad	6.1880		6.1880		0.0000
2	u	m	0.0000		0.0000		0.0000
2	w	m	0.0000		0.0000		0.0000
2	ϕ_y	rad	−2.0810	e1	−2.0810	e1	0.0000
3	u	m	1.2570	e3	1.2490	e3	0.6080
3	w	m	−3.3750	e2	−3.3750	e2	0.0000
3	ϕ_y	rad	4.8880	e1	4.8380	e1	1.0470
4	u	m	2.8130	e−1	2.8130	e−1	0.0000
4	w	m	−3.3750	e2	−3.3750	e2	0.0000
4	ϕ_y	rad	2.1380	e1	2.1380	e1	0.0000

Sensor diagnostics. For each element, the left bar–plot shows the residuals $r_i = \varepsilon_{s,i}^{\text{pred}} - \varepsilon_{s,i}^{\text{meas}}$ (one bar per sensor, in input order), with predicted strains evaluated as

$$\varepsilon_{s,i}^{\text{pred}} = \Big(\mathbf{B}_u(\xi_i) + z_i\,\mathbf{B}_w(\xi_i) + y_i\,\mathbf{B}_v(\xi_i)\Big)\,\mathbf{q}_{\text{loc}}.$$

The right scatter–plot compares measured vs. predicted strains (one marker per sensor) with a 1:1 guideline; alignment with the 1:1 indicates unbiased fit.

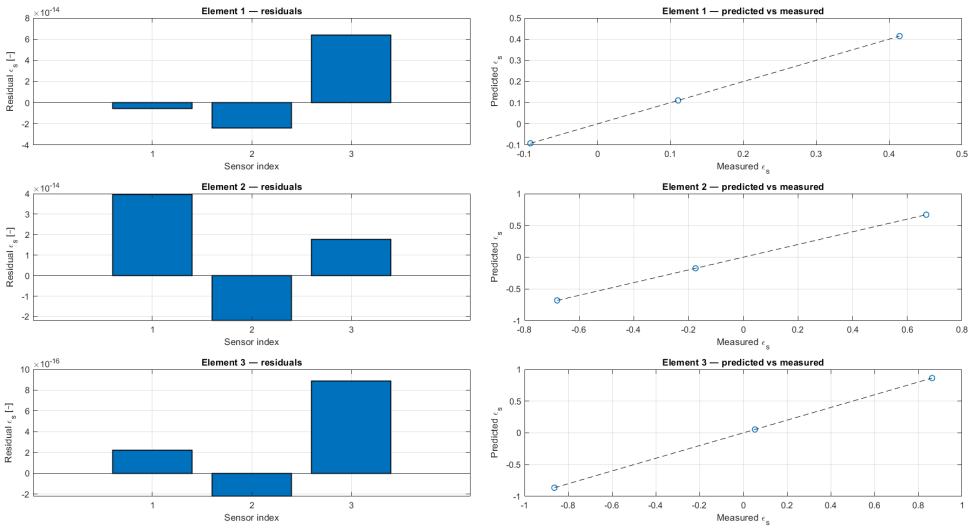

Figure 6.32: Case E (T-beam). Left: sensor residuals by element. Right: predicted vs measured ε_s with 1:1 guideline.

4) Discussion

- **Accuracy and localization.** Element-wise metrics (Table 6.47) are at round-off for the horizontal branches (Elements 1–2) and around 0.6% on the vertical member (Element 3), consistent with the single inverse element used on the vertical leg under distributed loading.

- **Nodal picture.** The largest deviations concentrate at node 3 (Table 6.48), mainly on u and ϕ_y; transverse displacement w is recovered accurately at all nodes.

- **Nodal picture.** The largest deviations concentrate at node 3 (Table 6.48), mainly on u and ϕ_y; transverse displacement w is recovered accurately at all nodes. Evaluating the single-element inverse solution at the mid-height section of the vertical leg (corresponding to node 5 in Case F) yields a relative error of about 2.0% on u, with w and ϕ_y remaining essentially exact, and will be used below as a reference for the two-element discretization.

6.4.6 Case F — T-beam, simply supported; uniform distributed load on the vertical leg; SSB-iFEM with two inverse elements on the vertical

1) Setup and instrumentation

Same structure, supports, and loading as Case E (pinned–pinned T-beam; uniform $q = -5{\times}10^{-4}$ along the vertical leg's local x). The *forward* mesh again splits the vertical leg into four equal segments. The *inverse* SSB model now uses *two* elements on the vertical branch (equal size), to increase localization of the reconstructed fields.

Instrumentation is unchanged: per element, gauges at $\xi = \{0.2, 0.8\}$ with *paired* top/bottom at $\xi = 0.2$ and *top-only* at $\xi = 0.8$; all gauges on the mid-width line ($y = 0$).

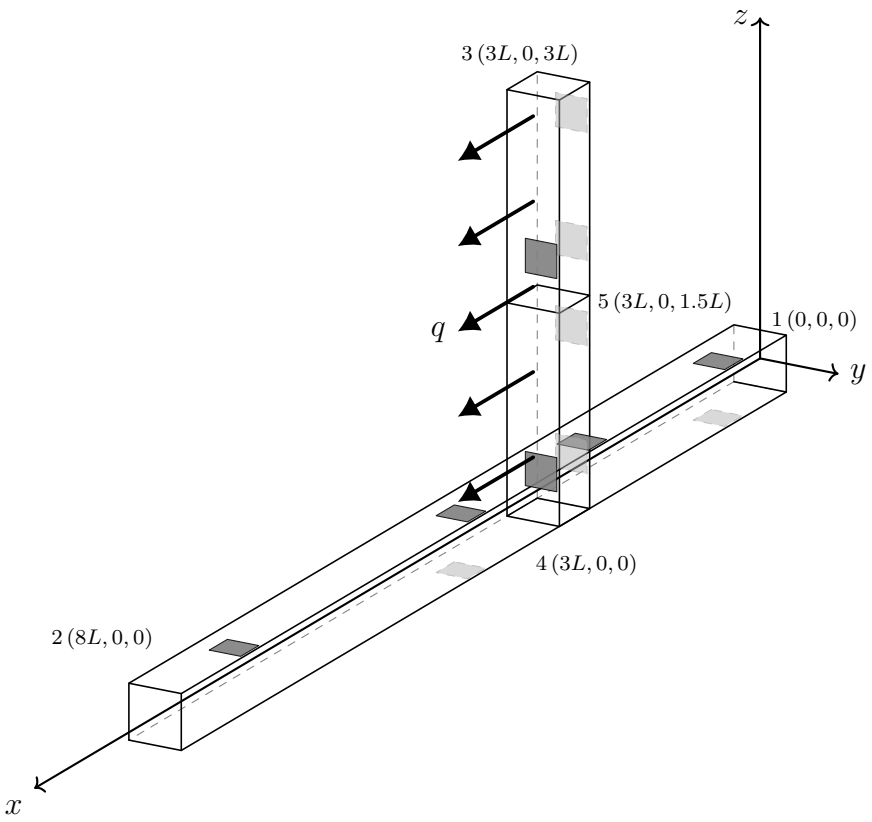

Figure 6.33: Case F (T-beam): geometry, supports, vertical leg with uniform load, and SSB sensor layout (paired at $\xi = 0.2$, top-only at $\xi = 0.8$; $y = 0$). The inverse model employs *two* elements on the vertical leg.

Measured channels (SSB input). Measured ε_s per element and station:

Table 6.49: Case F — Measured surface strains ε_s (dimensionless) by element and station.

Element	Station	$\varepsilon_s^{\text{top}}$ ($\xi = 0.2$)	$\varepsilon_s^{\text{bot}}$ ($\xi = 0.2$)	$\varepsilon_s^{\text{top}}$ ($\xi = 0.8$)
1		0.1106	−0.0919	0.4144
2		−0.6806	0.6694	−0.1744
3		1.0997	−1.0997	0.4922
4		0.2222	−0.2222	0.0197

2) Reference

The independent forward FEM solver (provided by the advisor) supplies the global nodal displacement vector used as reference solution. For the in-plane DOFs at nodes 1–5 (ordered as $(u_1, w_1, \phi_{y1};\ u_2, w_2, \phi_{y2};\ u_3, w_3, \phi_{y3};\ u_4, w_4, \phi_{y4};\ u_5, w_5, \phi_{y5})$ we obtain

$$\mathbf{q}^{\text{ref}} = \begin{bmatrix} 0.0000 & 0.0000 & 6.1875 \\ 0.0000 & 0.0000 & -20.8125 \\ 1.2490\text{e}3 & -3.3750\text{e}2 & 4.8375\text{e}1 \\ 2.8125\text{e}{-1} & -3.3750\text{e}2 & 2.1375\text{e}1 \\ 5.3606\text{e}2 & -3.3750\text{e}2 & 4.5000\text{e}1 \end{bmatrix}^{\top},$$

which are the reference values also reported in Table 6.51 for direct comparison against the reconstruction.

3) Reconstruction results

Relative errors (global and per element):

Table 6.50: Case F — Relative errors w.r.t. the reference solution (global and per element).

Scope	$\|\text{err}\|_\infty / \|\text{ref}\|_\infty$	$\|\text{err}\|_2 / \|\text{ref}\|_2$
Whole structure	6.0800e−3	5.2980e−3
Element 1	8.0830e−13	8.0730e−13
Element 2	8.0830e−13	8.0560e−13
Element 3	3.5410e−3	2.6620e−3
Element 4	6.0800e−3	5.4420e−3

Nodal values and relative errors (%):

Table 6.51: Case F — Nodal quantities at all nodes (values and relative errors). u, w in m; ϕ_y in rad.

Node	DOF	Unit	SSB		Reference		Rel. err [%]
1	u	m	0.0000		0.0000		0.0000
1	w	m	0.0000		0.0000		0.0000
1	ϕ_y	rad	6.1880		6.1880		0.0000
2	u	m	0.0000		0.0000		0.0000
2	w	m	0.0000		0.0000		0.0000
2	ϕ_y	rad	−2.0810	e1	−2.0810	e1	0.0000
3	u	m	1.2570	e3	1.2490	e3	0.6080
3	w	m	−3.3750	e2	−3.3750	e2	0.0000
3	ϕ_y	rad	4.8880	e1	4.8380	e1	1.0470
4	u	m	2.8130	e−1	2.8130	e−1	0.0000
4	w	m	−3.3750	e2	−3.3750	e2	0.0000
4	ϕ_y	rad	2.1380	e1	2.1380	e1	0.0000
5	u	m	5.3800	e2	5.3610	e2	0.3540
5	w	m	−3.3750	e2	−3.3750	e2	0.0000
5	ϕ_y	rad	4.5250	e1	4.5000	e1	0.5620

Sensor diagnostics. Residual and 1:1 plots are constructed as in Case E:

$$r_i = \varepsilon_{s,i}^{\text{pred}} - \varepsilon_{s,i}^{\text{meas}}, \qquad \varepsilon_{s,i}^{\text{pred}} = \Big(\mathbf{B}_u(\xi_i) + z_i\,\mathbf{B}_w(\xi_i) + y_i\,\mathbf{B}_v(\xi_i)\Big)\,\mathbf{q}_{\text{loc}}.$$

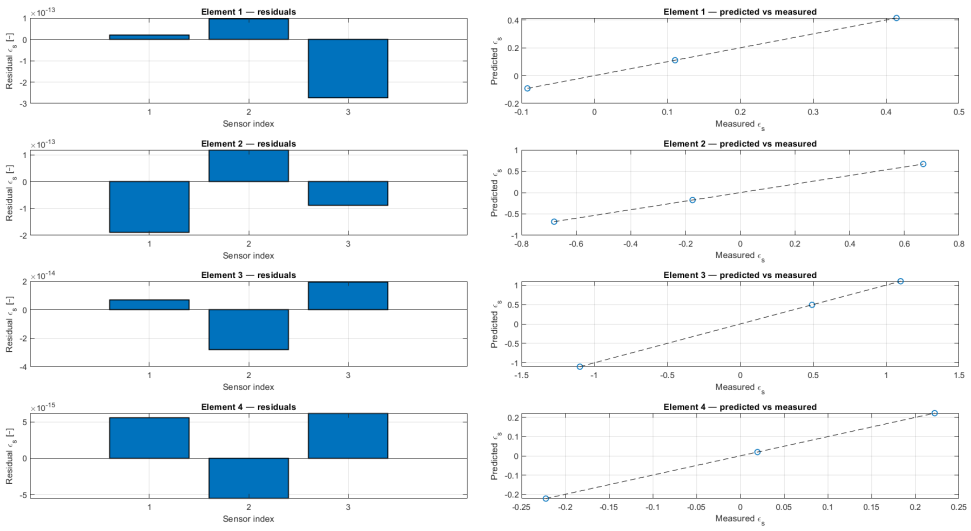

Figure 6.34: Case F (T-beam). Left: sensor residuals by element. Right: predicted vs measured ε_s with 1:1 guideline.

4) Discussion

- **Effect of vertical discretization in the inverse model.** Using two inverse elements on the vertical leg reduces the element-wise relative errors there (Table 6.50, Elements 3–4) compared to aggregating the vertical branch into a single inverse element (Case E).

- **Nodal trends.** The largest discrepancies remain localized at inner vertical nodes (3 and 5), predominantly on the axial DOF u and the rotation ϕ_y, while w is consistently accurate.

- **Mid-height section comparison with Case E.** Although the reconstruction at node 3 is practically unchanged between Cases E and F, sampling the *single-element* inverse solution of Case E at the mid-height section of the vertical leg (same physical location as node 5 in Case F) shows a larger axial error there: the relative error on u is about 2.0%, with w and ϕ_y remaining essentially exact (0.0% and $\approx 0.56\%$, respectively). In the present two-element inverse model, the corresponding errors at node 5 are $\approx 0.35\%$ in u, 0.0% in w, and $\approx 0.56\%$ in ϕ_y. This indicates that refining the inverse discretization of the vertical leg mainly improves the internal distribution of axial displacement, even if the reconstruction at the upper node 3 is nearly unaffected.

Chapter 7

Conclusions

This thesis has investigated the application of the Single-Sensor-Based inverse Finite Element Method (SSB-iFEM) to Euler–Bernoulli beam elements, with the objective of reconstructing the displacement field from a reduced number of strain sensors. Building on recent SSB formulations for plates and shells, a new least-squares functional has been derived for one-dimensional beam models and implemented in MATLAB, and its performance has been assessed on both simple and complex beam configurations.

The work started from the classical Euler–Bernoulli iFEM formulation, in which axial strain and bending curvatures are reconstructed from mid-line quantities and typically require paired measurements on opposite faces. A general sensor-based SSB-iFEM formulation was then developed by expressing each surface strain measurement as a linear combination of axial strain and bending curvatures, evaluated at the actual sensor coordinates within the cross-section. In this framework, each sensor is treated as an independent observation associated with its own spatial position, and the functional element is written as a weighted least-squares sum of all sensor residuals. The resulting element matrices preserve the symmetry and positive semi-definiteness of the classical iFEM operators and are assembled into a global system that is formally identical in structure to the standard inverse finite element equations.

The first verification step focused on single-element, straight-beam scenarios with analytically prescribed displacement fields. These tests were designed to check the consistency of the theoretical operators, the MATLAB implementation, and the handling of local-to-global frames and boundary conditions. When full, paired instrumentation on all faces was used, the SSB-iFEM reconstruction matched the classical Euler–Bernoulli iFEM at machine precision, confirming the theoretical equivalence of the two formulations when they are supplied with equivalent information. Under reduced and

unpaired layouts on the mid-width line, the SSB-iFEM still reproduced the observable displacement components with negligible error, while the lateral displacement remained unobserved due to the lack of sensitivity to curvature about the corresponding axis. These simple scenarios highlighted the close relationship between sensor layout, curvature observability, and the accuracy of the reconstructed displacement field.

The second part of the work extended the verification campaign to more complex beam-like structures: a cantilever L-beam, a cantilever Z-beam, and a hinged T-beam with a branching joint. For each configuration, a systematic set of sensor layouts was studied, including: (i) full paired instrumentation on top and bottom faces (baseline comparison between SSB and classical iFEM); (ii) a reduced layout with one paired station and one single-sided sensor per element; (iii) three unpaired sensors distributed along the cross-section; and (iv) a highly constrained top-only layout. Reference solutions and synthetic strain measurements were generated using an independent forward FEM tool, ensuring that the inverse solution was tested against an external dataset.

The numerical results on these complex structures support several key conclusions. First, in all baseline cases with paired sensors on opposite faces, the SSB-iFEM reproduced the reference displacement fields with accuracy comparable to the classical iFEM. This confirms that the SSB formulation does not introduce any loss of information when classical curvature channels are effectively available, and that it can be used as a drop-in alternative to the conventional beam iFEM under ideal instrumentation conditions. Second, reduced layouts combining one paired station with an additional single-sided sensor proved sufficient to retain full-field accuracy on all the considered configurations, at least for the loading conditions examined. In these cases, the SSB solution matched the reference displacements with very small global relative errors, demonstrating that the method can tolerate moderate accessibility constraints without compromising reconstruction quality.

Third, the study of highly asymmetric and top-only layouts provided insight into the limitations of the approach. For asymmetric configurations with sensors on different faces, the SSB-iFEM still achieved accurate reconstruction of the targeted displacement components, provided that at least one sensor was available on each of the two opposite faces involved in the curvature of interest. In contrast, when all sensors were placed on the same face, the inverse system became ill-conditioned: the mid-line strain and bending curvature contributions could no longer be disentangled, and the reconstructed axial degrees of freedom and rotations exhibited large relative errors, even though vertical deflections remained reasonably accurate. These results emphasise that, while SSB-iFEM relaxes the strict requirement of fully paired layouts, some degree of through-thickness information is still necessary to en-

sure a well-conditioned problem, especially in multi-element assemblies with corners and branching joints.

Finally, the T-beam test with distributed loading on the vertical web highlighted the impact of the inverse-model discretisation on reconstruction accuracy. When the vertical leg of the T-beam was represented by a single inverse element, the global errors remained moderate but local discrepancies on that element were noticeable. Subdividing the same segment into two inverse elements, while keeping the same sensor layout, led to a reduction of element-wise errors on the vertical branch and improved agreement with the reference solution. This confirms that, as in classical FEM, an adequate inverse discretisation is important to capture local variations of the deformation field, particularly in regions where the forward model employs a finer mesh or where significant gradients are expected.

From an application standpoint, the results obtained in this thesis support the use of SSB-iFEM as a practical and efficient tool for shape sensing of beam-like structures in structural health monitoring and real-time displacement reconstruction. The formulation naturally accommodates arbitrary cross-sections and sensor coordinates, and its ability to operate with reduced and partially unpaired sensor layouts is especially attractive in aerospace applications, where access to structural surfaces is often limited and the installation of large sensor networks is impractical. Within the tested conditions, the method has shown robustness to moderate sensor reduction and to geometric complexity, while preserving the main advantages of iFEM, namely independence from the applied loads and boundary conditions and compatibility with standard finite element workflows.

Future work. Several directions emerge for future developments. A natural continuation of this research is the experimental validation of the proposed SSB-iFEM formulation on beam specimens instrumented with strain gauges or fibre Bragg gratings, in order to assess its performance under measurement noise, modelling uncertainties, and realistic loading conditions. Another important extension concerns the integration of sensor-noise models and regularisation strategies into the least-squares functional, to improve robustness in the presence of sparse or noisy data. The optimisation of sensor placement—for instance through sensitivity analysis or optimisation algorithms—would further enhance the efficiency of the method and help define guidelines for practical instrumentation of real structures. In addition, the present work has been limited to planar Euler–Bernoulli beam configurations, where each structural member lies in a single plane and bending predominantly occurs about one axis. A natural extension is the generalisation of the SSB-iFEM framework to fully three-dimensional beam and frame

geometries, in which the beam centreline follows an arbitrary space curve and bending in two orthogonal planes is coupled with torsion, thus enabling truly three-dimensional shape sensing of complex aerospace assemblies.

On the modelling side, the SSB concept could be extended to more advanced beam theories, such as Timoshenko beams, and to combined beam/shell inverse models for more realistic aeronautical structures. Moreover, coupling SSB-iFEM-based shape sensing with damage-detection or load-identification procedures would further strengthen its role within structural health monitoring systems.

Acknowledgments

First and foremost, I would like to express my sincere gratitude to my supervisor, Prof. Marco Gherlone, for making this project possible, and for the patience, availability, and time he dedicated to me. Working on this thesis has been extremely stimulating, and I am truly grateful for the way in which we have worked together throughout this journey.

I am deeply grateful to my parents, Gian Franco and Chiara, who have always supported me throughout my studies, no matter what. Their constant presence, encouragement, and understanding have been essential, and this achievement would not have been possible without them.

I would also like to thank my sisters, Giada and Ilaria. Having gone through their own, very different university paths, they have been able to help me, offer me new perspectives, and challenge me through our many conversations. Their example and support have been a precious reference point along the way.

My heartfelt thanks go to all my friends, who are far too many to list individually. They are the ones who have helped me and continuously supported me, especially in the darkest and most difficult moments of this journey. Their presence, closeness, and willingness to stand by me have meant more than I can say. With them I have shared some of the best and the worst moments, and through these experiences I have also learned a lot about who I am.

Finally, my deepest gratitude goes to my girlfriend, Judith. This thesis would not have been possible without her. She has believed in me far more than I was able to believe in myself, encouraging me, comforting me, and always staying close despite the challenges of distance and all the sacrifices it required. Her support has been a fundamental source of strength and motivation.

References

[1] V. Biscotti, M. Esposito, and M. Gherlone, "A new single sensor based ifem formulation for shape-sensing of thin-walled structures instrumented with single-sided sensor configurations: formulation, numerical assessment, and experimental validation," *Mechanical Systems and Signal Processing*, vol. 232, p. 112700, 2025.

[2] A. Tessler and J. L. Spangler, "A least-squares variational method for full-field reconstruction of elastic deformations in shear-deformable plates and shells," *Computers & Structures*, vol. 87, no. 9–10, pp. 582–601, 2009.

[3] M. Gherlone, P. Cerracchio, M. Mattone, M. Di Sciuva, and A. Tessler, "Shape sensing of plate and shell structures by the inverse finite element method: numerical and experimental studies," *International Journal of Solids and Structures*, vol. 132-133, pp. 174–187, 2018.

[4] M. Gherlone, P. Cerracchio, A. Tessler, M. Mattone, and M. Di Sciuva, "Beam and frame shape sensing by inverse finite element method: numerical and experimental validation," *Smart Materials and Structures*, vol. 28, no. 9, p. 095021, 2019.

[5] M. Gherlone, A. Tessler, M. Di Sciuva, G. Giunta, and P. Paolino, "Beam shape sensing using inverse finite element method: theory and experimental validation," *Smart Materials and Structures*, vol. 21, no. 6, p. 065004, 2012.

[6] M. Gherlone *et al.*, "Inverse finite element method for euler–bernoulli beam structures: formulation and validation," in *Proceedings of the Society for Experimental Mechanics (SEM) Conference*, 2019. IMAC-XXXVII, Orlando, FL.

[7] P. Savino, M. Gherlone, and F. Tondolo, "Shape sensing with inverse finite element method for slender structures," *Structural Engineering and Mechanics*, vol. 72, no. 2, pp. 217–227, 2019.

[8] M. Gherlone, P. Cerracchio, M. Mattone, M. Di Sciuva, and A. Tessler, "Shape sensing of 3d frame structures using an inverse finite element method," *International Journal of Solids and Structures*, vol. 49, no. 22, pp. 3100–3112, 2012.

[9] M. Gherlone, P. Cerracchio, and M. Mattone, "Shape sensing methods: review and experimental comparison on a wing-shaped plate," *Progress in Aerospace Sciences*, vol. 99, pp. 14–26, 2018.

[10] P. Cerracchio, M. Gherlone, M. Di Sciuva, and A. Tessler, "A novel approach for displacement and stress monitoring of sandwich structures based on the inverse finite element method," *Composite Structures*, vol. 127, pp. 69–76, 2015.

[11] A. Kefal, A. Tessler, and E. Oterkus, "An enhanced inverse finite element method for displacement and stress monitoring of multilayered composite and sandwich structures," *Composite Structures*, vol. 179, pp. 514–540, 2017.

[12] A. Kefal, E. Oterkus, A. Tessler, and J. L. Spangler, "A quadrilateral inverse-shell element with drilling degrees of freedom for shape sensing and structural health monitoring," *Engineering Science and Technology, an International Journal*, vol. 19, no. 3, pp. 1299–1313, 2016.

[13] A. Kefal and M. Yildiz, "Modeling of sensor placement strategy for shape sensing and structural health monitoring of a wing-shaped sandwich panel using inverse finite element method," *Sensors*, vol. 17, no. 12, p. 2775, 2017.

[14] M. Esposito and M. Gherlone, "Composite wing box deformed-shape reconstruction based on measured strains: optimization and comparison of existing approaches," *Aerospace Science and Technology*, vol. 99, p. 105758, 2020.

[15] R. Roy, A. Tessler, C. Surace, and M. Gherlone, "Efficient shape sensing of plate structures using the inverse finite element method aided by strain pre-extrapolation," *Thin-Walled Structures*, vol. 180, p. 109798, 2022.

[16] A. Kefal, I. E. Tabrizi, M. Yildiz, and A. Tessler, "A smoothed ifem approach for efficient shape-sensing applications: numerical and experimental validation on composite structures," *Mechanical Systems and Signal Processing*, vol. 152, p. 107486, 2021.

[17] C. R. Farrar and K. Worden, "An introduction to structural health monitoring," *Philosophical Transactions of the Royal Society A: Mathematical, Physical and Engineering Sciences*, vol. 365, no. 1851, pp. 303–315, 2007.

[18] W. L. Ko, W. L. Richards, and V. T. Fleischer, "Applications of ko displacement theory to the deformed shape predictions of the doubly-tapered ikhana wing," Tech. Rep. NASA/TP-2009-214652, NASA Dryden Flight Research Center, 2009.

[19] O. C. Zienkiewicz and R. L. Taylor, *The Finite Element Method: Volume 1, The Basis*. Butterworth–Heinemann, 5 ed., 2000.

[20] S. P. Timoshenko and J. N. Goodier, *Theory of Elasticity*. McGraw–Hill, 3 ed., 1970.